UNIVERSIDADE FEDERAL DO RIO GRANDE DO SUL
INSTITUTO DE FÍSICA
PROGRAMA DE PÓS GRADUAÇÃO EM FÍSICA

Gabriel Lauffer Ramos

Asteroseismology of pulsating low-mass white dwarf stars

Ou

Astrossismologia de estrelas anãs brancas pulsantes de baixa massa

Porto Alegre, Brasil

February, 2024

Gabriel Lauffer Ramos

Astrossismologia de estrelas anãs brancas pulsantes de baixa massa

Thesis submitted to *Programa de Pós-Graduação em Física at Universidade Federal do Rio Grande do Sul* as a partial requirement for the degree of Doctor of Sciences

Supervisor: Alejandra D. Romero

Porto Alegre, Brasil

February, 2024

CIP - Catalogação na Publicação

Ramos, Gabriel Lauffer
Astrossismologia de estrelas anãs brancas pulsantes de baixa massa / Gabriel Lauffer Ramos. -- 2024.
124 f.
Orientadora: Alejandra Daniela Romero.

Tese (Doutorado) -- Universidade Federal do Rio Grande do Sul, Instituto de Física, Programa de Pós-Graduação em Física, Porto Alegre, BR-RS, 2024.

1. Astrossismologia. 2. Anã Branca. 3. Sistemas Binários. I. Romero, Alejandra Daniela, orient. II. Título.

Elaborada pelo Sistema de Geração Automática de Ficha Catalográfica da UFRGS com os dados fornecidos pelo(a) autor(a).

Gabriel Lauffer Ramos

Astrossismologia de estrelas anãs brancas pulsantes de baixa massa

Thesis submitted to *Programa de Pós-Graduação em Física at Universidade Federal do Rio Grande do Sul* as a partial requirement for the degree of Doctor of Sciences

Trabalho aprovado. Porto Alegre, Brasil, *5* de *fevereiro* de *2024*:

Prof^a. Dr^a. Alejandra D. Romero
Orientadora

Prof^a. Dr^a. Agnes Kim
Convidado 1

Prof. Dr. Francis Timmes
Convidado 2

Prof^a. Dr^a. Marina Trevisan
Convidado 3

Prof. Dr. José Eduardo da Siveira Costa
Convidado 4

Porto Alegre, Brasil
February, 2024

To my wife, Chaiana.

Acknowledgements

The message in this section will be written in English and Portuguese in order to reach everyone who deserves a proper thank you.

English

To pursue the academic path is an old dream. I decided that I would pursue this path around the age of 17 when I realized that basic research and a constant learning environment were what made me happy and what I wanted for my future. This decision was encouraged by the environment I was in: a technical school that incentives research, good physics and chemistry teachers, a great example of a scientist in the family, and being raised by parents who always believed in my potential and who never spared efforts to ensure that I could dedicate myself to my life choices. To my technical school teachers, my godfather Jackson (*in memoriam*), my parents, Eliane, and Sandro, my brother Guilherme, my uncle Émerson, and my grandparents, Rudy and Carmelita, my thanks

As an undergraduate, the first opportunity to work in research was given to me by Dr. Matheus J. Lazo, and even though I didn't follow his line of research, he has always been a point of support in the main doubts about physics and continues to be a reference in theoretical knowledge on the most diverse topics to this day. Later, in the United States, Dr. Shashi Kanbur introduced me to the fantastic world of variable stars and gave me opportunities for research and collaboration beyond my expectations. Shashi is a great example of a mentor, as he always sought opportunities for his students and always demonstrated a passion for basic research. At the end of my graduation, upon returning to Brazil, Dr. Fabricio Ferrari accepted me as his student, even though variable stars were not his research topic, his knowledge of digital signal processing was fundamental in polishing my work and guaranteeing my position as a student in the UFRGS master's program. To the professors mentioned here and to the others who participated in my education, as well as to my undergraduate colleagues, especially Vinicius Becker, my thanks.

During my postgraduate studies, I entered the master's degree under the supervision of Dr. Alejandra Romero and co-supervised by Dr. Kepler de Souza Oliveira Filho. Its understanding of the Universe, knowledge of various topics, and dedication to ensuring access to information for students provided by Kepler are invaluable and fundamental to ensuring quality in research. During my doctorate, I had the opportunity to work in other countries, experiences that were fundamental in ensuring knowledge and collaborations that impacted this work. Such opportunities would not have been obtained without all of Alejandra's efforts to help, guide, and encourage me, even after I decided to migrate to the private sector and continue my doctorate as a secondary activity. The academy is not easy, especially when it is not carried out exclusively, but Alejandra's efforts and understanding made the process easier. To Alejandra and Kepler, my thanks.

I would like to thank the Department of Astronomy, the UFRGS Physics Institute (IF-UFRGS), and the Postgraduate Program in Physics (PPGFís) for the structure, materials, and support necessary for the development of this research. Also, to CNPq for financing the scholarship and CAPES for financial support. I also thank Dr. Alina Istrate for her mentoring, advice, and her help with the development of computational models. I thank the developers of the MESA and GYRE software, especially Dr. Bill Paxton and Dr. Richard Townsend, for ensuring open-source software and supporting its use. Open source software and programming languages are widely used in academia and rarely receive due credit, so here are my thanks to the main tools used, such as the `Python 3` language, the Ipython kernel, the Jupyter project and the packages Matplotlib, Pandas, and the Scipy ecosystem. Also, my thanks to the StackOverflow community and related websites, which were fundamental in resolving doubts about code bugs and various computational problems that arose throughout undergraduate and postgraduate studies.

Finally, my most sincere thanks to my wife Chaiana. Since the first day of our relationship, which began in 2011, you have encouraged, advised, and helped me to converge my divergent focus on studies. A doctorate requires great dedication from the student and the people around them, even more so when the doctorate is done in conjunction with a full-time work. I thank you for everything you had to give up during these years and for all the affection, friendship, understanding, patience, fun, and love. This thesis is for you.

Portuguese

Perseguir o caminho acadêmico é um sonho antigo. Eu decidi que eu iria perseguir esse caminho em torno dos meus 17 anos, quando percebi que a pesquisa básica e um ambiente de constante aprendizado era o que me fazia feliz e o que eu queria para o meu futuro. Essa decisão foi incentivada pelo meio em que eu estava, uma escola técnica com cobrança semelhante a faculdade e incentivo a pesquisa, bons professores de física e química, um ótimo exemplo de cientista na família e ser criado por pais que sempre acreditaram no meu potencial e que nunca mediram esforços para garantir que eu pudesse me dedicar as minhas escolhas de vida. Aos meus professores de escola técnica, ao meu padrinho Jackson, aos meus pais, Eliane e Sandro, ao meu irmão Guilherme, ao meu tio Émerson e aos meus avós, Rudy e Carmelita, meu muito obrigado.

Na graduação, a primeira oportunidade de trabalhar com pesquisa me foi dada pelo Prof. Dr. Matheus J. Lazo, e que mesmo eu não seguindo na linha de pesquisa dele, sempre foi um ponto de apoio nas principais dúvidas sobre física e continua sendo até hoje uma referência em conhecimento teórico sobre os mais diversos tópicos. Posteriormente, já nos

Estados Unidos, o Prof. Dr. Shashi Kanbur me apresentou o fantástico mundo das estrelas variáveis e me deu oportunidades de pesquisas e colaboração além das minhas expectativas. O Shashi é um grande exemplo de mentor, pois sempre buscou oportunidades para seus alunos e sempre demonstrou paixão pela pesquisa básica. No final da minha graduação, ao retornar para o Brasil, o Prof. Dr. Fabricio Ferrari me acolheu, pois embora estrelas variáveis não fossem o seu tópico de pesquisa, o seu conhecimento em processamento de sinal digital foram fundamentais para lapidar meu trabalho e garantir a minha posição de aluno no mestrado da UFRGS. Aos professores aqui mencionados e aos demais que participaram da minha formação, assim como aos colegas de graduação, em especial ao Vinicius Becker, meu muito obrigado.

Durante a pós-graduação, ingressei no mestrado sob a tutela da Profª. Drª. Alejandra Romero e coorientado pelo Prof. Dr. Kepler de Souza Oliveira Filho. A compreensão sobre o Universo, conhecimento sobre diversos temas e a dedicação em garantir acesso à informação aos alunos fornecida pelo Kepler é inestimável e fundamental para garantir uma pesquisa de qualidade. Durante o doutorado, tive a oportunidade de trabalhar em outros países, viagens que foram fundamentais para garantir conhecimento e colaborações que impactaram neste trabalho. Tais oportunidades não seriam obtidas sem todos os esforços da Alejandra em ajudar, orientar e me incentivar, mesmo após eu decidir em migrar para o ambiente corporativo e continuar o doutorado como uma atividade secundária. O ambiente acadêmico não é nada fácil, principalmente quando não é efetuado em dedicação exclusiva, mas os esforços e compreensão da Alejandra facilitaram e fizeram com que o processo fosse mais leve. A Alejandra e ao Kepler, meus agradecimentos.

Agradeço ao Departamento de Astronomia, ao Instituto de Física da UFRGS (IF-UFRGS) e ao Programa de Pós-Graduação em Física (PPGFís) pela estrutura, materiais e suporte necessários ao desenvolvimento desta pesquisa. Também, ao CNPq pelo financiamento da bolsa e a CAPES pelo suporte financeiro. Também agradeço a Dra. Alina Istrate pela mentoria, conselhos e toda a ajuda com o desenvolvimento de modelos computacionais. Agradeço aos desenvolvedores dos softwares MESA e GYRE, em especial ao Dr. Bill Paxton e ao Dr. Richard Townsend, por garantirem software de código aberto e darem suporte a utilização dos mesmos. Os softwares e linguagens de programação de código aberto são amplamente utilizados na academia e raramente recebem os créditos devidos, portanto seguem aqui meus agradecimentos as principais ferramentas utilizadas, como a linguagem `Python 3`, o kernel Ipython, o projeto Jupyter e as bibliotecas Matplotlib, Pandas e o ecosistema Scipy. Também, meus agradecimentos a comunidade do StackOverflow e sites relacionados, que foram fundamentais para resolverem dúvidas de bugs de códigos e diversos problemas computacionais que surgiram ao longo da graduação e pós-graduação.

Por fim, meus mais sinceros agradecimentos à minha esposa, Chaiana. Desde o

primeiro dia do nosso relacionamento, que começou em 2011, tu me incentivas, aconselha e me ajuda a convergir meu foco divergente aos estudos. O doutorado exige uma grande dedicação do aluno e das pessoas na sua volta, ainda mais quando o doutorado é feito em conjunto com um trabalho de turno integral no setor privado. Te agradeço por tudo que tu tiveste que abdicar durante esses anos e por todo o carinho, amizade, compreensão, paciência, diversão e amor. Esta tese é dedicada a ti.

The Road goes ever on and on
Out from the door where it began.
Now far ahead the Road has gone,
Let others follow it who can!
Let them a journey new begin,
But I at last with weary feet
Will turn towards the lighted inn,
My evening-rest and sleep to meet.
(The Road Goes Ever On, J.R.R. Tolkien)

Abstract

White dwarf stars are the most common final stage of stellar evolution, corresponding to 99% of all stars in the Galaxy. Around 10% of white dwarfs in the solar neighbourhood are low-mass ($< 0.45 M_\odot$) objects. In the case of low-mass white dwarfs, up to 70% of them are in binary systems. The total number of stars in such systems increases to 100% when extremely low-mass white dwarfs are considered. The pulsating low-mass white dwarf stars have stellar masses between 0.30 $M_\odot$ and 0.45 $M_\odot$ and show photometric variability due to gravity-mode pulsations. Within this mass range, they can harbour both a helium- and hybrid-core, depending if the progenitor experienced helium-core burning during the pre-white dwarf evolution. The eclipsing binary system SDSS J115219.99+024814.4 is composed of two low-mass white dwarfs with stellar masses of 0.362 ± 0.014 $M_\odot$ and 0.325 ± 0.013 $M_\odot$. The less massive component is a pulsating star, showing at least three pulsation periods of $\sim$1314 s, $\sim$1069 s, and $\sim$582.9 s. This opens the way to use asteroseismology as a tool to uncover its inner chemical structure, in combination with the information obtained using the light-curve modeling of the eclipses. By means of binary evolutionary models leading to helium- and hybrid-core white dwarfs, we computed adiabatic pulsations for $\ell = 1$ and $\ell = 2$ gravity modes with `GYRE`. We found that the pulsating component of the SDSS J115219.99+024814.4 system must have a hydrogen envelope thinner than the value obtained from binary evolution computations, independently of the inner composition. Finally, from our asteroseismological study, we find a best fit model characterised by $T_{\rm eff} = 10\,917$ K, M=0.338 $M_\odot$, $M_H = 10^{-6}$ $M_\odot$ with the inner composition of a hybrid white dwarf.

Keywords: asteroseismology; white dwarf; binary system.

Resumo

As estrelas anãs brancas são o estágio final mais comum da evolução estelar, correspondendo a 99% de todas as estrelas da Galáxia. Em torno de 10% das anãs brancas da vizinhança solar são objetos com baixa massa ($< 0.45 M_\odot$). No caso destes objetos, até 70% delas pertencem a sistemas binários. Este percentual aumenta para 100% quando consideramos as anãs brancas de massas extremamente baixas ($< 0.3 M_\odot$). As anãs brancas pulsantes de baixas massas possuem massas estelares entre 0.30 $M_\odot$ e 0.45 $M_\odot$, e apresentam variabilidade fotométrica devido a modos-g de pulsações. Dentro dessa faixa de massa, essas estrelas podem vir a ter núcleos de hélio ou híbridos, dependendo se as progenitoras tiveram queima de hélio no núcleo durante a fase evolutiva de pré-anã branca. O sistema binário eclipsante SDSS J115219.99+024814.4 é composto por duas anãs brancas de baixas massas, 0.362±0.014 $M_\odot$ e 0.325±0.013 $M_\odot$. A componente menos massiva é uma estrela pulsante que apresenta pelo menos três períodos de pulsações, sendo de ∼1314 s, ∼1069 s and ∼582.9 s. Estes períodos permitem utilizar a astrossismologia como uma ferramenta para revelar a estrutura química interna em conjunto com a informação extraída das curvas de luz dos eclipses. Através de modelos evolutivos de binárias que geraram anãs brancas com núcleos de hélio e híbrido, foram calculadas pulsações adiabáticas para modos de gravidade com $\ell = 1$ e $\ell = 2$, utilizando o software `GYRE`. Foi descoberto que, independente da composição do núcleo, a componente pulsante do sistema SDSS J115219.99+024814.4 deve possuir um envelope de hidrogênio mais fino do que o previsto pelos cálculos evolutivos para uma componente de sistema binário. Além disso, a partir do estudo astrossismológico, foi descoberto que o melhor modelo que descreve a componente pulsante possui um núcleo híbrido e as seguinte características: $T_{\rm eff} = 10\,917$ K, M=0.338 $M_\odot$, $M_H = 10^{-6}$ $M_\odot$.

Palavras-chave: astrossismologia. anã branca. sistemas binários.

List of Figures

List of Tables

List of abbreviations and acronyms

AGB	Asymptotic Giant Branch
CE	Common Envelope
CS	Cooling Sequence
COROT	Convection, Rotation and Planetary Transits
ELM	Extremely low mass white dwarfs
EOS	Equation of State
HB	Horizontal Branch
HELM	Timmes & Swesty (2000) table of equation of state
HIPPARCOS	HIgh Precision PARallax COlleting Satellite
HR	Hertzsprung-Russell diagram
LM	low mass white dwarfs
MESA	Modules for Experiments in Stellar Astrophysics
MLT	Mixing Length Theory
MS	Main Sequence
OGLE	The Optical Gravitational Lensing Experiment
OPAL	Rogers & Nayfonov (2002) table of equation of state
OPD	Pico dos Dias Observatory
RGB	Red Giant Branch
RLOF	Roche Lobe overflow
SDSS	Sloan Digital Sky Survey
SOAR	Southern Astrophysical Research
SRLOF	Stable Roche Lobe overflow
TESS	Transiting Exoplanet Survey Satellite

ZAMS	Zero Age Main Sequence
WET	Whole Earth Telescope
WMP	Weighted Mean Period

List of symbols

a_k	Lagrangian acceleration at cell face k
DA	Type of white dwarf with H-atmosphere
DB	White dwarf with He-atmosphere and effective temperature of $11\,000 - 30\,000$ K
DC	White dwarf with He-atmosphere, traces of carbon and effective temperature below $\sim 11\,000$ K
$D_{\mathrm{conv},0}$	MLT derived diffusion coefficient
DO	White dwarf with He-atmosphere and effective temperature of $45\,000 - 200\,000$ K
DQ	White dwarf with He-atmosphere, traces of metals and effective temperature below $\sim 11\,000$ K
f	Adjustable parameter for overshooting
HeI	Neutral helium
HeII	Singly ionized helium
K	Unit Kelvin
L_k	Luminosity interior to cell face k
m_k	Mass interior to cell face k
$M_\odot$	Solar Mass
M_{ZAMS}	Mass at ZAMS
P_k	Pressure at cell k
r_k	Radius interior to cell face k
$R_\odot$	Solar Radius
t	Time
T_{eff}	Effective Temperature
T_k	Temperature at cell k

v_k	velocity interior to cell face k
$X_{i,k}$	Mass fraction of element i at cell k
Z	Metallicity
ε_{nuc}	Nuclear energy
η	Mass loss efficiency parameter
κ	Opacity
ρ_k	Densitity at cell k
σ_k	Lagrangian diffusion coeficient at cell k
F_k	Mass flow rate at cell k
ϕ	Effective gravitational potential energy
Ω	Angular rotation velocity
f'	Eulerian perturbation of a variable f
k	Radial order
ℓ	Harmonic degree
m	Azimuth order
$Y_\ell^m(\theta, \phi)$	Spherical harmonics
$\sigma_{k,\ell,m}$	Angular frequency
L_ℓ^2	Lamb frequency
c_S^2	Adiabatic local sound speed
N^2	Brunt-Väisälä frequency
Φ	Gravitational potential
$\Delta\sigma^a$	Asymptotic frequency spacing
$\Delta\Pi_\ell^a$	Asymptotic period spacing
$C_{k,\ell}$	Rotational spliting coefficient
M_d	Donor star mass
M_c	Accretor star mass

r_1	Distance of star 1 from the center of binary the system
r_2	Distance of star 2 from the center of binary the system
ω	Angular frequency
P	Orbital period
L_1	Inner Lagrangian point
R_L	Roche Lobe radius
β	Fraction of transfered mass
J	Orbital angular momentum

Contents

1 Introduction

1.1 Stellar Evolution

In this section, we will review the theory of stellar evolution. A detailed discussion on this topic can be found on the works of Kepler & Saraiva (2017), Maciel (2016), and Cox & Giuli (1968). For a full description of binary evolution, the reader is referred to Carroll & Ostlie (2014), Hilditch (2001), and Eggleton (2006).

1.1.1 Single Stellar Evolution

Stars are born from massive gas clouds that collapse due to self-gravity. In the contraction, gravitational potential energy is released and partly transformed into thermal energy, heating the matter which composes the protostar. If in virial equilibrium, half of the potential energy is released as radiation. Eventually, the central region reaches density and temperature high enough to start burning hydrogen into helium at the core. The released energy from nuclear reaction balances the gravitational contraction and the protostar enters the *Zero Age Main Sequence* (ZAMS). If the protostar mass is lower than 0.08 $M_{\odot}$, for solar composition, it will never reach the threshold temperature ($T \sim 6 \times 10^6$ K) to start the hydrogen burning. In this case, the matter becomes degenerate and its pressure balances the gravitational contraction, which prevents further heating hence forming a brown dwarf.

The stage where the star first ignites hydrogen is known as ZAMS and the entire process of core H-burning is known as *Main Sequence* (MS), the longest stage in stellar evolution, before the last compact state. In the MS, the star is in hydrostatic equilibrium due to the balance between thermonuclear energy and gravitational contraction. For larger initial masses, the release of energy from nuclear reactions is larger, resulting in higher luminosities and a shorter lifetime in the MS. For example, a 20 $M_{\odot}$ initial mass star has a MS lifetime of $\sim 6 \times 10^6$ years while a 1 $M_{\odot}$ star has a lifetime of $\sim 10^{10}$ years. When hydrogen is extinguished in the core, the stars are left with a helium core surrounded by a layer of hydrogen burning. At this stage, the MS is over.

After the end of the MS, the stellar core contracts and the envelope expands. This expansion reduces the effective temperature and the star enters the *Red Giant Branch* (RGB). In this stage, the star increases its luminosity at almost constant temperatures. The mass of the inert helium core increases as the star burns hydrogen in the surrounding layers. This increase in core mass leads to more contraction and larger temperatures. When the core temperature reaches $\sim 10^8$ K the star starts to burn helium into carbon and

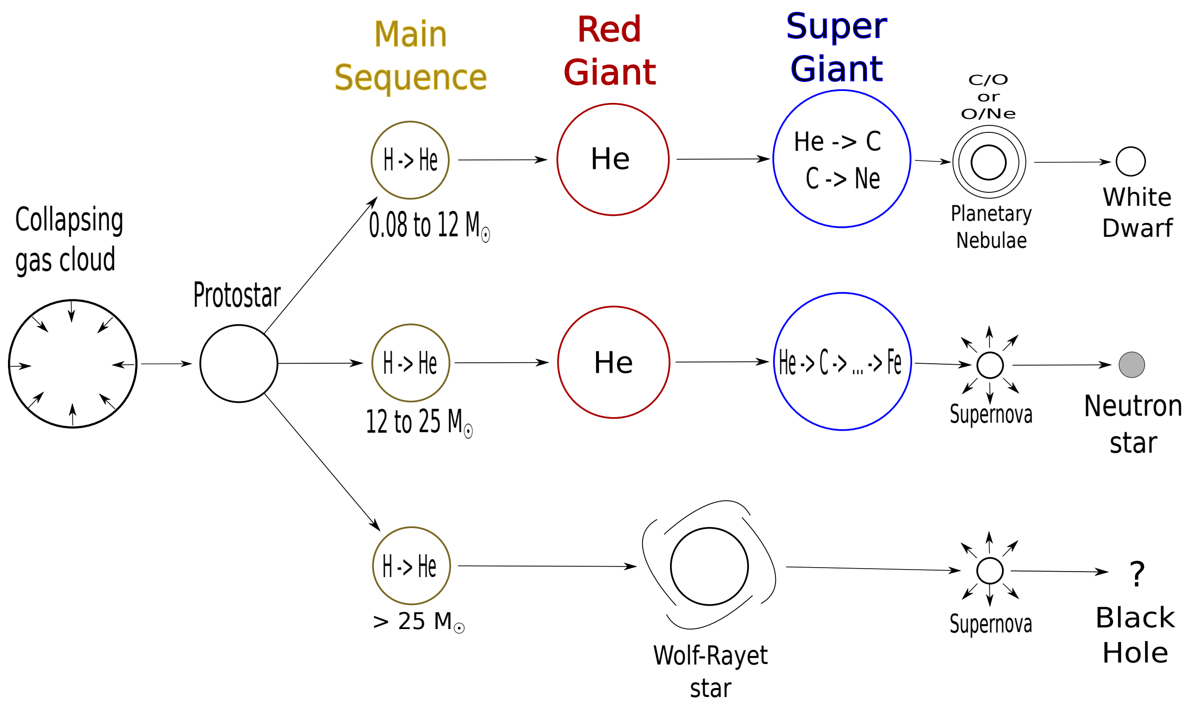

Figure 1 – A Scheme of the evolutionary paths a single star may follow, depending on its mass.

oxygen. This stage is known as *Horizontal Branch* (HB).

The subsequent evolutionary stages after the HB depend on the metallicity and stellar mass at the beginning of the MS. Hence, for solar metallicity, the stars can be divided into three groups: stars with initial masses between 0.08 $M_{\odot}$ and ~ 12 $M_{\odot}$; stars with masses in a range of ~ 12 to 25 $M_{\odot}$; and massive stars with masses greater than ~ 25 $M_{\odot}$. A schematic view of the three possibles paths of single stellar evolution is shown in Figure 1.

For stars with initial masses between 0.08 $M_{\odot}$ and ~ 12 $M_{\odot}$, after core He burning, they develop a degenerate core of carbon and oxygen surrounded by a layer of helium burning. On top of the helium layer, the star still has a hydrogen burning layer. As there are no nuclear reactions in the core, the core contracts, and the regions between the burning layer expand. Thus, the envelope expands and the star enters the *Asymptotic Giant Branch* phase (AGB), reaching higher luminosities. In our models, stars with initial masses $M_{ZAMS} < 9$ $M_{\odot}$ the core never reaches a temperature high enough to burn carbon ending as a carbon/oxygen core. This happens because the carbon/oxygen core density becomes high enough to form a degenerate gas, and the neutrinos produced in the core are radiated away without interacting with matter, reducing the temperature in the core. Stars with initial masses of $M_{ZAMS} = 9 \sim 12$ $M_{\odot}$ burn carbon resulting in a core composed of oxygen/neon or oxygen/neon/magnesium for the more massive cases. At the end of the

AGB, the He-burning layer becomes unstable and the star undergoes a series of thermal pulses. As the evolution proceeds through the AGB, the core mass increases due to the He-burning on the surrounding layer. Also, the mass loss due to thermal pulses and radiation pressure expels almost the entire envelope together with most of the hydrogen. This leaves a star with a degenerate core and a small envelope with a radius comparable to the Earth's size. The ejected material around the remaining star shines for 10 to 100 thousand years as a *Planetary Nebula* due to the absorption of the ultraviolet radiation emitted from the central object, before dissipating into the interstellar medium. The final result is a *White Dwarf* star.

For the case of stars with masses in range of $\sim 12 - 25\ M_{\odot}$, after the stars burn all helium in the core, the core does not become degenerate. This allows a series of nuclear reactions, from carbon burning to iron burning, without changing the outer layers. These series of reactions last for hundreds of years. As a result, the star creates a layered structure, with layers of increasingly heavy elements towards the center. Once the star produces an iron core, energy production from nuclear sources stops, since iron fusion is an endothermic reaction. Thus, the only source of energy is the gravitational contraction, which increases the core temperature and causes the dissociation of the atomic nuclei into protons and neutrons. With increasing density, the protons capture electrons forming neutrons and emitting neutrinos, finally forming a degenerate gas. This gas becomes incompressible and stops the gravitational collapse of the outer layers. As a result, a shock wave is generated, and together with neutrino emission, transfers momentum to the envelope, expelling the outer layer in a *Supernova* (SN) explosion that lasts for a couple of minutes. The remaining core transforms into a *neutron star*, with mass between 1.4 $M_{\odot}$ to $\sim 2.2\ M_{\odot}$. The upper limit depends on the equation of state of nuclear matter, still uncertain, on rotation and magnetic field.

Last, stars with initial masses greater than $\sim 25\ M_{\odot}$ become luminous *Wolf-Rayet* stars. As the massive star evolves, the processed material in the core gradually reaches the surface due to convection. When a sufficient amount accumulates on the surface, it absorbs almost the entire emitted radiation producing strong winds, with mass-loss rates of order $10^{-6} - 10^{-5}\ M_{\odot}$year. These winds hide the stars. It is believed that the process occurring in the interior of massive stars is similar to the intermediate-mass stars, with the layered structure and iron core leading to a Supernova event. In this case, the mass of the remaining core exceeds the upper mass limit for neutron stars, hence the gravitational contraction is higher than the pressure from the degenerate neutron gas. The contraction of the core leads to a *Black Hole* or total disruption of the star.

The star Formation Rate is not the same for the entire mass range. According to the *Initial Mass Function*, for each 10 $M_{\odot}$ star that is born, there are ≈ 300 stars with 1 $M_{\odot}$ (Salpeter, 1955). Hence, the white dwarf stars are the most common final stage of stellar evolution.

1.1.2 Binary Evolution

A binary system is composed of two stars bound by gravity. If their orbital separation is sufficiently large, i.e larger than the radius on the AGB, each component of the system will evolve as a single star, which defines a *Wide Binary System*. On the other hand, if their separation is not large enough to prevent interactions due to the evolutionary expansion, the system is called a *Close Binary System*. In such systems, the interactions occurs due to mass and angular momentum exchange between the stars. How they interact and the number of interactions will impact the structural properties and evolution of the system.

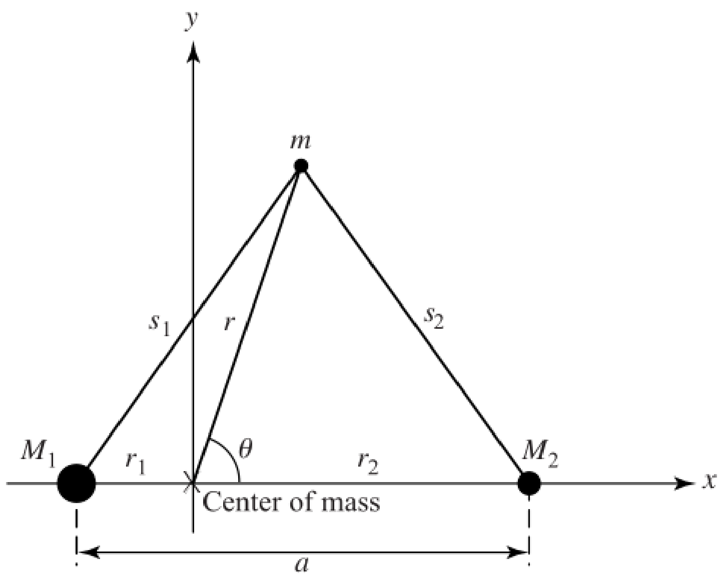

Figure 2 – The coordinate system for a binary system. Adapted from Carroll & Ostlie (2014).

To understand such interactions it is necessary to study the effective gravitational potential energy ϕ of a binary system. We will consider two stars, with masses M_1 and M_2, in a circular orbit in the $x-y$ plane, as shown in Figure 2. The stars are separated by a distance $a = r_1 + r_2$, where r_1, r_2 are the distance of star 1 and 2 to the center of mass of the system. For a small test mass m, with distance r from the center of mass and distance s_1, s_2 from stars 1 and 2, the effective gravitational potential is

$$\phi = -G\left(\frac{M_1}{s_1} + \frac{M_2}{s_2}\right) - \frac{1}{2}\omega^2 r^2 \quad , \tag{1.1}$$

where s_1 and s_2 are given by the law of cosines:

$$s_1^2 = r_1^2 + r^2 + 2rr_1\cos\theta \tag{1.2}$$

$$s_2^2 = r_2^2 + r^2 + 2rr_2\cos\theta \quad , \tag{1.3}$$

The angular frequency of the orbit ω is given from Kepler's third law:

$$\omega^2 = \left(\frac{2\pi}{P}\right)^2 = \frac{G(M_1 + M_2)}{a^3} \quad , \tag{1.4}$$

where $P = 2\pi/\omega$ is orbital period.

These equations can be used to evaluate the effective gravitational potential at every point in the orbital plane. Figure 3 shows the equipotential contours, or points in space that share the same value of ϕ, and the Lagrangian points, where there is no net force on the test mass, along the $x - y$ plane. The Lagrangian points are unstable equilibrium points since they are local maxima of ϕ.

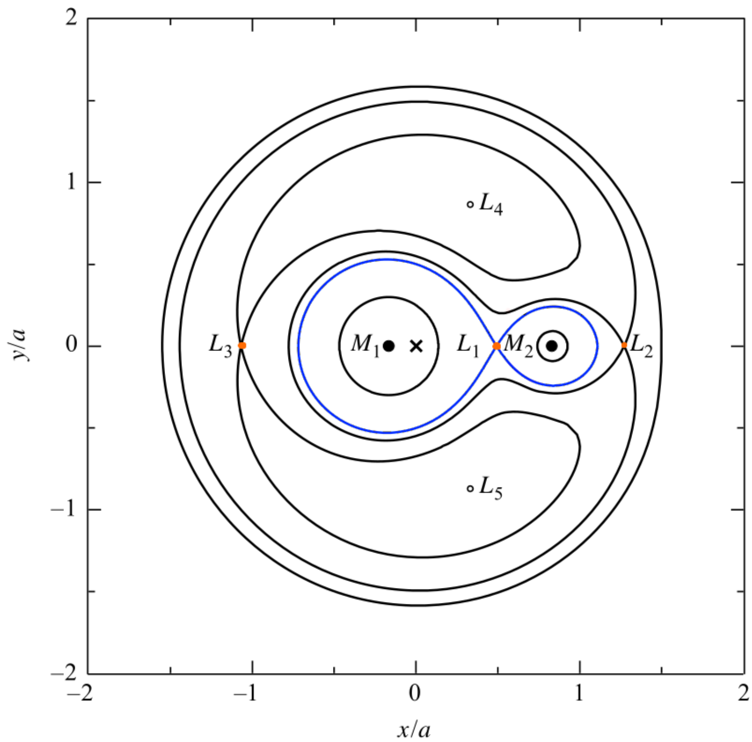

Figure 3 – Equipotential contours for a binary system. The $\times$ is the center of mass. Orange dots are the Lagrangian points and the blue contour is the Roche Lobe. Adapted from Carroll & Ostlie (2014).

Along the evolution of the stars in the system, they can expand and fill successively larger equipotential surfaces. If one star expands enough to fill the teardrop-shaped regions, depicted as a blue contour in Figure 3, then part of its envelope can escape towards its companion through the inner Lagrangian point L_1. These regions bounded by the blue contour line are called *Roche Lobes*. The Roche lobe radius R_L can be evaluated numerically, within 1% uncertainty, by the expression

$$R_L = \frac{0.49q^{2/3}a}{0.6q^{2/3} + \ln(1 + q^{1/3})} \quad , \tag{1.5}$$

where $q = M_1/M_2$ (Eggleton, 1983). The *Roche lobe overflow* (RLOF) begins when one of the stars has expanded enough such its radius becomes equal to R_L.

A binary system is called *Semidetached* when one of the stars has expanded beyond its Roche lobe and starts to transfer mass. However, both stars can fill and expand beyond their Roche lobes simultaneously. In the case where both stars fill their Roche lobes, the system is called a *Contact* binary. Finally, if both stars expand beyond their Roche lobes, the system is known as *Common envelope* and the two stars share a common atmosphere bounded by the equipotential surface immediately larger than the Roche lobe surface.

The interaction between the stars in a close binary system can happen through mass and angular momentum exchange. When mass transfer starts, the final mass of a star in such system no longer depends only on its initial mass and metallicity at ZAMS. The mass transfer starts when one of the stars, with mass M_d and called *Donor*, expands enough to fill its Roche Lobe radius (R_L). The mass is transferred through the L_1 Lagrange point to the companion, or *Accretor* with mass M_a. The mass transfer rate can be defined as

$$\dot{M}_a = -\beta \dot{M}_d \ , \quad 0 \leq \beta \leq 1 \quad , \tag{1.6}$$

where β measures the fraction of the transferred mass that is accreted. The residual $(1-\beta)$ gives the amount of material that is lost to the interstellar medium. The mass transfer is conservative when $\beta = 1$, or non-conservative otherwise. In the conservative case, where no mass is lost from the system, the orbital angular momentum of the binary (J), given by

$$J = M_a M_d \frac{\sqrt{Ga}}{M_a + M_d} \quad , \tag{1.7}$$

is conserved, hence $\dot{J} = 0$. By differentiating 1.7 we obtain an equation for the orbital evolution of the system:

$$\frac{\dot{J}}{J} = \frac{1}{2}\frac{\dot{a}}{a} + \frac{\dot{M}_a}{M_a} + \frac{\dot{M}_d}{M_d} - \frac{\dot{M}_a + \dot{M}_d}{2(M_a + M_d)} \quad . \tag{1.8}$$

Applying the conditions for the conservative case, $\dot{J} = 0$ and $\dot{M}_a = -\dot{M}_d$, the above expressions becomes:

$$\frac{\dot{a}}{a} = 2\frac{\dot{M}_d}{M_d}\left(\frac{M_d}{M_a} - 1\right) \quad , \tag{1.9}$$

where $\dot{M}_d < 0$ by definition. In the case $M_d/M_a < 1$ where the donor is less massive than the accretor, the Roche Lobe radius (R_L) and the orbit expands ($\dot{a} > 0$). This scenario is known as *Stable Roche Lobe Overflow (SRLOF) channel.* As R_L increases the mass transfer stops until it fills its new R_L. However, in the case where the donor is more massive than the accretor, $M_d/M_a > 1$, the orbit and R_L decreases ($\dot{a} < 0$). The mass transfer becomes unstable as the donor‘s companion can not accrete all the material, which stacks on top of the accretor. The accretor starts to expand beyond its Roche Lobe radius, leading to a common envelope. This scenario is known as *Common Envelope (CE) channel.*

1.1.3 White Dwarf Stars

White dwarf stars are the most common final stage of stellar evolution. They are the end product of MS stars with masses up to $5 - 11.8$ M$_\odot$ (García-Berro; Isern; Hernanz, 1997; Poelarends et al., 2008; Siess, 2010; Langer, 2012; Woosley; Heger, 2015; Doherty et al., 2015; Lauffer; Romero; Kepler, 2018), depending on metallicity. Considering the upper limit for solar metallicity, $M = 12\ M_\odot$, the percentage of white dwarf stars in the Galaxy can be calculated by the Salpeter Initial Mass Function (Salpeter, 1955):

$$\int_{0.1}^{12} 0.06 M^{-2.35} \mathrm{d}M = \frac{0.06}{1.35}\left(0.1^{-1.35} - 12^{-1.35}\right) = 0.9934 \tag{1.10}$$

hence, 99% of all stars in the Galaxy will become white dwarf stars.

White dwarf usually start their lives as hot cores remnants of a planetary nebula. Then, as there are no nuclear reactions, the star starts to cool. The pressure from the degenerate core balances the gravitational force leading to a final evolution with an almost constant radius. The degenerate core in the relativistic regime is responsible for the upper mass limit of white dwarf stars, known as the *Chandrasekhar limit*, with a value of $\sim 1.4\ M_\odot$ (Chandrasekhar, 1931). Corrections due to general relativity and neutron dripping lead to an upper limit of $1.36\ M_\odot$, while magnetic field and rotation can significantly increase the limiting mass.

From an spectroscopic point of view, white dwarf stars can be divided into two main classes: DA and non-DA types, based on the main component of their atmosphere. The DA spectral class shows a hydrogen-rich atmosphere and represents $\simeq 85\%$ of all white dwarfs while non-DA have hydrogen deficient and helium-rich atmospheres (Fontaine; Brassard, 2008; Althaus et al., 2010b). The helium-rich white dwarfs are believed to be a progeny of PG 1159 stars (McGraw et al., 1979) formed by a Born-Again episode (Schoenberner, 1979; Iben JR. et al., 1983) in which a helium flash occurs during the cooling sequence (i.e. very late thermal pulse) forcing the star to evolve back to the AGB. As a result, this very late thermal pulse burns out all hydrogen left in the atmosphere of the star. The non-DA white dwarfs can be classified by the dominant element in the atmosphere and effective temperature: DO class with strong lines of singly ionized helium (HeII) and effective temperatures of $T_{eff} \approx 45\ 000 - 200\ 000$ K; DB class with strong lines of neutral helium (HeI) and $T_{\rm eff} \approx 11\ 000 - 30\ 000$ K, and for effective temperatures bellow $T_{eff} \approx 11\ 000$ K there are DC with no lines, and DQ and DZ types with traces of carbon and metals in their spectra, respectively. Along the evolution of a DO-type white dwarf, the HeII recombines to form HeI and become a DB white dwarf. The transition from a DO to a DB white dwarf ($32\ 000\ K < T_{\rm eff} < 45\ 000\ K$) is known as *DB Gap* (Liebert et al., 1986; Liebert; Fontaine; Wesemael, 1987), a region where few objects are observed with a hydrogen deficient atmosphere (Kleinman et al., 2013). Also, the hot DQ type, or white dwarfs with carbon-rich atmosphere and $T_{eff} \approx 20\ 000\ K$ are believed to be a cold descendant of PG 1159 stars formed by mixing between the outer He convection zone with the underlying convective carbon intershell at cold temperatures (Dufour et al., 2007; Dufour et al., 2008; Althaus et al., 2009). A scheme of the possible evolutionary paths that a white dwarf may follow is shown in Figure 4.

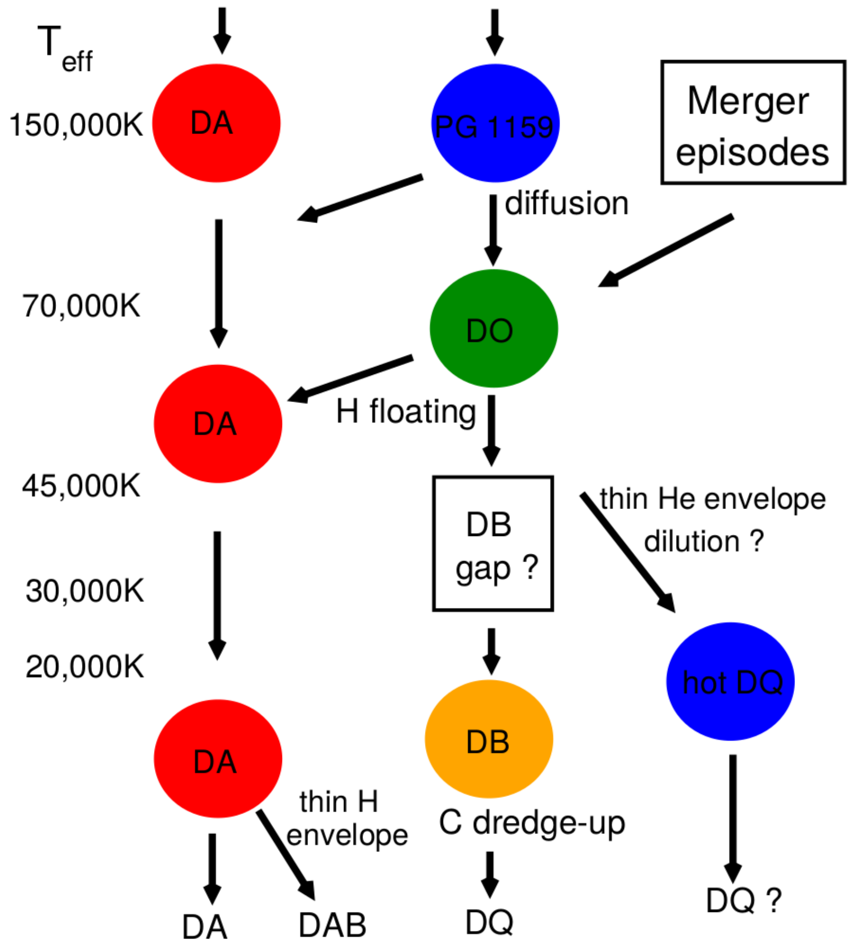

Figure 4 – A scheme of the evolutionary paths a white dwarf may follow. The left column indicates the effective temperature. The second column presents the evolution of the most common type of white dwarf (DA spectral type). The DO type may follow different paths, either from a merger event or from a hot and helium-, carbon-, and oxygen-rich PG 1159 star. The PG 1159 stars are also believed to be the progenitors of hot DQ stars. Accretion of metal from interstellar medium or circumstellar matter by cool helium-rich white dwarf may lead to a DZ white dwarf. Adapted from Althaus et al. (2010b).

The number of spectroscopically confirmed white dwarf stars has increased to more than ≈ 30 000 with surveys like the *Sloan Digital Sky Survey* (SDSS) (Ahn et al., 2014), which allows us to study the mass distribution of white dwarf stars. Figure 5 shows a density distribution versus stellar mass DA white dwarfs from the SDSS data release 12 (Kepler et al., 2016). The mass distribution is centered at 0.649 $M_\odot$, which represents ∼ 84% of the total sample. There are two additional peaks, one at higher masses, centered at ≈ 0.811 $M_\odot$, and a second at lower masses, centered at ≈ 0.39 $M_\odot$ (Kleinman et al., 2013; Kepler et al., 2007; Kepler et al., 2015).

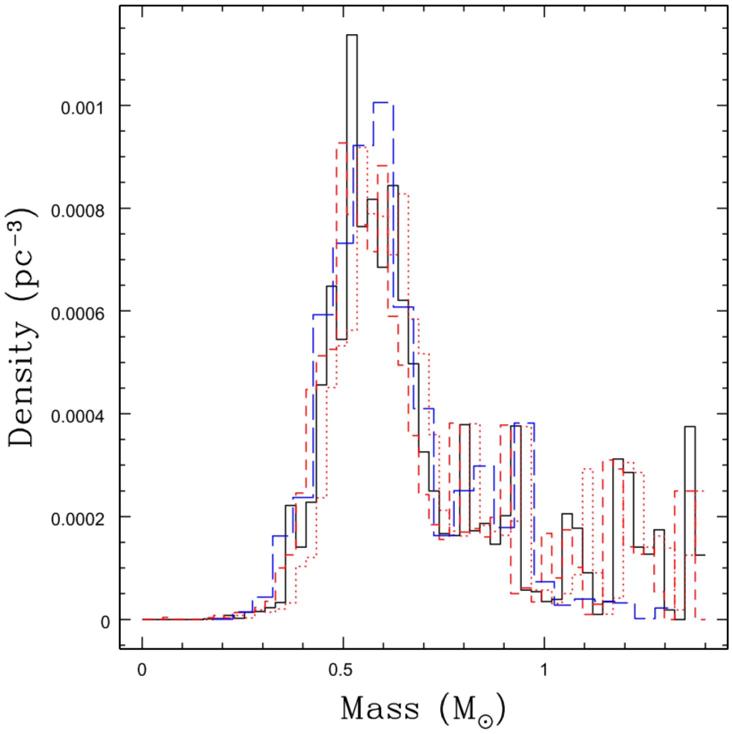

Figure 5 – Histogram for the number density distribution of white dwarfs versus mass on the SDSS data release 12. Red lines show the -1σ and $+1\sigma$ uncertainties. The long dashed blue histogram is the one from Rebassa-Mansergas et al. (2015). Adapted from Kepler et al. (2016).

The low-mass tail extends to stellar masses as low as 0.2 M$_\odot$ and up to 0.45 M$_\odot$. White dwarf stars with masses below 0.3 M$_\odot$ are end products of close binary systems since single star evolution predicts that the progenitors of those stars have a main sequence evolution time larger than the age of the Universe (Kilic; Stanek; Pinsonneault, 2007; Pelisoli; Vos, 2019). These objects are known as *Extremely Low-Mass White Dwarfs* (ELMs) and are expected to harbour helium cores.

In the mass range of 0.3 – 0.45 M$_\odot$, the objects are known as *Low-Mass White Dwarfs* (LM). These objects are most likely formed due to strong mass–loss episodes at the Red Giant Branch phase before the occurrence of the He–flash. For high metallicity progenitors, enhanced mass loss due to high opacity can lead to low mass remnants. On the other hand, for solar metallicity progenitors, mass–loss episodes must occur in interacting binary systems through mass–transfer (Kilic; Stanek; Pinsonneault, 2007; Istrate et al., 2016). The LM white dwarfs can harbour either a helium core or a hybrid core, composed of helium, carbon, and oxygen (Panei et al., 2007; Prada Moroni; Straniero, 2009; Althaus; Miller Bertolami; Córsico, 2013; Istrate et al., 2014; Zenati; Toonen; Perets, 2019).

In recent years, the increase interest in LM and ELM white dwarfs gave rise to surveys dedicated to search for those stars, such as the ELM Survey (Brown et al.,

2010) with 98 identified ELMs with surface gravity $4.71 \leq \log g[\mathrm{cm/s^2}] \leq 7.76$, effective temperature of $7\,940 \leq T_{\mathrm{eff}}[\mathrm{K}] \leq 34\,270$ and mass $0.142 \leq M/M_{\odot} \leq 0.497$ (Brown et al., 2016). Brown et al. (2020) also found that 100% of the ELM white dwarfs in their sample are double white dwarf binaries with orbital periods of $0.0089 < P[\mathrm{days}] < 1.5$. Moreover Brown et al. (2011) found that the fraction of single LM white dwarf is less than 30% in their sample of 30 LM white dwarfs from the Palomar-Green survey (Green; Schmidt; Liebert, 1986).

1.2 Stellar Pulsations

Stars are dynamic and active objects that experience major changes in their internal structure along their evolution. Those internal changes modify the physical properties that lead to a variation in the luminosity of the star. When that happens a star is called a *Variable Star*. Those oscillations can last from minutes to months and can happen in almost all types of stars and in many stages of the stellar evolution.

Variable stars can be divided into two main groups: Intrinsic and Extrinsic Variables. When the change in luminosity is due to the varying physical properties, the star is part of the Intrinsic Variable group. This group encompasses the pulsating variables (periodical change in shape and size), eruptive variables (change in luminosity from extreme mass loss, or eruptions), and cataclysmic variables (Nova and Supernova).

The Extrinsic variables present changes in brightness due to external sources and can be further divided into two sub-classes: Eclipsing Variables and Rotational Variables. In an eclipsing binary system, one star blocks partially the light from the companion when the orbital plane is in the line of sight. Rotational variables are rotating stars with nonuniform surface brightness or with a flattened shape, whose rotation axis does not coincide with the line of sight towards the observer.

1.2.1 Stellar pulsations in Intrinsic Variable stars

In general, a star is a stable system in hydrostatic equilibrium. Under some circumstances, a small perturbation in its equilibrium can grow over time and become large enough to be observed as brightness variability. Usually, stellar oscillations are manifested by periodical variations in the star luminosity. However, it can also be manifested by variations in the spectral lines. Those variations can be caused by changes in the stellar radius, superficial temperature, or by a combination of these effects.

The simplest oscillation a star can undergo is the *Radial* type, in which a star expands and contracts radially and periodically, preserving its spherical symmetry. In this type of oscillation, the restoring force is pressure and the stellar material has only radial motions, thus the pulsation modes are pressure (or acoustic) modes *p-modes*. If transverse motion occurs in addition to radial motion, the oscillation is of the *non-Radial* type and presents a *p-mode* and *g-mode* spectra, in which pressure and gravity are restoring forces, respectively.

1.2.2 Basic Equations of Oscillation

In this subsection, a summary of the general properties of non-radial oscillations will be presented. A complete description of the equations that describe the non-radial pulsations in their adiabatic form is presented in Appendix A. For complete details of non-radial pulsations applied to stellar oscillations, it is recommended the work of Unno et al. (1989).

The basic hydrostatic equations that control the non-radial pulsations are: Equation of mass (A.1), momentum (A.2), and energy conservation (A.3). By applying small perturbations on an equilibrium state with spherical symmetry, a system of linear equations is obtained. With this consideration and for a normal mode, a variable f can be described as:

$$f'_{k,\ell,m}(r,\theta,\phi,t) = f'_{k,\ell,m}(r) Y_\ell^m(\theta,\phi) \exp(i\sigma_{k,\ell,m} t) \quad , \tag{1.11}$$

where f' is the Eulerian perturbation of a physical quantity f, $Y_\ell^m(\theta,\phi)$ are the spherical harmonics, $\sigma_{k,\ell,m}$ is the angular frequency and $f'_{k,\ell,m}(r)$ is the radial part of the eigenfunction. Under the adiabatic approximation, in which the specific entropy is conserved ($\delta S = 0$), the set of linear equations that describe the non-radial pulsations is reduced to 4 first-order differential equations given by A.60 to A.63.

Equation 1.11 shows that each normal mode is characterised by three numbers, being the radial order k, the harmonic degree ℓ and the azimuth degree m, which has range of $-\ell \leq m \leq \ell$. The harmonic degree is equal to the number of nodal lines in the star surface and $|m|$ is the number of meridians. The number of parallels is given by $\ell - |m|$. Figure 6 shows the nodal lines for modes with $\ell = 3$ and varying values of m (rows) and inclination (columns) of the star. The left, middle and right columns show inclinations of 30°, 60° and 90°, respectively. The white bands represent the positions of the surface nodes and the red and blue parts represent sections of the stars that are heating and cooling, opposite of each other. The integration of luminosity in different regions of the surface of the star leads to variations in the total luminosity. The top row shows the mode with $m = 0$ where all nodal lines are parallels. The second and third row (from top to bottom) has $m = \pm 1$ and $m = \pm 2$. The bottom row shows $m = \pm 3$ where $\ell = |m|$ and presents only meridians. The increase in the harmonic degree also increases the number of regions separated by nodal lines, which decreases the size of those regions. This gives rise to the phenomenon called *Geometric Cancellation*, in which the variability of the stars becomes too small to be observed. Hence, modes with harmonic degree $\ell > 3$ are difficult to observe in small objects like white dwarf stars.

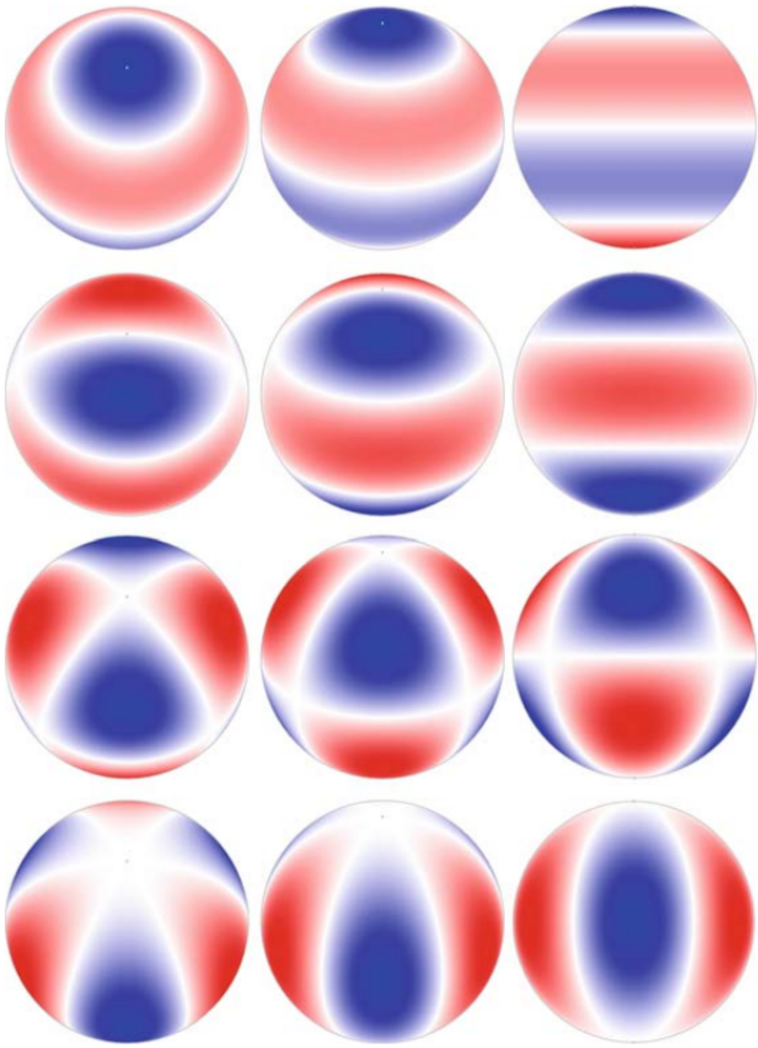

Figure 6 – Nodal lines for modes with $\ell = 3$ and varying values of m (rows) and inclination (columns) of the star. The left, middle and right columns shows inclinations of 30°, 60° and 90°, respectively. The first, second, third and fourth row (from top to bottom) shows m equals to 0, ±1, ±2,±3, respectively. Adapted from Aerts, Christensen-Dalsgaard & Kurtz (2010)

For homogeneous stellar models, the radial order k represents the number of radial nodes, or the number of concentric spherical surfaces with radius r_i ($1 \leq i \leq k$) where the movement of the stellar material is equal to zero. In the absence of rotation, magnetic field, and any other external force, the oscillation equations do not depend explicitly on the azimuth order m. This leads to eigenfrequencies σ^2 that are independent of m and show degeneration of order $2\ell + 1$ on the eigenvalues. Thus, the $2\ell + 1$ normal modes characterized by the same k and ℓ values have the same oscillation frequency.

1.2.3 Properties of non-radial oscillations

As previously mentioned, there are two classes of modes in the non-Radial type of oscillation, the p-modes and the g-modes. They are defined by their restoring force, being the pressure for p-modes and gravity for the g-modes.

The properties of the non-Radial modes are given by their characteristic frequencies. The pressure p-modes are related to the Lamb frequency:

$$L_\ell^2 - \frac{\ell(\ell+1)}{r^2} c_S^2 \quad , \tag{1.12}$$

where c_S^2 is the adiabatic local sound speed, given by $c_S = \sqrt{\Gamma_1 P/\rho}$. The Lamb frequency is inversely proportional to the time a sound wave takes to travel a distance $\lambda_\ell = 2\pi r/\ell$. The p-modes show radial motion in the stellar material and the restoring force is given by pressure gradients. For white dwarf stars, they present short periods (high frequencies) which increase with k and ℓ.

On the other hand, g-modes are related to the Brunt-Väisälä frequency, given by:

$$N^2 = g \left(\frac{1}{\Gamma_1} \frac{\mathrm{d} \ln P}{\mathrm{d}r} - \frac{\mathrm{d} \ln \rho}{\mathrm{d}r} \right) \quad . \tag{1.13}$$

The Brunt-Väisälä frequency represents the oscillation frequency of a gaseous bubble around its equilibrium position due to gravity. The g-modes show transverse motion (horizontal displacement) and propagate, in general, in the inner regions around the nucleus. This class of mode presents longer periods (lower frequencies) which decrease with increasing k and ℓ. For white dwarf stars, the Brunt-Väisälä frequency has lower values in the center of the star, due to electron degeneracy, which causes the g-modes to propagate at more external regions with increasing degeneracy. Finally, for each value of $\ell > 1$ there is a unique mode whose frequency falls between the g- and p-modes. This unique mode is called *f-mode* or *Kelvin* mode.

1.2.4 Local Analysis

The local treatment helps to understand the qualitative features of non-Radial oscillations. Together with the *Cowling Approximation*, which neglects the Eulerian perturbations of the gravitational potential ($\Phi' = 1$), the Local Analysis allows us to assume the coefficients of the pulsation equations as constants. In this approximation, we obtain a radial dependence proportional to $\exp(ik_r R)$ where k_r is the radial component of the wave-number. As a result, we obtain a dispersion relation given by

$$k_r^2 = \frac{1}{\sigma^2 c_S^2} \left(\sigma^2 - L_\ell^2 \right) \left(\sigma^2 - N^2 \right) \quad , \tag{1.14}$$

which relates the wave number to the frequency. For a given mode to propagate, locally it must fulfil the condition that $k_r^2 > 0$, which can be achieved by

$$k_r^2 > 0 \quad \text{if} \quad \begin{cases} \sigma^2 > L_\ell^2, N^2 \\ \sigma^2 < L_\ell^2, N^2 \end{cases} . \tag{1.15}$$

In such cases, waves can propagate in the radial direction. If the condition is not met and $k_r^2 < 0$, the radial wave number is purely imaginary and the solutions are evanescent in this region. Therefore, the inner regions of the star can be divided into propagating and evanescent regions which are determined by the shape of Lamb and Brunt-Väisälä frequencies.

1.2.5 Asymptotic approximation

To obtain the spectrum of normal modes of oscillations for a given stellar model, it is necessary to solve numerically the set of non-Radial oscillation equations. However, one can apply the *Asymptotic approximation* for modes with large radial order ($k \gg 1$) and small values of ℓ to obtain an asymptotic solution (Tassoul; Tassoul, 1968; Tassoul, 1980).

For pressure modes, the frequency at the asymptotic limit is given by

$$\sigma_{k,\ell} \approx \frac{\pi}{2}\left(2k + \ell + n + \frac{1}{2}\right)\left[\int_0^{R_*} \frac{1}{c_S(r)}\right]^{-1} , \tag{1.16}$$

where n is the polytropic index. From the above expression, we can calculate the asymptotic frequency spacing for a fixed ℓ:

$$\Delta\sigma^a = \sigma_{k+1,\ell} - \sigma_{k,\ell} = \pi\left[\int_0^R {}_* \frac{1}{c_S(r)}\right]^{-1} , \tag{1.17}$$

note that $\Delta\sigma^a$ is a constant which depends exclusively on the local adiabatic sound speed, which in turn is proportional to the Lamb frequency for a given ℓ.

For gravity modes, one must take into account the type of energy transport, if either convective ($N^2 < 0$) or radiative ($N^2 > 0$) in a given region. If the stellar model has both types of energy transport, the period spectrum of the gravity modes can be divided into g$^+$- (convective, $\sigma^2 < 0$) and g$^-$-modes (radiative, $\sigma^2 > 0$), characterised by real and imaginary eigenvalues, respectively. For a chemically homogeneous stellar model which a pure radiative (or convective) transport, the oscillation frequencies of the g-modes in the asymptotic limit can be approximated to

$$\sigma_{k,\ell}^{-1} \approx \frac{\pi}{2}\left(2k + \ell + n\frac{1}{2}\right)\frac{1}{\sqrt{\ell(\ell+1)}}\left[\int_0^{R_*} \frac{N(r)}{r} \mathrm{d}\right]^{-1} . \tag{1.18}$$

We can calculate the asymptotic frequency spacing. However, for gravity modes it is more convenient to transform angular frequency into period by using the relation $\Pi_{k,\ell} = 2\Pi/\sigma_{k,\ell}$.

Therefore, we can define the asymptotic period spacing as

$$\Delta\Pi_\ell^a = \Pi_{k+1,\ell} - \Pi_{k,\ell} = \frac{2\Pi^2}{\sqrt{\ell(\ell+1)}}\left[\int_0^{R_*}\frac{N(r)}{r}\mathrm{d}r\right]^{-1} \quad , \tag{1.19}$$

where $\Delta\Pi_\ell^a$ is a constant which is proportional to the Brunt-Väisälä frequency.

1.2.6 The effects of Rotation and Magnetic Fields

The equilibrium structure of a stellar model is no longer spherically symmetric in the presence of rotation or/a magnetic field. In the case of slow rotation, where any angular frequency Ω is much smaller than the oscillation frequency of any normal mode, we can make a first-order correction in the oscillation frequency

$$\sigma_{k,\ell,m}(\Omega) = \sigma_{k,\ell}(\Omega = 0) + \delta\sigma_{k,\ell,m} \quad , \tag{1.20}$$

where the first-order correction depends on the azimuth number m. In the case of uniform rotation $\Omega = \text{const.}$ (or rigid body rotation), the correction in the eigenfrequency is given by (Cowling; Newing, 1949; Ledoux, 1951):

$$\delta\sigma_{k,\ell,m} = -m\Omega(1 - C_{k,\ell}) \quad , \tag{1.21}$$

where

$$C_{k,\ell} = \frac{\int_0^{R_*}\rho r^2[2\xi_r\xi_h + \xi_h^2]\mathrm{d}r}{\int_0^{R_*}\rho r^2[\xi_r^2 + \ell(\ell+1)\xi_h^2]\mathrm{d}r} \quad , \tag{1.22}$$

is a constant called the rotational splitting coefficient. It depends on the model and the mode considered. The terms ξ_r and ξ_h are the radial and horizontal displacements, respectively. In the asymptotic limit for p-modes, the radial displacement is much larger than the horizontal one ($\xi_r \gg \xi_r$) so that $C_{k,\ell} \to 0$ for increasing k. On the other hand, for g-modes we have that $\xi_r \ll \xi_r$ and $C_{k,\ell} \to 1/[\ell(\ell+1)]$ for increasing k in the asymptotic limit.

Let us now consider an angular rotational velocity which is a function of the stellar radius ($\Omega(r)$), the first-order correction in the frequency is given by

$$\delta\sigma_{k,\ell,m} = -m\int_0^{R_*}\Omega(r)K_{k,\ell}(r)\mathrm{d}r \quad , \tag{1.23}$$

where $K_{k,\ell}(r)$ is the rotational kernel which is written in terms of the displacement:

$$K_{k,\ell}(r) = \frac{\rho r^2\xi_r^2 - 2\xi_r\xi_h - \xi_h^2[1 - \ell(\ell+1)]}{\int_0^{R_*}\rho r^2[\xi_r^2 + \ell(\ell+1)\xi_h^2]\mathrm{d}r} \quad . \tag{1.24}$$

The rotational kernel acts over $\Omega(r)$ as a weight function.

In the presence of a weak magnetic field, the pulsation frequencies experience small changes in the form of:

$$\sigma_{k,\ell,m}(\vec{B}_0) = \sigma_{k,\ell}(\vec{B}_0 = 0) + \sigma'_{k,\ell,m} \quad , \tag{1.25}$$

where $\sigma_{k,\ell}(\vec{B}_0 = 0)$ is the oscillation frequency without magnetic field and $\sigma'_{k,\ell,m}$ is the first order correction. The expression for $\sigma'_{k,\ell,m}$ is dependent of the eigenfunction ξ, in the case without magnetic field, and dependent on $\vec{B}_0$ (Jones et al., 1989):

$$\sigma'_{k,\ell,m} = \frac{1}{8\pi\sigma_{k,\ell}(\vec{B}_0 = 0)} \frac{\int_o^M \rho^{-1}|\vec{B}'|^2 \mathrm{d}m_r - \int_S [(\xi^* \times \vec{B}_0) \times \vec{B}'] \cdot \hat{n} \mathrm{d}s}{\int_M |\xi|^2 \mathrm{d}m_r} \quad . \tag{1.26}$$

The subscript S means that the integral is calculated over the star surface, the $\hat{n}$ is the normal vector to such surface, and $\vec{B}'$ is given by:

$$\vec{B}'(r) = \nabla \times (\xi \times \vec{B}_0) \quad . \tag{1.27}$$

For a constant or dipolar magnetic field, the frequency correction $\sigma'_{k,\ell,m}$ depends on $|\vec{B}_0|$ and the azimuth number as m^2. This implies that the frequency $\sigma_{k,\ell}$ is divided into $\ell + 1$ components as opposed to $2\ell + 1$ as in the case of slow rotation, where the degeneration in m is partially removed.

1.2.7 Excitation Mechanisms

In general, we can compare a star to a heat engine, where the external layers regulate the outward energy flux, usually through ionization and recombination of ions corresponding to the dominant chemical species. A perturbation in the energy flux results in a mechanism that converts thermal to mechanical energy. In the case of white dwarfs and low mass stars, the most common mechanism are the $\kappa - \gamma$ and the ϵ mechanisms.

1.2.7.1 The $\kappa - \gamma$ mechanism

The dominant effect that drives pulsations in white dwarfs and pre-white dwarfs stars is the $\kappa - \gamma$ mechanism. Generally, when there is an increase in the outward energy flux, this increases the temperature and decreases the opacity, allowing the radiation to leave the star easily. However, in a partially ionized region, the increase in the radiative flux can be absorbed which increases the number of ions, instead of increasing the temperature. As a result, the increase in ions blocks the outward flux, which is stocked as ionizing energy. This process is known as the γ mechanism. Also, the huge opacity gradients which are formed due to the partially ionized regions can excite pulsations by means of the κ mechanism (Dolez; Vauclair, 1981). For white dwarfs in general, those two mechanisms act together. In summary, a full pulsation cycle caused by the $\kappa - \gamma$ mechanism can be described as follows:

1. In the star compression, the outward radiative flux is blocked by the increase in opacity. The radiative energy is stored in ions as kinetic energy . The increase in temperature is small.

2. At the point of maximum compression, the partially ionized region keeps increasing its temperature, which causes a decrease in density.

3. The star expands due to the release of the ionizing energy. The opacity decreases along the expansion which facilitates the release of energy. This is the point of minimum density, which results in the expansion of matter and a decrease in temperature.

4. At the point of maximum expansion, the matter keeps losing heat until reaching a minimum value of pressure. All stored energy is released by the ions, which makes a partially ionized region and restarts the pulsation cycle.

1.2.7.2 The ϵ mechanism

The ϵ mechanism acts on the regions where nuclear reactions take place. In the star compression, the inner temperature increases which translate to an increase in nuclear energy generation. As nuclear reactions depend strongly on the temperature, small changes in temperature result in huge increases in nuclear energy production. The process is fed back, as the increase in energy production also increases the temperature, resulting in a global instability that grows over time. However, this mechanism is not very efficient since pulsation amplitudes tend to be small in layers with higher temperatures and higher energy rates (Battich et al., 2018).

1.3 Asteroseismology

Asteroseismology is the study of the internal structure and evolutionary properties of stars from their observed variance in brightness. An asteroseismological fit compares the observed periods to theoretical periods obtained from a computational model of the given star. Except for neutrino emission, asteroseismology is the only technique that can give direct information about stellar interiors.

Over the years, collaborations and surveys were made and built to supply the demand for observations. One of the earliest campaigns was the *Whole Earth Telescope* (WET) founded in 1986 (Nather et al., 1990). The WET is a worldwide network of 25 astronomical observatories, with a common objective to observe quasi-continuous white dwarf light-curves. Other telescopes helped to increase the number of observed variable stars, such as *The Optical Gravitational Lensing Experiment* (OGLE) (Udalski et al., 1992) and the *Sloan Digital Sky Survey* (SDSS) (York et al., 2000). Also, the space telescopes, which allow to obtain light-curves without gaps from the day/night cycle,

Table 1 – Properties of the families of pulsating white dwarfs, sorted by increasing effective temperature. Adapted from Córsico et al. (2019).

Type	Range of periods [s]	Teff [kK]	$\log g$ [cgs]	Quantity
ELMV	100 - 6200	7.8 - 10	6 - 6.8	11
pre-ELMV	300 - 5000	8-13	4 - 5	5
DAV (ZZ Ceti)	100 - 1400	10.4-12.4	7.5-9.1	250
GW Lib	100 - 1900	10.5-16	8.35-8.7	20
DQV	240 - 1100	19-22	8-9	6
DBV (V777 Her)	120 - 1080	22.4-32	7.5-8.3	39
Hot DAV	160 -705	30-32.6	7.3-7.8	3
GW Vir	300 - 6000	80-180	5.5-7.7	19

are an improvement in the quality and amount of data gathered. The first telescope to collect large-scale astrometric and photometric data was the *HIPPARCOS* (HIgh Precision PARallax COlleting Satellite) (Perryman et al., 1997). Later there was *CoRoT* (Convection, Rotation and Planetary Transits) launched in 2006 for seismology and planet-hunting (Auvergne et al., 2009), followed by the *Kepler* space mission in 2009 (Borucki et al., 2010). Recent missions are *Gaia* (Gaia Collaboration et al., 2017) and *TESS* (Ricker et al., 2015) satellites.

Pulsating stars can be found in many evolutionary phases and in a large range of masses. However, this work will focus on pulsating low mass white dwarfs and the discussion will shift to the white dwarf class of pulsating objects. For general information about pulsating stars, the reader is referred to the book of Aerts, Christensen-Dalsgaard & Kurtz (2010) and Catelan & Smith (2015).

1.3.1 Pulsating White dwarfs

Asteroseismology is a powerful tool to explore the internal structure and evolutionary properties of white dwarf stars. It allows us to measure the mass of the hydrogen and helium layers (Castanheira; Kepler, 2009; Romero et al., 2012; Romero et al., 2013), to better estimate the total stellar mass and to determine the core composition (Córsico; Althaus, 2006; Calcaferro; Córsico; Althaus, 2016; Romero et al., 2017). It also allows to study axions (Isern; Hernanz; Garcia-Berro, 1992; Bischoff-Kim; Montgomery; Winget, 2008; Isern et al., 2010; Córsico et al., 2012) and neutrino emission (Winget et al., 2004), crystallisation (Montgomery; Winget, 1999; Kanaan et al., 2005) and external convective zones (Montgomery, 2005). For a full review on the applications and pulsations properties of white dwarfs, the reader is referred to the works of Winget & Kepler (2008), Fontaine & Brassard (2008), Althaus et al. (2010b).

The first variable pulsating white dwarf, *HL Tau 76*, was discovered by Arlo Landolt in 1968 when he detected a period of ≈ 740 s(Landolt, 1968). This period was too large to be explained by the current theory of radial pulsations. Later, more pulsating white dwarfs were detected. This new type of variable stars was called *ZZ Ceti*. McGraw (1977) showed that the luminosity variations were due to changes in the superficial temperatures of the stars, confirming the idea of non-radial pulsations as the cause of those variations. Robinson, Kepler & Nather (1982) developed the theoretical basis of that hypotheses. The ZZ Ceti (also called DAV) are the most numerous class and presents hydrogen-rich atmosphere and effective temperatures of $10\,400$ K $\leq T_{\rm eff} \leq 12\,400$ K. They present periods of $100 - 1\,400$ s with low harmonic degree ($\ell \leq 2$) and short to intermediate radial order. The excitation mechanism is the $\kappa - \gamma$ due to the opacity peak in the partial ionization zone of hydrogen.

Other types of pulsating white dwarfs were discovered along the cooling sequence. In Table 1 we show the properties of the many families of pulsating white dwarfs. The first class of pulsating hydrogen-deficient white dwarf discovered was the PG 1159 (or GW Vir) stars (McGraw et al., 1979). This is the hottest known class of pulsating pre-white dwarf stars ($80\,000$ K $\leq T_{\rm eff} \leq 180\,000$ k) presenting an atmosphere rich with carbon ($\approx 15 - 60\%$), oxygen ($\approx 2 - 20\%$) and helium ($\approx 30 - 85\%$) (Werner; Herwig, 2006). They are multi-periodic variables with low harmonic degree ($\ell \leq 2$) and higher radial order ($k \geq 18$), with periods of $300 - 6000$ s. The κ excitation mechanism is responsible for driving pulsations due to the partial ionization of carbon and oxygen in the outer layers. This class is composed of two sub-classes, the *PNNV* (Planetary Nebula Nuclei Variable) and *DOV*, the former is surrounded by its planetary nebula while the former is not.

The DBV class (or V777 Her) was first predicted by Winget et al. (1982) and detected a few months later by Winget et al. (1982). The DBV class presents an almost pure helium atmosphere and effective temperatures of $22\,400$ K $\leq T_{\rm eff} \leq 32\,000$ K. They present non-radial g-modes with periods of $120 - 1\,080$ s, excited by the $\kappa - \gamma$ mechanism due to the partial ionization of helium in the base of the convective zone.

The GW Lib class was first observed by Warner & van Zyl (1998) being a class of accreting pulsating white dwarfs in cataclysmic variables. They present effective temperatures of $10\,500$ K $\leq T_{\rm eff} \leq 16\,000$ K and hydrogen-rich atmosphere. However, they can also present a helium-rich atmosphere due to accretion. They have non-radial g-modes, with periods of $100 - 1\,900$ s. The g-modes are excited due to the H/He ionization zone.

The Hot DAV class was predicted by Shibahashi (2005), observed by Kurtz et al. (2008) and recently confirmed as a variable class by Romero et al. (2020). The DQV (or Hot DQ) variable class are white dwarfs with carbon- and helium-rich atmospheres and were discovered by Montgomery et al. (2008). They show non-radial g-mode periods between $240 - 1\,100$ s and effective temperatures of $19\,000$ K $\leq T_{\rm eff} \leq 22\,000$ K. The modes are excited due to the opacity peak of the partial ionization of carbon.

Finally, the ELMV (Extremely Low-Mass white dwarf Variables) class, with hydrogen atmospheres, were discovered by Hermes et al. (2012) , and the pre-ELMV which are probably the precursors of ELMV were discovered by Maxted et al. (2013). The pre-ELMV shows multi-periodic pulsations in a period range of $300 - 5000$ s. They present a surface composition made of a mixture of hydrogen and helium, and their pulsation modes are high-frequency p-modes and intermediate-frequency p-g modes, which are modes that behave like g-modes in the inner parts of the star and like p-modes in the outer layers. This is due to the peculiar shape of the Brunt-Väisälä frequency (Córsico et al., 2016). These modes are excited by the $\kappa - \gamma$ mechanism. The ELMV class will be discussed in the following section.

Figure 7 shows the classes of pulsating white dwarf stars in a Kiel diagram. The different symbols indicate the element related to the excitation mechanism: hydrogen (circles), helium (triangle-up), carbon and/or oxygen (triangle-left), and iron peak elements (squares). The known variable low-mass white dwarfs are indicated with a light-blue dot. The position of J115219.99+024814.4, the star that is the subject of this work, is depicted with a grey star, with the atmospheric parameters taken from Parsons et al. (2020). The data was extracted from Fontaine & Brassard (2008), Bognar & Sodor (2016), Pietrukowicz et al. (2017), Córsico et al. (2019), Romero et al. (2019), Kupfer et al. (2019). The dashed lines are theoretical white dwarf sequences with helium-core and mass of 0.324 and 0.182 $M_\odot$ (Istrate et al., 2016), and C/O core with masses of 0.878, 0.638 and 0.524 $M_\odot$ (Romero; Campos; Kepler, 2015). Figure 7 also shows the *BLAPS* (Blue Large-Amplitude Pulsators) class discovered by (Pietrukowicz et al., 2017) and the high-gravity BLAPS, discovered by Kupfer et al. (2019). The BLAPS class presents just the radial fundamental mode ($\ell = 0, k = 0$), periods in range of $1\,200 - 2\,400$ s, high metallicity and mean effective temperature of $T_{\rm eff} \approx 30\,000$. It is believed that BLAPS are pre-low mass white dwarf stars with hot helium-core and hydrogen shell burning that drives pulsations due to the κ mechanism acting in the opacity bump due to iron peak elements (Romero et al., 2018). The high-gravity BLAPS are less-massive analogs of the BLAPS class. The nature of pulsations in these classes is still under debate.

1.3.2 The LM and ELMV Class

The LM white dwarfs can harbour a helium core or a hybrid core, composed of helium, carbon, and oxygen. The core composition will depend on the formation channel. For high metallicity progenitors, the LM white dwarfs can be the result of enhanced mass loss, due to high opacity, before the occurrence of the helium-flash during during the RGB phase, which avoids the helium ignition and leads to a low mass remnant with a helium core. However, for solar metallicity progenitors, mass-loss episodes must occur in interacting binary system through mass-transfer (Istrate et al., 2016). Depending on the stellar mass and the orbital period of the binary system, a low mass remnant with helium-

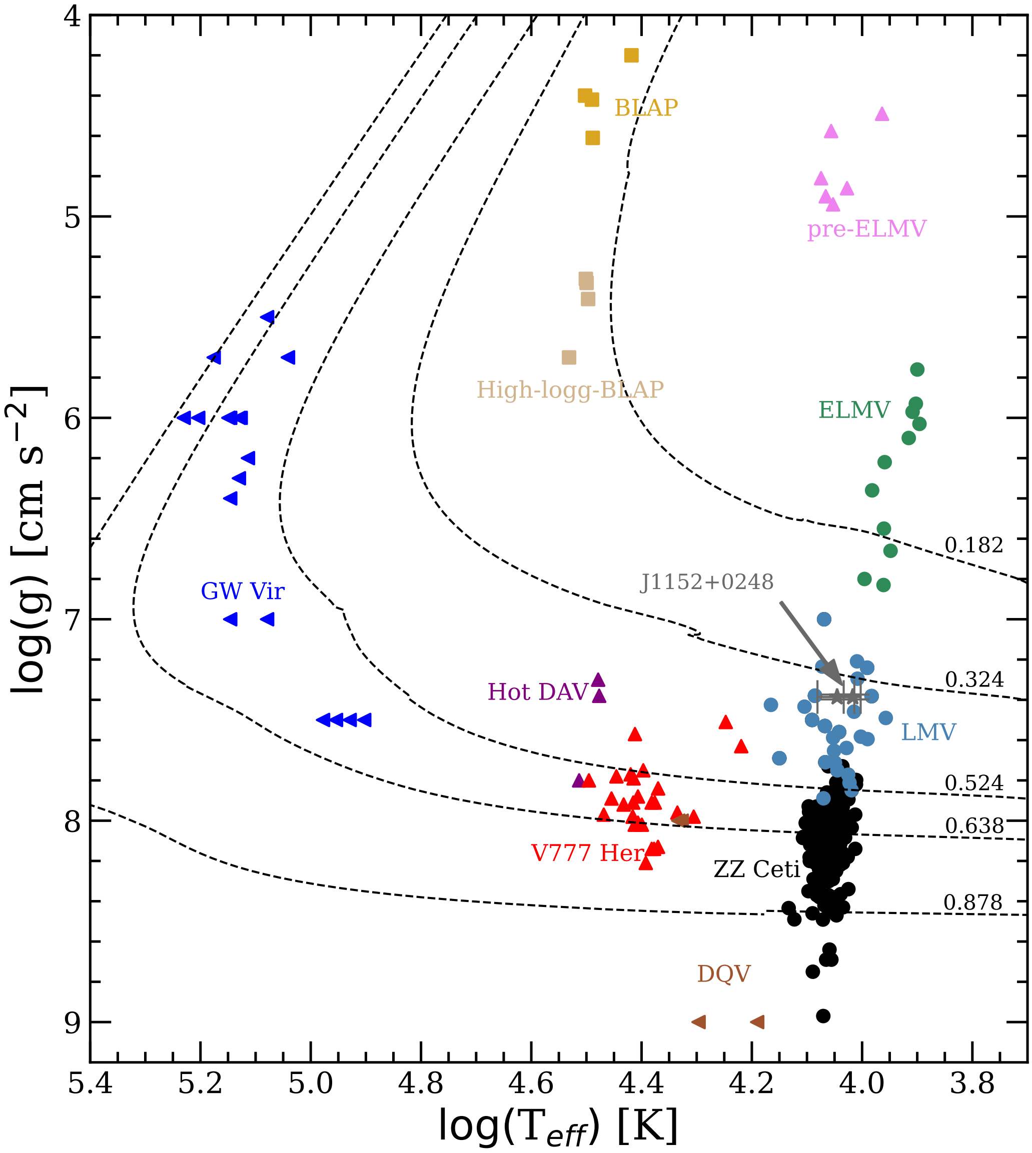

Figure 7 – The classes of pulsating white dwarf stars. The different symbols indicate the element related to the excitation mechanism: hydrogen (circles), helium (triangle-up), carbon and/or oxygen (triangle-left), and iron peak elements (squares). Adapted from Romero et al. (2021). See text for details.

or hybrid-core can be formed (Panei et al., 2007; Istrate et al., 2014; Zenati; Toonen; Perets, 2019). In the case of the ELM white dwarfs, strong mass-loss in close binary system is necessary to explain their formation, since MS lifetimes would be larger than the age of the Universe for single star evolution (Kilic; Stanek; Pinsonneault, 2007; Pelisoli; Vos, 2019).

The existence of pulsations in ELM white dwarfs was predicted by Steinfadt, Bildsten & Arras (2010) and later discovered by Hermes et al. (2012). The first pulsating ELM white dwarf, SDSS J1840+6423, is a 4.6 hour binary system with another white dwarf. It shows high-amplitude and multi-periodic g-modes with periods in range 2 000 − 4 900 s and effective temperature of $T_{\rm eff} = 9100$ K. (Córsico et al., 2019). Recently, more ELM variables were discovered (Hermes et al., 2013; Kilic et al., 2015; Bell et al., 2015; Bell et al., 2017; Bell et al., 2018; Kilic et al., 2018; Pelisoli et al., 2019). In addition, there are 22 objects in the literature with stellar masses within the range $0.30 \leq \mathrm{M}/\mathrm{M}_{\odot} \leq 0.45$ (light blue dots in Fig. 7) that show photometric variability with periods between 200 and 1300 s (Bognar; Sodor, 2016; Su et al., 2017; Fuchs, 2017; Rowan et al., 2019). For 4 of them, the uncertainties in the atmospheric parameters are quite large, leading to uncertainty in the stellar mass of 0.1–0.4 $\mathrm{M}_{\odot}$ (Su et al., 2017; Rowan et al., 2019). The low number of pulsating low-mass WDs as compared to canonical mass ZZ Ceti stars could be due to some kind of fine-tuning during the evolution of the progenitor, but it is most likely due to the lack of studies focused on the search for pulsations on objects in this stellar mass range.

The increasing number of discovered ELMV motivated theoretical work to explore the pulsational properties of these stars. The works of Steinfadt, Bildsten & Arras (2010) and Córsico et al. (2012), Córsico et al. (2012) concluded that, in opposite to what happens to ZZ Ceti and LM variable white dwarfs, the g-modes in ELM variables mainly probe the core regions while p-modes sound the stellar envelope. This happens because the Brunt-Väisälä frequency has large values in the core, which allows the eigenfunctions of g-modes to penetrate the deep regions of the star. In LM white dwarfs, the g-modes are sensitive to the helium/hydrogen chemical transition, which permit to constrain the hydrogen envelope thickness (Córsico; Althaus, 2014). Also, the works of Córsico et al. (2012), Van Grootel et al. (2013), Córsico & Althaus (2016) shows that the $\kappa - \gamma$ mechanism and the convective driving, both acting at the hydrogen partial ionization region are responsible for the excitation of pulsations. Therefore, asteroseismology of ELMVs allows to put constraints to both the core and envelope chemical structure.

1.3.3 Asteroseismological tools

The Forward Period Spacing (FPS), $\Delta\Pi_{k,\ell} = \Pi_{k+1,\ell} - \Pi_{k,\ell}$, can be used to determine some of the structural parameter in pulsating white dwarf stars. The FPS depends on the Brunt-Väisälä frequency in the same way as the asymptotic period spacing $\Delta\Pi_{\ell}^{a}$ (see equation (1.19)), and in turn the Brunt-Väisälä frequency is proportional to the surface gravity $N \propto g$, where $g \propto \mathrm{M}/\mathrm{R}^2$. Hence, the period spacing is proportional to the stellar mass and inversely proportional to the stellar radius. For a chemically homogeneous and radiative star, the period spectrum is characterized by a constant period separation, known as the asymptotic period spacing (Tassoul; Fontaine; Winget, 1990). In this case, the forward period spacing would be constant and given by the asymptotic period spacing. However, the inner chemical structure of white dwarfs is not homogeneous, showing composition gradients (Althaus et al., 2010a). In this case, the asymptotic period spacing corresponds to the period spacing at the limit of very large values of k, where it is almost constant (Tassoul; Fontaine; Winget, 1990). Examples of the applications of this technique can be found in the works of Winget et al. (1991), Kawaler et al. (1995), Handler et al. (2003), Calcaferro, Córsico & Althaus (2016), Romero et al. (2017).

Another technique is the asteroseismological fit of periods. This technique searches for a theoretical stellar model that best matches the observed periods. To find the best fit model, we calculate the quality function, defined as:

$$\chi^2 = \sum_{i=1}^{n} \left(\frac{\Pi_{\text{obs}}^{(i)} - \Pi_{\text{th}}^{(i)}}{\sigma_{\text{obs}}^{(i)}} \right)^2 \quad , \tag{1.28}$$

where $\Pi_{\text{obs}}^{(i)}$ and $\sigma_{\text{obs}}^{(i)}$ are the observed periods and their associated uncertainties, $\Pi_{\text{th}}^{(i)}$ are the theoretical periods, and n is the number of observed modes. A search for a minimum of the equation 1.28 gives us the model that best fits the observed periods. If there is a global minimum in the quality function, only one asteroseismological solution exists. Usually there are several local minima, which make it necessary to apply additional restrictions to the model. A common restriction is the observed effective temperature and its associated error. This technique allows to estimate some quantities as stellar mass, luminosity, radius, etc., from the best fitting model. Examples of the applications of this technique can be found in the works of Castanheira & Kepler (2008), Romero et al. (2013), Romero, Campos & Kepler (2015), Romero et al. (2017), Hall, Castanheira & Bischoff-Kim (2023).

1.4 Objectives

The recent interest in LM and ELM white dwarfs, leveraged by the observation of pulsation, has increased the total number of pulsating stars and the number of theoretical models computed to explain its formation and nature of pulsations. Observations and theoretical models are the basic ingredients for an asteroseismological study.

In the first part of this work, we present a list of variable LM white dwarfs and their mean periods, to draw a parallel with the pulsational properties of ZZ Ceti stars. Also, a list of candidates for LMVs is shown together with a discussion about observations of a sample of those candidates, in an attempt to increase the number of discovered LMVs.

Recently, Parsons et al. (2020) reported the discovery of the first pulsating LM white dwarf in a compact eclipsing binary system, with another LM white dwarf as a companion. The binary nature of the SDSS J115219.99+024814.4 system (hereafter

J1152+0248) was first reported by Hallakoun et al. (2016), based on the K2 data of the *Kepler* mission. Based on the determination of the radius, the authors proposed that the variable component (hereafter J1152+0248−V) is either a hybrid-core or a helium-core LM white dwarf with an extremely thin surface hydrogen layer ($M_H/M_\odot < 10^{-8}$). However, different inner chemical structures will influence the period spectrum of a pulsating star. Consequently, an asteroseismological study of this object can help to elucidate both the chemical composition and the mass of the hydrogen envelope.

In the last part of this work, we explore the pulsational properties of both hybrid- and helium-core LM white dwarf models representative for the case of J1152+0248−V. Furthermore, we consider sequences with hydrogen envelopes thinner than the value predicted by stable mass-transfer binary evolutionary models. As different inner chemical structures will influence the period spectrum of a pulsating star, this work intends to perform an asteroseismological study to elucidate both the chemical composition and the mass of the hydrogen envelope of the pulsating component of J1152+0248.

2 Numerical Methods

In this chapter, it is presented a description of the numerical code used to compute the evolutionary sequences and the pulsations in this thesis. First, the evolutionary code MESA will be described followed by a discussion of the input physics applied to the code. Finally, a description of the stellar Oscillation code `GYRE` and its inputs will be discussed.

2.1 Evolutionary Code

The numerical simulations presented in this thesis were performed using the *Modules for Experiments in Stellar Astrophysics* - MESA code (Paxton et al., 2011; Paxton et al., 2013; Paxton et al., 2015; Paxton et al., 2018), a suite of open source, robust, efficient, thread-safe libraries for a wide range of applications in computational stellar astrophysics. It is a one-dimensional stellar evolution module that combines many of the numerical and physics modules for simulations of a wide range of stellar evolution scenarios, ranging from very low mass to massive stars, including advanced evolutionary phases. The code solves the fully coupled structure and composition equations simultaneously, using adaptive mesh refinement and time-step controls. It provides equation of state, opacity, nuclear reaction rates, element diffusion data, and atmospheric boundary conditions. Each module is constructed as a separate `Fortran 95` library with its own explicitly defined public interface to facilitate independent development.

The MESA evolutionary code has been extensively used to perform calculations of LM and ELM white dwarfs (Istrate et al., 2016; Istrate; Fontaine; Heuser, 2017; Sun; Arras, 2017), hybrid C/O/Ne white dwarfs and Type Ia SN progenitors (Jones et al., 2013; Denissenkov et al., 2013; Chen et al., 2014; Farmer; Fields; Timmes, 2015; Brooks et al., 2017b; Lauffer; Romero; Kepler, 2018), accreting white dwarf binaries with C/O core (Brooks et al., 2016; Wang; Podsiadlowski; Han, 2017) and O/Ne core (Schwab; Bildsten; Quataert, 2017; Brooks et al., 2017a), white dwarf isochrones (Dotter, 2016) and set of sequences covering the white dwarf mass range (Choi et al., 2016; Pignatari et al., 2016; Ritter et al., 2017).

The MESA code is a Henyey style code (Henyey et al., 1959) with automatic mesh refinement, analytic Jacobians, and coupled solution of the structure and composition equations. The code builds one-dimensional, spherically symmetric models by dividing the structure into cells. For a cell k, the cell mass-averaged variables are density ρ_k, temperature T_k, and mass fraction vector $X_{i,k}$. The boundary variables are mass interior to the face (boundary) m_k, radius r_k, luminosity L_k, and velocity v_k. In addition to these basic variables, composite variables are calculated for every cell and face, such as nuclear energy ε_{nuc}, opacity κ, Lagrangian diffusion coefficient σ_k, and mass flow rate F_k. All variables are evaluated at time $t + \delta t$. Figure 8 shows a scheme of cell and face variables. The code solves the mass conservation equation, hydrostatic equilibrium, energy transport, and energy conservation in the following form:

$$\ln r_k = \frac{1}{3} \ln \left[r_{k+1}^3 + \frac{3}{4\pi} \frac{\mathrm{d}m_k}{\rho_k} \right] \tag{2.1}$$

$$P_{k-1} - P_k = \overline{\mathrm{d}m_k} \left[-\frac{Gm_k}{4\pi r_k^4} - \frac{a_k}{4\pi r_k^2} \right] \tag{2.2}$$

$$T_{k-1} - T_k = \overline{\mathrm{d}m_k} \left[\nabla_{T,k} \left(\frac{\mathrm{d}P}{\mathrm{d}m} \right)_{\text{hydrostatic}} \frac{\overline{T_k}}{\overline{P_k}} \right] \tag{2.3}$$

$$L_k - L_{k+1} = \mathrm{d}m_k \left(\varepsilon_{nuc} - \varepsilon_{v,\text{thermal}} + \varepsilon_{\text{grav}} \right) \tag{2.4}$$

where P_k is pressure at cell k, $\overline{\mathrm{d}m_k} = 0.5(\mathrm{d}m_{k-1} + \mathrm{d}m_k$, a_k is the Lagrangian acceleration at face k, $\nabla_{T,k} = \mathrm{d}\ln T/\mathrm{d}\ln P$ at face k, $\overline{T_k}$ and $\overline{P_k}$ are the mass averaged values of temperature and pressure between cell k and $k-1$, $\varepsilon_{v,\text{thermal}}$ is the specific thermal neutrino-loss rate and $\varepsilon_{\text{grav}}$ is the specific rate of change of gravitational energy. This formulation was chosen to enhance numerical stability.

The chemical composition is calculated considering both the nuclear reaction ($\mathrm{d}X_{\text{burn}}$) and the mixing ($\mathrm{d}X_{\text{mix}}$) caused by convection. The equation for mass fraction $X_{i,k}$ for species i in cell k is given by:

$$X_{i,k}(t+\delta t) - X_{i,k}(t) = \mathrm{d}X_{\text{burn}} + \mathrm{d}X_{\text{mix}} \tag{2.5}$$

$$= \frac{\mathrm{d}X_{i,k}}{\mathrm{d}t} \delta t + (F_{i,k+1} - F_{i,k}) \frac{\delta t}{\mathrm{d}m_k} \tag{2.6}$$

where $\mathrm{d}X_{i,k}/\mathrm{d}t$ is the rate of change from nuclear reactions and $F_{i,k}$ is the mass of species i flowing across face k:

$$F_{i,k} = (X_{i,k} - X_{i,k-1}) \frac{\sigma_k}{\overline{\mathrm{d}m_k}} \tag{2.7}$$

The code does not require the structure equations to be solved separately from the composition equations. It simultaneously solves the full set of coupled equations for all cells from the surface to the center by using a Newton-Raphson solver.

The evolutionary sequences in this work were computed using MESA version `r12115` and are part of a grid of models covering the mass interval where helium- and hybrid-core white dwarfs overlap, i.e. $\sim$0.32–0.45 $\mathrm{M}_\odot$ (Istrate; et. al., in preparation).

2.1.1 Input Physics

In this section, we describe the physical aspects and numerical choices made for the computations of all evolutionary sequences in this dissertation.

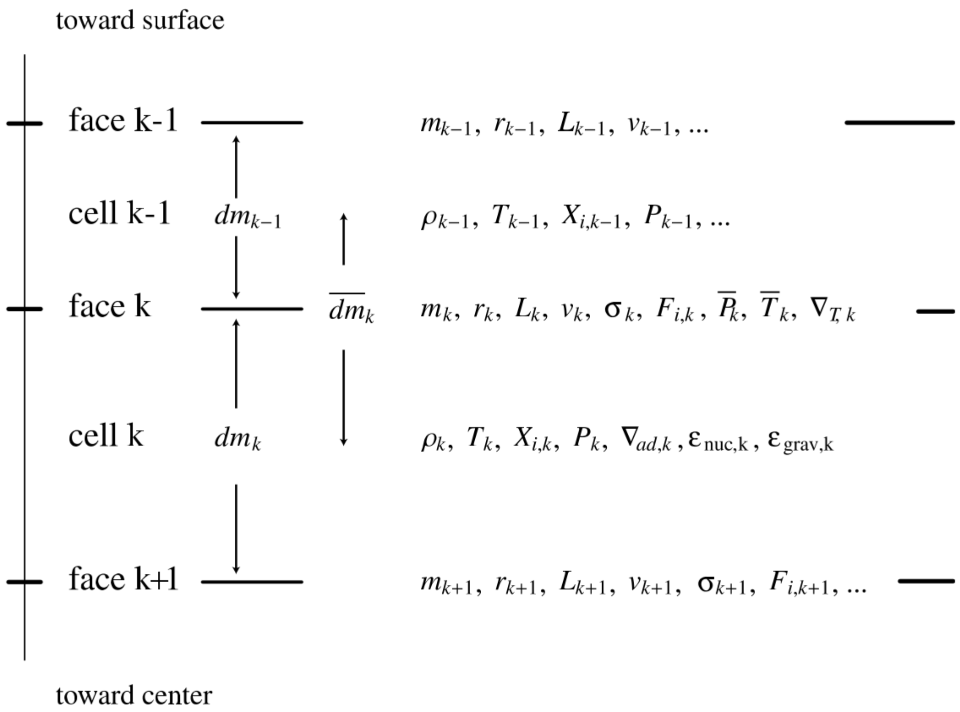

Figure 8 – A scheme of how MESA computes its cell and face (boundary) variables. Adapted from Paxton et al. (2011).

We consider an initial metallicity of $Z = 0.01$, with a helium abundance given by $Y = 0.24 + 2.0 \cdot Z$ and the metal abundances scaled according to Grevesse & Sauval (1998). Convection is modeled using the standard mixing-length theory (Henyey; Vardya; Bodenheimer, 1965) with a mixing-length parameter $\alpha = 2.0$, adopting the Ledoux criterion. A step function overshooting extends the mixing region for 0.25 pressure scale heights beyond the convective boundary during core hydrogen burning. In order to smooth the boundaries, we also include exponential overshooting with $f = 0.0005$. Semiconvection follows the work of Langer, Fricke & Sugimoto (1983), with an efficiency parameter α_{sc} = 0.001. Thermohaline mixing is included with an efficiency parameter of 1.0. Radiative opacities are taken from Ferguson et al. (2005) for $2.7 \leq \log \mathrm{T} \leq 3.8$ and OPAL (Iglesias; Rogers, 1993; Iglesias; Rogers, 1996) for $3.75 \leq \log \mathrm{T} \leq 8.7$, and conductive opacities are adopted from Cassisi et al. (2007).

The nuclear network used is `cno_extras.net` which accounts for additional nuclear reactions for the CNO burning compared to the default `basic.net` network. We consider the effects of element diffusion (Iben I.; Tutukov, 1985; Thoul; Bahcall; Loeb, 1994) on all isotopes and during all the stages of evolution.

We adopt a grey atmosphere using the Eddington approximation on the evolution before the cooling track, and the white dwarf atmosphere tables from Rohrmann et al. (2012) during the white dwarf cooling stage.

Rotational mixing and angular momentum transport are treated as diffusive processes as described in Heger, Langer & Woosley (2000), with an efficiency parameter $f_c = 1/30$ (Chaboyer; Zahn, 1992) and a sensitivity to composition gradients parametrized by $f_\mu = 0.05$. We also include transport of angular momentum due to electron viscosity (Itoh; Kohyama; Takeuchi, 1987). All models include rotation, with the initial rotational velocity initialized such that the donor is synchronized with the orbital period. We include magnetic braking for the loss of angular momentum just for the donors leading to the formation of the helium-core WDs. For more massive donors (>2.0 $M_\odot$), which are considered for the progenitors of the hybrid-core WDs, we assume that the magnetic braking stops operating. This assumption follows from the conventional thinking that braking via a magnetized stellar wind is inoperative in stars with radiative envelopes (Kawaler, 1988). For all the models, we assume a mass transfer efficiency of 50%, i.e. 50% of the transferred mass is accreted by the companion, while the rest leaves the system with the specific angular momentum of the accretor.

2.2 Stellar Oscillation Code

The numerical computations for pulsations were calculated using the `GYRE` Stellar Oscillation code (Townsend; Teitler, 2013; Townsend; Goldstein; Zweibel, 2018a; Goldstein; Townsend, 2020; Sun; Townsend; Guo, 2021), an open–source code that calculates eigenfrenquencies and eigenfunctions for an input stellar model. The `GYRE` code has been used to compute pulsations of solar like stars (Compton et al., 2018), intermediate and massive stars (Edelmann et al., 2019; Van Reeth et al., 2018; Moravveji, 2016), subdwarfs (Kupfer et al., 2019), pre-main sequence stars (Murphy et al., 2021), B type stars (Zwintz et al., 2017; Buysschaert et al., 2018; Townsend; Goldstein; Zweibel, 2018b). The code has been under constant improvements by adding features as non-adiabatic calculations (Goldstein; Townsend, 2020) and stellar tides (Sun; Townsend; Guo, 2021).

The code is written in `Fortran 2008` with a modular architecture which allows parallelized computations on multiple processor cores or cluster nodes. It implements a *Magnus Multiple Shooting* (MMS) scheme for solving the set of linearized pulsations equations given by equations (A.60) to (A.63) (Magnus, 1954; Gabriel; Noels, 1976). A Shooting Scheme is a method for solving a boundary value problem by reducing it to a set of initial value problems. The mismatch between a solution of the initial value problem and the boundary value problem is quantified by a discriminant function $D(\omega)$, which vanishes when those solutions match. The roots of $D(\omega)$ correspond to the eigenfrequencies of the boundary value problem. The MMS method divides the interval over which a solution is sought into several smaller intervals, solves an initial value problem in each of the smaller intervals, and imposes additional matching conditions to form a solution on the whole interval by using a Magnus integrator (Gabriel; Noels, 1976).

The GYRE version 5.0 code was used as a stand-alone package, in its adiabatic form. A typical GYRE run involves the following steps: First, a stellar model file is read, and a grid of frequencies is calculated. Then, a scan through frequency space searches for sign changes in the discriminant $D(\omega)$. After that, the signal changes are used as initial guesses for the discriminant roots and when the roots are found, the corresponding eigenfunctions are reconstructed.

In this work, we computed pulsations for helium- and hybrid-core sequences, performing a scan using a linear grid over a period range of $80 - 2000$ s, for $\ell = 1$ and $\ell = 2$ gravity modes, with `alpha_osc`$= 100$ and `alpha_exp` and `alpha_ctr` set to 50. The boundary conditions and variables were set to UNNO and `DZIEM`, respectively. All the configuration settings are attached in Appendix C.

3 Low Mass White Dwarf Variables

This chapter presents the observed confirmed LM white dwarf variables and an analysis of the weighted mean period of these objects. Also, a list of LMV candidates, its selection criteria, observational runs, and data analysis of light curves obtained for this thesis are discussed.

3.1 LMV White Dwarfs and Their Weighted Mean Period

In the literature, there are 22 confirmed LMV white dwarfs with stellar masses within the range of $0.30 \leq \mathrm{M/M_{\odot}} \leq 0.45$ and photometric variability with periods between 200 and 1300 s. Those objects are presented in Table 2, where column 1 is a cardinal identifier for this work, and column 2 is the object name in its telescope survey, which is presented in column 5. The coordinates in $J2000$ are in columns 3 and 4. The G magnitude, the effective temperature, $\log g$, stellar mass, and weighted mean period are listed in columns 6, 7, 8, 9, and 10, respectively. The data were taken from the works of Hermes et al. (2017), Guo et al. (2015), Bognar & Sodor (2016), Su et al. (2017), Rowan et al. (2019) and Romero et al. (2022). The objects in rows 15 and 22 does not have their position published in their discovery papers. The 22 LMV are also shown as light-blue dots on Fig. 11. For 4 of them the uncertainties in the atmospheric parameters are quite large, leading to uncertainty in the stellar mass of 0.1–0.4 $\mathrm{M_{\odot}}$.

The pioneering works of Robinson (1979), Robinson (1980) and McGraw (1980) demonstrated the correlation between pulsation period and amplitudes for ZZ Ceti stars. Short pulsation periods ($\sim$ 100 to 300 s) typically have pulsation amplitudes of a few percent, while long pulsation periods ($\geqslant$ 600 s) have large amplitudes, which can be as high as 10% (Mukadam et al., 2006). The behaviour of pulsation periods and amplitudes as a function of temperature was shown more than a decade later, first by Clemens (1993) and later by Kanaan, Kepler & Winget (2002) and Mukadam et al. (2006).

The *Weighted Mean Period* (WMP) is defined by weighting each period with the corresponding observed amplitude. It is given by:

$$\mathrm{WMP} = \frac{\sum_i P_i A_i}{\sum_i A_i}. \tag{3.1}$$

Where P_i is the pulsation period and A_i its amplitude. In combination with temperature, a linear relationship can be extracted. The WMP provides us with a method of determining the temperature of a ZZ Ceti star independent of spectroscopy, as ilustrated in Figure 9, which shows a linear relation between the WMP and temperature calculated by Mukadam

Table 2 – List of the 22 confirmed LMVs. Column 1 is a cardinal identifier for this work. Column 2 is the identifier of the stars in its telescope survey. The coordinates in $J2000$ are in columns 3 and 4. The telescope of its discovery is in column 5 and the G magnitude is listed in column 6. The effective temperature, $\log g$, stellar mass, and WMP are listed in columns 7, 8, 9, and 10. See text for details.

#	Object Name	RA	DEC	telescope	G	$T_{eff}[K]$	$\log g[cm\,s^{-2}]$	Mass $[M_\odot]$	WMP
1	5624184	09:32:48.01	-37:44:28.7	TESS	15.95	$11\,286 \pm 123$	7.588 ± 0.018	0.418	464.8
2	21187072	18:26:06.04	48:29:11.3	TESS	16.28	$11\,808 \pm 228$	7.235 ± 0.025	0.314	1074.5
3	33717565	04:05:36.39	-76:28:28.1	TESS	16.52	$10\,675 \pm 172$	7.639 ± 0.031	0.433	413.9
4	72637474	02:08:07.86	-29:31:38.0	TESS	15.92	$10\,214 \pm 112$	7.209 ± 0.025	0.297	893.9
5	156064657	00:37:23.75	-48:21:55.9	TESS	16.60	$10\,193 \pm 131$	7.295 ± 0.034	0.32	1457.9
6	158068117	06:00:52.91	-46:30:41.1	TESS	16.09	$12\,719 \pm 210$	7.434 ± 0.026	0.376	268.5
7	188087204	10:46:27.80	-25:12:15.8	TESS	16.83	$10\,052 \pm 218$	7.583 ± 0.055	0.412	644.8
8	229581336	18:01:15.37	72:18:49.0	TESS	16.05	$14\,634 \pm 403$	7.425 ± 0.035	0.382	741.4
9	313109945	14:05:40.57	74:38:59.3	TESS	15.59	$9\,059 \pm 134$	7.490 ± 0.04	0.38	386.1
10	724128806	05:37:24.22	-80:45:49.7	TESS	17.48	$9\,776 \pm 239$	7.595 ± 0.065	0.415	290.2
11	1001545355	14:13:53.96	71:36:12.6	TESS	16.99	$11\,244 \pm 232$	7.653 ± 0.036	0.439	709.3
12	1102242692	15:28:09.16	55:39:16.1	TESS	17.09	$10\,343 \pm 223$	7.459 ± 0.051	0.372	746.6
13	J1413+0134	14:43:30.93	01:34:05.8	SDSS	18.70	$10\,450 \pm 240$	7.849 ± 0.170	0.525	1016.4
14	J1502-0001	15:02:07.02	-00:01:47.1	SDSS	18.70	$11\,090 \pm 190$	7.750 ± 0.10	0.495	536.1
15	0210+3302	-	-	HS	16.70	$12\,176 \pm 250$	7.379 ± 0.005	0.361	194.4
16	J0229-0638	02:29:41.29	-06:38:42.7	SDSS	18.21	$9\,791 \pm 34$	7.240 ± 0.100	0.308	754
17	J1150-0553	11:50:57.43	-05:53:06.50	SDSS	17.50	$9\,611 \pm 88$	7.381 ± 0.0021	0.347	403
18	J1507+0748	15:07:39.34	07:48:28.5	SDSS	18.17	$10\,540 \pm 49$	7.812 ± 0.60	0.521	583
19	J0046+3433	00:46:28.31	34:33:19.02	LAMOST	16.33	$11\,681 \pm 199$	7.530 ± 0.150	0.407	473
20	J0103+4337	01:03:02.46	43:37:56.000	LAMOST	18.33	$11\,750 \pm 492$	7.889 ± 0.330	0.547	1174
21	J0130+2737	01:30:33.90	27:37:57.02	LAMOST	18.57	$14\,127 \pm 334$	7.690 ± 0.007	0.481	310
22	KIC210397465	-	-	KEPLER	17.60	$11\,200 \pm 160$	7.713 ± 0.0054	0.479	841

et al. (2006) for a sample of 41 ZZ Ceti from the SDSS-DR4 (top) and 39 ZZ Ceti stars from the BG04 sample (Bergeron et al., 2004; Gianninas; Bergeron; Fontaine, 2005) (bottom). The WMP presents an increasing trend towards lower temperatures, however, there is a significant scatter in these linear relations.

Figure 10 shows the WMP for the sample of LMVs presented in Table 2, in terms of the effective temperature. Only the uncertainties in the effective temperature are presented as the errors in period and amplitude were not published. The dotted lines are the linear relation from Mukadam et al. (2006) presented in Figure 9. The amount of scatter in those linear relations can be explained by uncertainties in the measurement methods. The uncertainty in spectroscopic temperature depends on the quality of the spectrum, and the accuracy and completeness of the model atmosphere to fit the observed spectrum with the template spectra. For the WMP, the uncertainty comes from the quality of the photometric observations and the amplitude modulation of the star. Also, dispersion in the period can happen due to variations in core composition, stellar mass, and boundary of the H/He layer.

Although the Brunt-Väisälä frequency among the ZZ Ceti and LMV are similar, the linear relation for ZZ Ceti can not be extended for the LMVs. In the mass range of the LMVs, the core composition, which can be He or a mix of carbon and oxygen or even carbon-oxygen-helium, together with the formation channel can directly impact the H/He boundary layer which will have an effect in the range of periods. For completeness, the

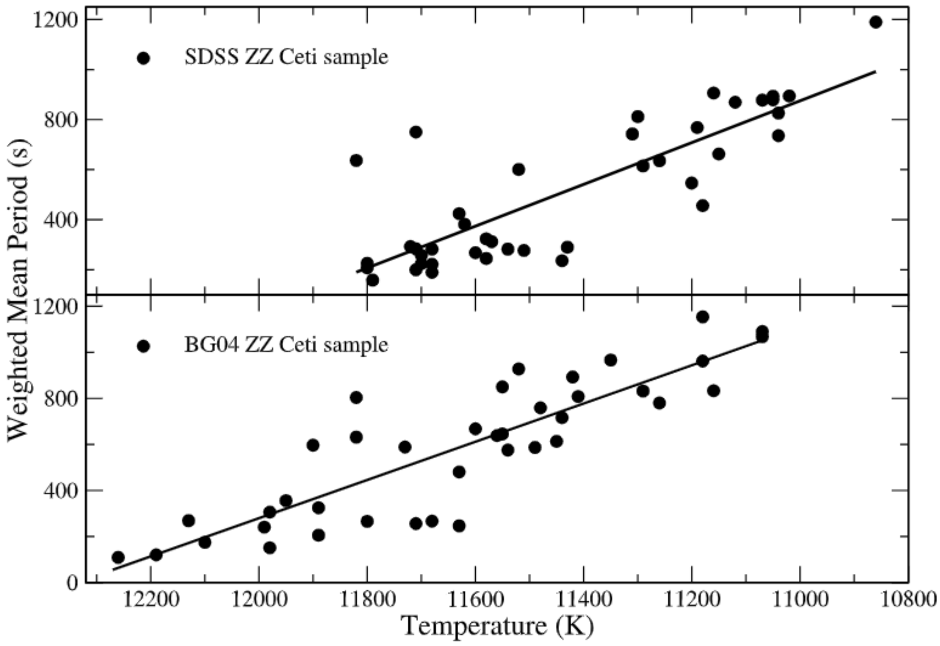

Figure 9 – The WMP as function of the spectroscopic temperature for 41 ZZ Ceti stars from the SDSS (top) and 39 ZZ Ceti stars from the BG04 sample (bottom) (Bergeron et al., 2004; Gianninas; Bergeron; Fontaine, 2005). Adapted from Mukadam et al. (2006).

ELMVs from Figure 7 are also shown as green dots. Those stars appear to follow the linear relation for lower effective temperatures and longer WMP. In this mass range, helium is the main component of the core and the H/He boundary layer is affected mainly by the formation channel. With fewer constraints, the scatter in the period range is lower. However, more data are necessary to confirm the extrapolation of the ZZ Ceti relation for ELMVs.

3.2 LMV Candidates

We selected a list of targets from a sample of the white dwarf catalogue presented by Kepler et al. (2019) from the SDSS data release 14. We choose objects with spectroscopic effective temperature in the range of $12\,500 - 9\,800$ K, within the instability strip of the ZZ Cetis (Tremblay et al., 2015) and mass in the range of $\approx 0.3 - 0.45 M_{\odot}$, considering the uncertainties in the mass determination. Those two selection criteria lead us to a list of ≈ 310 objects. However, another constraint was added in the magnitude, by filtering objects with $g < 18.5$ to be able to observe in the Southern Astrophysical Research (SOAR) telescope or in the Pico dos Dias Observatory (OPD) in Brazil. Finally, our list of 61 candidates are shown in Table 3 and 4, where we list the object's position, g magnitude, effective temperature, surface gravity, and stellar mass, which were estimated by linear interpolation of the evolutionary tracks from Romero et al. (2012), Romero et al. (2013).

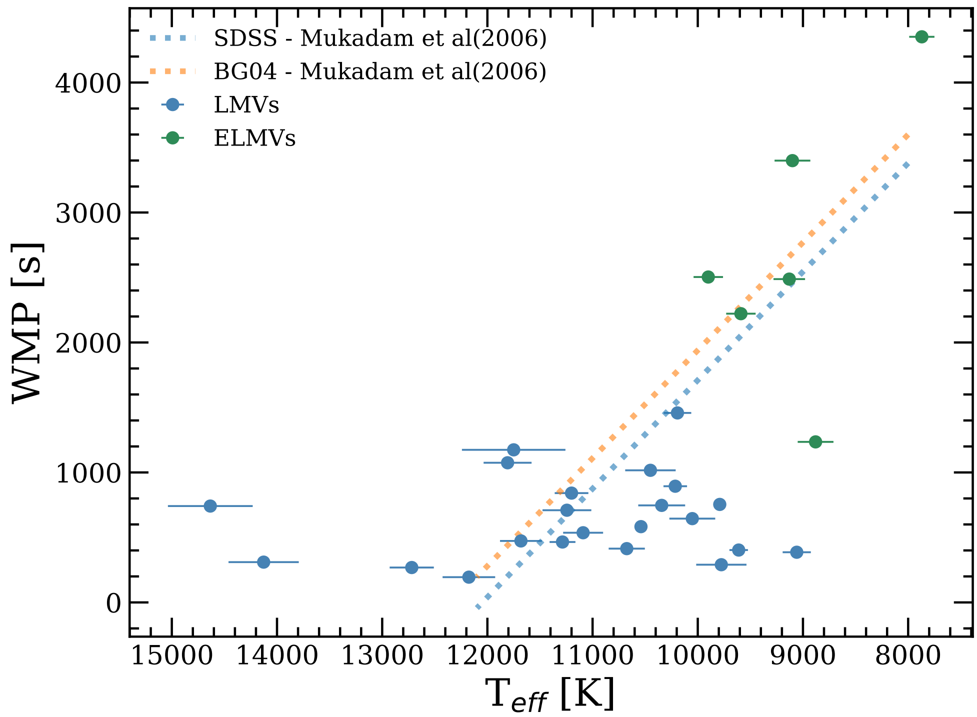

Figure 10 – The Weighted Mean Period (WMP) as a function of the spectroscopic temperature for the LMVs that are presented in Table 2.

The location of the candidates and observed objects on the $T_{\rm eff} - \log g$ plane are depicted in Figure 11 whith red circles and red dots, respectively. Also, the confirmed LMVs from Table 2 are shown as light-blue dots with their effective temperature and surface gravity uncertainties. The two gray stars are the position of J1152+0248, the star that is the subject of this work, with the atmospheric parameters taken from Parsons et al. (2020). The ZZ Ceti stars are shown as black dots and the black dashed lines are theoretical white dwarf sequences with helium-core and mass of 0.272 and 0.324 $M_\odot$ from Istrate et al. (2016), and C/O core with a mass of 0.452 $M_\odot$ from Romero, Campos & Kepler (2015). The blue and red dashed lines are the blue and red edges of the 3D corrected instability strip for ZZ Ceti stars from Tremblay et al. (2015). Note that not all of the LMVs reside within the ZZ Ceti instability strip and they also present higher temperatures than the ZZ Ceti. This shift towards hotter temperatures can be explained by the variations in core composition and boundary of the H/He layer that LMVs have due to their varied formation channels. The ZZ Ceti usually are formed from single stellar evolution and present a more stable period range and core composition, which contrast with the observed results for LMVs.

Table 3 – A sample of 61 LMV candidates. Column 1 is a cardinal identifier for this work. Column 2 is the object ID on the SDSS DR 14. The coordinates in $J2000$ are in columns 3 and 4. The g magnitude, the effective temperature, $\log g$, and stellar mass are listed in columns 5, 6, 7, and 8, respectively. See text for details.

#	Object	RA	DEC	g	$T_{eff}[K]$	$\log g[cm\,s^{-2}]$	Mass $[M_\odot]$
1	J2230-0023	22:30:28.68	-00:23:31.47	15.443	$9\,305 \pm 11$	7.628 ± 0.019	0.437 ± 0.012
2	J2058-0605	20:58:57.10	-06:05:19.43	17.734	$9\,570 \pm 26$	7.683 ± 0.043	0.46 ± 0.025
3	J1212-0123	12:12:58.25	-01:23:10.20	16.774	$9\,812 \pm 19$	7.558 ± 0.029	0.409 ± 0.016
4	J1448+0713	14:48:46.85	+07:13:04.39	17.202	$12\,150 \pm 66$	7.599 ± 0.038	0.437 ± 0.022
5	J1143+0009	11:43:12.57	+00:09:26.51	18.154	$9\,789 \pm 38$	7.484 ± 0.065	0.381 ± 0.031
6	J1151-0007	11:51:56.94	-00:07:25.49	18.140	$9\,755 \pm 37$	7.173 ± 0.08	0.289 ± 0.028
7	J1152+0021	11:52:36.99	+00:21:41.84	17.295	$10\,113 \pm 23$	7.593 ± 0.033	0.424 ± 0.019
8	J1206-0030	12:06:04.13	-00:30:39.48	17.547	$9\,088 \pm 32$	7.634 ± 0.069	0.438 ± 0.041
9	J1234-0038	12:34:52.87	-00:38:19.27	18.215	$9\,548 \pm 51$	7.655 ± 0.105	0.449 ± 0.062
10	J1221-0324	12:21:54.82	-03:24:36.63	18.271	$10\,422 \pm 59$	7.745 ± 0.081	0.489 ± 0.046
11	J1534+0037	15:34:24.85	+00:37:56.05	17.492	$8\,138 \pm 23$	7.7119 ± 0.049	0.466 ± 0.029
12	J2156-0046	21:56:28.26	-00:46:17.14	18.408	$10\,308 \pm 57$	7.5289 ± 0.08	0.399 ± 0.042
13	J2231-0002	22:31:20.96	-00:02:16.39	17.821	$9\,081 \pm 32$	7.609 ± 0.066	0.427 ± 0.039
14	J0321+0053	03:21:50.57	+00:53:12.80	17.983	$8\,530 \pm 25$	7.75 ± 0.057	0.484 ± 0.036
15	J0236-0748	02:36:38.97	-07:48:30.37	18.495	$8\,076 \pm 41$	7.45 ± 0.105	0.361 ± 0.049
16	J0256-0730	02:56:10.61	-07:30:24.61	16.838	$10\,868 \pm 31$	7.6699 ± 0.029	0.460 ± 0.015
17	J0922+0146	09:22:07.11	+01:46:37.16	18.344	$10\,409 \pm 46$	7.671 ± 0.058	0.458 ± 0.033
18	J1442+0214	14:42:42.01	+02:14:48.53	18.393	$8\,864 \pm 49$	7.735 ± 0.058	0.479 ± 0.036
19	J1013+0439	10:13:23.91	+04:39:46.15	18.494	$9\,575 \pm 45$	7.69 ± 0.075	0.462 ± 0.044
20	J1037+0352	10:37:33.82	+03:52:31.56	17.832	$9\,606 \pm 77$	7.7229 ± 0.141	0.476 ± 0.078
21	J1101+0515	11:01:19.74	+05:15:13.78	18.326	$11\,810 \pm 102$	7.5529 ± 0.07	0.416 ± 0.038
22	J0026-1037	00:26:02.29	-10:37:52.02	16.248	$9\,942 \pm 16$	7.6479 ± 0.024	0.447 ± 0.013
23	J2222-0729	22:22:28.16	-07:29:28.80	18.416	$8\,236 \pm 53$	7.569 ± 0.123	0.405 ± 0.068
24	J0015+1353	00:15:18.88	+13:53:32.91	17.277	$8\,372 \pm 24$	7.681 ± 0.055	0.454 ± 0.032
25	J0012+1439	00:12:45.61	+14:39:56.43	18.155	$10\,861 \pm 57$	7.649 ± 0.061	0.452 ± 0.034
26	J1118+0402	11:18:16.40	+04:02:06.73	17.632	$8\,960 \pm 36$	7.73 ± 0.067	0.477 ± 0.041
27	J1141+0420	11:41:32.99	+04:20:28.86	18.172	$11\,508 \pm 98$	7.495 ± 0.075	0.393 ± 0.036
28	J1156+0503	11:56:30.06	+05:03:58.78	17.550	$8\,025 \pm 29$	7.7 ± 0.062	0.461 ± 0.037
29	J1343+0440	13:43:21.33	+04:40:00.72	18.454	$8\,091 \pm 46$	7.4939 ± 0.12	0.376 ± 0.061
30	J1411-0313	14:11:15.81	-03:13:25.60	18.419	$9\,285 \pm 45$	7.7699 ± 0.098	0.496 ± 0.053
31	J2120-0018	21:20:57.74	-00:18:10.71	18.370	$8\,413 \pm 50$	7.649 ± 0.117	0.441 ± 0.070
32	J2127+0019	21:27:52.92	+00:19:16.21	17.606	$8\,116 \pm 27$	7.216 ± 0.062	0.290 ± 0.023
33	J2132+0031	21:32:18.12	+00:31:58.82	18.004	$10\,051 \pm 37$	7.1669 ± 0.067	0.289 ± 0.023
34	J1029+0604	10:29:34.97	+06:04:18.06	18.163	$11\,909 \pm 89$	7.577 ± 0.060	0.426 ± 0.033
35	J1112+1012	11:12:49.26	+10:12:42.67	18.265	$8\,759 \pm 60$	7.7089 ± 0.099	0.467 ± 0.061
36	J0941+0856	09:41:22.16	+08:56:43.98	17.917	$8\,017 \pm 31$	7.581 ± 0.078	0.409 ± 0.045
37	J1228+1317	12:28:30.04	+13:17:23.66	18.414	$8\,957 \pm 55$	7.729 ± 0.096	0.476 ± 0.059
38	J1030+1249	10:30:12.29	+12:49:50.70	17.827	$9\,237 \pm 27$	7.7409 ± 0.053	0.483 ± 0.033
39	J1059+1514	10:59:32.55	+15:14:43.59	18.452	$9\,662 \pm 46$	7.7569 ± 0.077	0.492 ± 0.044
40	J1229+1353	12:29:42.64	+13:53:31.79	18.082	$8\,835 \pm 49$	7.766 ± 0.087	0.493 ± 0.048
41	J1259+1544	12:59:44.60	+15:44:56.23	18.207	$9\,949 \pm 42$	7.5129 ± 0.063	0.392 ± 0.032
42	J1246+0739	12:46:28.84	+07:39:26.18	18.318	$8\,325 \pm 42$	7.73 ± 0.101	0.474 ± 0.062
43	J1326+0910	13:26:45.42	+09:10:56.38	18.027	$8\,582 \pm 54$	7.3259 ± 0.109	0.325 ± 0.045
44	J1359+0544	13:59:31.90	+05:44:20.61	16.003	$10\,089 \pm 14$	7.368 ± 0.021	0.345 ± 0.008
45	J1521+0439	15:21:49.02	+04:39:28.21	17.829	$8\,785 \pm 38$	7.617 ± 0.064	0.429 ± 0.038

Table 4 – Continuation of Table 3

#	Object	RA	DEC	g	$T_{eff}[K]$	$\log g[cm\, s^{-2}]$	Mass $[M_\odot]$
46	J1040+0834	10:40:57.48	+08:34:21.64	18.111	$9\,806 \pm 36$	7.365 ± 0.071	0.343 ± 0.029
47	J1015+1850	10:15:01.07	+18:50:06.35	18.434	$10\,822 \pm 70$	7.488 ± 0.084	0.387 ± 0.040
48	J0833+1135	08:33:44.30	+11:35:16.88	17.698	$12\,063 \pm 87$	7.524 ± 0.048	0.406 ± 0.024
49	J0905+1642	09:05:43.45	+16:42:10.10	18.346	$8\,542 \pm 46$	7.742 ± 0.114	0.480 ± 0.064
50	J1109+1719	11:09:53.11	+17:19:34.90	18.209	$9\,567 \pm 33$	7.74 ± 0.054	0.484 ± 0.034
51	J1554+1408	15:54:12.24	+14:08:04.80	17.352	$8\,264 \pm 26$	7.721 ± 0.059	0.470 ± 0.036
52	J1305+2014	13:05:50.96	+20:14:50.30	18.373	$8\,508 \pm 45$	7.5199 ± 0.091	0.387 ± 0.048
53	J1340+2044	13:40:07.00	+20:44:57.26	18.094	$8\,006 \pm 38$	7.697 ± 0.089	0.459 ± 0.055
54	J1356-0920	13:56:39.76	-09:20:20.91	17.331	$8\,478 \pm 20$	7.73 ± 0.045	0.475 ± 0.027
55	J1356+1646	13:56:59.28	+16:46:42.84	18.033	$8\,273 \pm 33$	7.6859 ± 0.07	0.456 ± 0.042
56	J1411+1630	14:11:03.32	+16:30:34.22	17.358	$8\,828 \pm 34$	7.7229 ± 0.057	0.473 ± 0.034
57	J1455+1703	14:55:30.63	+17:03:17.81	18.297	$10\,226 \pm 44$	7.593 ± 0.058	0.425 ± 0.0342
58	J1532+1420	15:32:31.27	+14:20:39.34	17.850	$8\,891 \pm 37$	7.7309 ± 0.067	0.477 ± 0.0417
59	J1422+1929	14:22:44.92	+19:29:43.44	18.491	$10\,205 \pm 53$	7.4909 ± 0.073	0.385 ± 0.035
60	J1137-0027	11:37:38.37	-00:27:21.66	17.952	$8\,396 \pm 29$	7.7489 ± 0.057	0.483 ± 0.0367
61	J0136+1250	01:36:58.84	+12:50:41.83	18.074	$8\,012 \pm 22$	7.726 ± 0.044	0.471 ± 0.026

Table 5 – Journal of observations for the observed candidates. Column 1 is the object ID on the SDSS DR 14 and their coordinates in $J2000$ are shown in columns 2 and 3. The g magnitude, telescope, and start date and time of observations are listed in columns 4, 5, and 6, respectively. Columns 7 and 8 show the integration time $t_{\rm exp}$ of each exposure and the Δt, which is the total length of each observing run.

Object	RA	DEC	g	Telescope	Run start (UT)	$t_{\rm exp}$ (sec)	Δt (h)
J2230-0023	22:30:28.68	-00:23:31.47	15.443	SOAR	2021-07-04 05:58:57.82	15	2.06
J2058-0605	20:58:57.10	-06:05:19.43	17.734	SOAR	2021-07-04 03:19:37.85	50	2.6
J1212-0123	12:12:58.25	-01:23:10.20	16.774	OPD	2021-06-12 22:36:50.87	35	4.25
J1448+0713	14:48:46.85	+07:13:04.39	17.202	OPD	2021-06-14 01:07:52.87	20	2.95

3.2.1 Observational data

The first four objects presented in Table 3 were observed and the description of the telescopes, nights of observations, and data reduction and analysis are described as follows. We employed Goodman image mode on the 4.1 m SOAR Telescope in 2021. All observations were obtained with a red blocking filter S8612 and read-out mode 200 Hz ATTN2 with the CCD binned 2×2 and an ROI reduced to 800×800. The integration times vary from 15 to 50 s, depending on the magnitude of the object and the weather conditions. Two objects were observed using the I×ON camera on the 1.6 m Perkin Elmer Telescope at the OPD observatory in 2021. We also used a red-blocking filter BG40. The integration times vary from 20 to 35 s, depending on the magnitude of the object. The journal of observations is shown in Table 5.

The reduction of the raw data frames was computed with the `IRAF` software (Tody, 1986; Tody, 1993). It was performed bias and flat filed corrections before the aperture photometry, which was calculated with the `DAOPHOT` routine (Stetson, 1987). Light curves of all bright stars in the field were extracted. Then, we divided the light curve of the

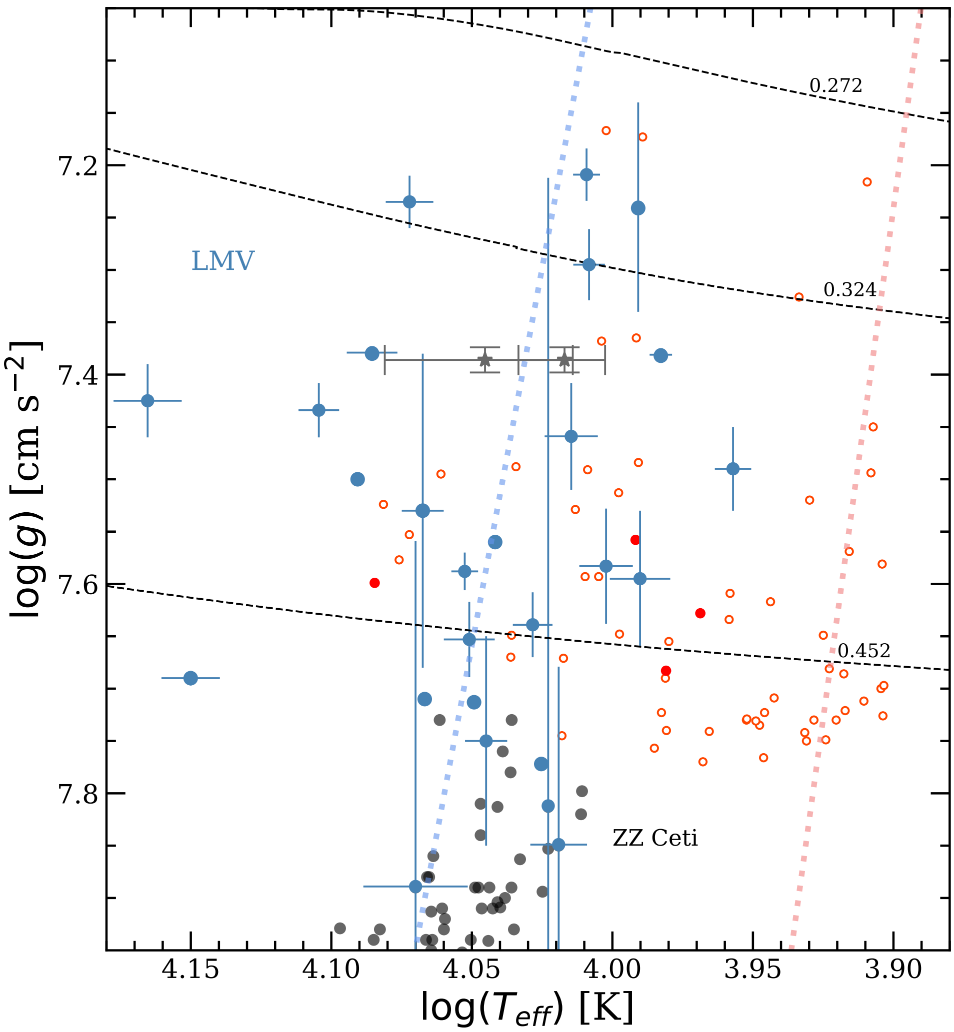

Figure 11 – Confirmed LMVs and candidates. This figure is a zoomed section of Figure 7 focusing on a region of $4.15 \leq \log T_{eff} \leq 3.9$. The black dots are the ZZ Ceti stars, the light-blue dots are the confirmed LMV, the hollow red circles are the LMV candidates, and the red dots are the observed candidates presented in a further section of this work. See text for details.

target star by the light curves of all comparison stars to minimise the effects of sky and transparency fluctuations and choose a comparison that maximises the signal-to-noise ratio. To look for periodicities in the light curves, we calculate the Fourier Transform (FT) using the software `Period04` (Lenz; Breger, 2004). We accepted a frequency peak as significant if its amplitude exceeds an adopted significance threshold of 4σ where σ is the mean amplitude of the FT. This significance criterion corresponds to a probability of the peak being due to noise smaller than 1 in 1000 (Kepler, 1993). Then, we used the process of pre–whitening the light curve by subtracting out the data of a sinusoid with the same frequency, amplitude, and phase of the highest peak and then computing the FT of the residuals. This process is repeated until there are no new significant signals.

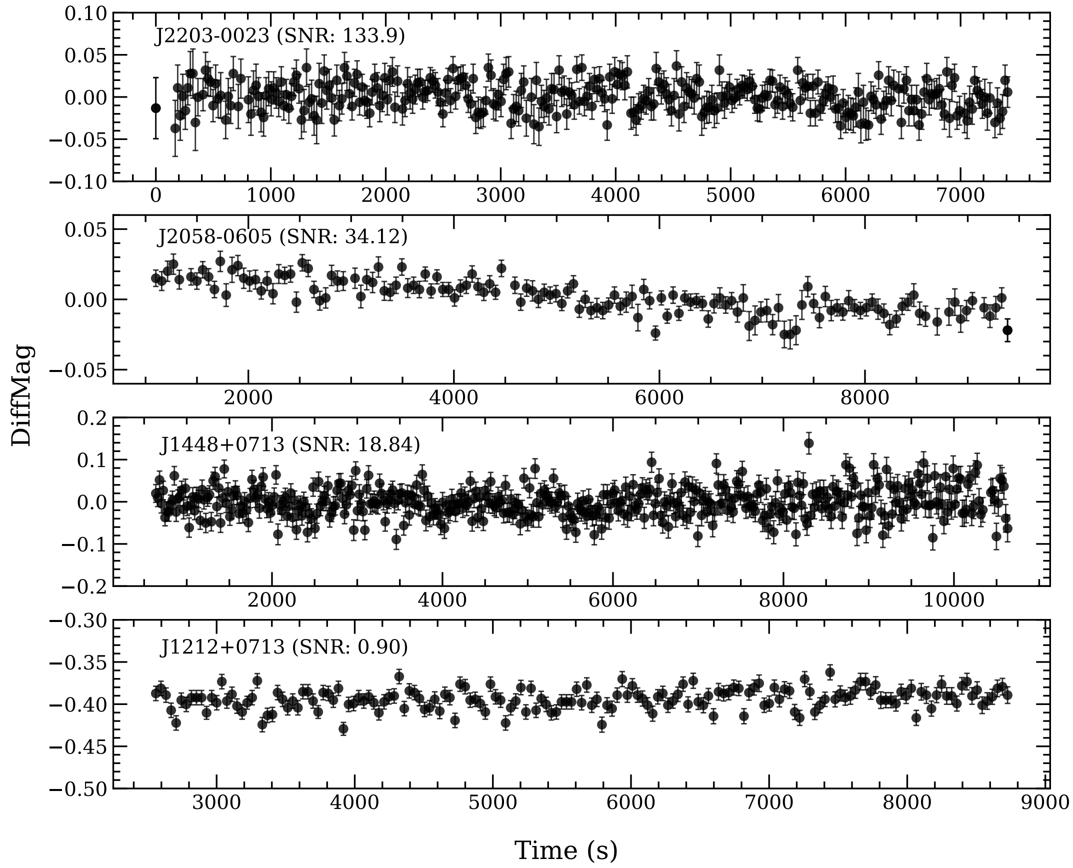

Figure 12 – Light curves of the observed candidates and its signal-to-noise ratio.

Figure 12 presents the light curves of the four observed objects and their signal-to-noise ratio (SNR). Note that only the first panel presents a light curve with SNR > 100. The poor weather condition of the observation nights increased the noise in the images preventing them from reaching SNR of ~ 1000. Figure 13 shows the FT of those light curves. The orange and red dashed lines in Figure 13 are the detection limits of 3σ and 4σ, respectively. From the FT presented in Figure 13, we did not detect any variability within the 4σ detection limit. Only one object, J1448+0713 presents a peak over the 3σ line but below the 4σ line. However, this peak corresponds to the time interval between consecutive observations and thus it is discarded for not being a real period.

The observed objects presented in this thesis can be classified as *Not Observed to Vary* (NOV). However, given that the period in LMV ranges from ~ 200 s to ~ 1400 s, as shown in Table 2, follow-up observations with better weather conditions and at least a grey sky are necessary to reduce the integration time to around 10 s to 15 s in order to

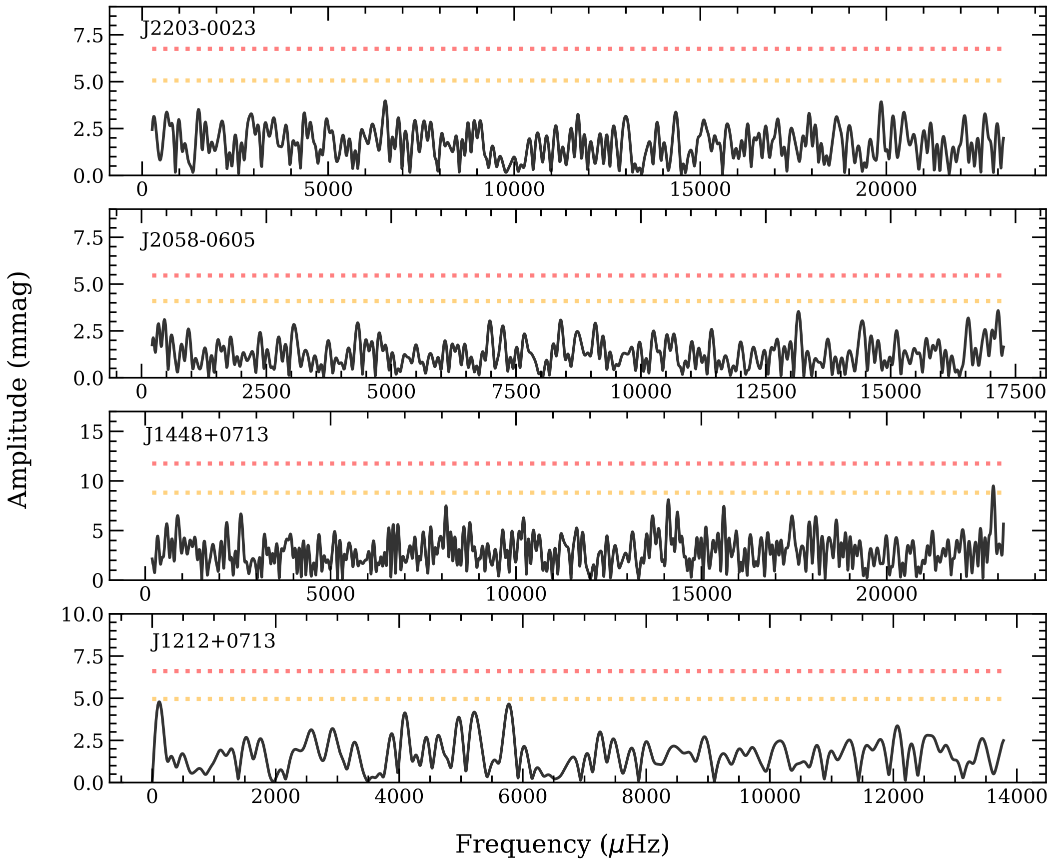

Figure 13 – Fourier transform of the observed candidates. The dashed lines are the detection limit of 3σ (orange) and 4σ (red).

detect shorter periods ($\sim$ 200 s) and to increase the SNR to 1000, as the observed periods of confirmed LMVs have milliamps variations. Also, observation times greater than 2 hrs are necessary to detect longer periods ($>$ 800s).

4 Current Results

The results and discussion presented in this chapter belong to the paper entitled "Uncovering the chemical structure of the pulsating low-mass white dwarf SDSS J115219.99+024814.4", published in the journal *Monthly Notices of the Royal Astronomical Society* and available at appendix B (Romero et al., 2021).

4.1 The case of the binary system J1152+0248

The binary system J1152+0248 was first reported by Hallakoun et al. (2016), based on K2 data from the *Kepler* mission. It is a close eclipsing binary system (orbital period of 2.4 h) composed of two low mass white dwarfs. Recently, Parsons et al. (2020) reported the discovery of pulsations on the lower mass companion, which become the first reported pulsating low-mass white dwarf in a compact eclipsing binary system.

Parsons et al. (2020) performed time-series spectroscopy with the X-shooter (Vernet et al., 2011) on the 8.2 m Very Large Telescope and 108 min of high-speed photometry observations with HiPERCAM (Dhillon et al., 2018) on the 10.4 m Gran Telescopio Canárias in five different bands, covering both primary and secondary eclipses. From the high time-resolution light-curves they found pulsation-related variations from the cooler component with at least three significant periods. To determine the mass and radius of each component in J1152+0248, they combine radial-velocity determinations from X-shooter with the information extracted from the primary and secondary eclipses in the light curves. The effective temperature was determined using two techniques, i.e. by fitting the spectral energy distribution ($T_{\rm eff}$ (SED)) and by modelling the light curves including the effects of the eclipses ($T_{\rm eff}$(Eclipse)). The stellar parameters obtained by Parsons et al. (2020) for the pulsating component in J1152+0248 (hereafter J1152+0248−V) are listed in Table 6.

Based on the determination of the radius, the authors proposed that J1152+0248−V is either a hybrid-core or a helium-core low-mass WDs with an extremely thin surface hydro-

Table 6 – Stellar parameters presented in Parsons et al. (2020) for the pulsating component of the J1152+0248 eclipsing binary.

Parameter	Value
$M_*/M_\odot$	0.325 ± 0.013
$R_*/R_\odot$	0.0191 ± 0.0004
$\log$ (g/[g cm^{-2}])	7.386 ± 0.012
$T_{\rm eff}$/K (SED)	$11\,100^{\pm 950}_{770}$
$T_{\rm eff}$/K (Eclipse)	$10\,400^{\pm 400}_{340}$

gen layer ($M_H/M_\odot < 10^{-8}$). However, different inner chemical structures will influence the period spectrum of a pulsating star. Consequently, an asteroseismological study of this object can help to elucidate both the chemical composition and the mass of the hydrogen envelope.

4.2 Evolutionary Sequences

The evolutionary models presented in this work are part of a grid of models covering the mass interval where helium- and hybrid-core white dwarfs overlap, i.e. ~0.32–0.45 $M_\odot$ (Istrate; et. al., in preparation). Since the aim of this work is uncovering the core-composition of J1152+0248−V using asteroseismology, we only consider sequences compatible with its observed effective temperature and radius. Therefore, we focus on evolutionary sequences for a white dwarf mass of 0.325 $M_\odot$, corresponding to the value obtained by Parsons et al. (2020), and 0.338 $M_\odot$, i.e. the maximum WD mass compatible within 1σ with the derived mass of J1152+0248−V. Table 7 shows the binary configuration leading to the formation of the four cases of low mass white dwarfs, composed of two masses and two core compositions for each mass.

Figure 14 shows the evolution of the donor star in the Kiel diagram leading to a 0.338 $M_\odot$ white dwarf with helium- (solid orange line) and hybrid-core (blue dashed line). The sequences are computed from the ZAMS until the white dwarf cools down to an effective temperature of 5 000 K on the cooling sequence. In both cases, the companion star is treated as a point mass. In Figure 14, the circle symbol depicts the beginning of the mass-transfer by stable RLOF. The end of the mass-transfer phase is marked with a star. The beginning and the end of the core-helium burning phase are shown with the square and thin diamond symbol, respectively. Finally, the beginning of the cooling track is represented by the diamond symbol.

Table 7 – Binary system configurations. The white dwarf mass and core composition on the end of the cooling sequence are listed in columns 1 and 2. The donor‘s and the accretor‘s mass are shown in columns 3 and 4. Lastly, the orbital period is listed in column 5.

M_{WD} [$M_\odot$]	Core	M_d [$M_\odot$]	M_a [$M_\odot$]	P [days]
0.338	He	1.3	1.2	16.98
0.338	Hybrid	2.3	2	1.99
0.325	He	1.3	1.2	11.75
0.325	Hybrid	2.3	2	1.43

After the end of the mass-transfer phase (star marker on Figure 14), the remnant evolves through the proto-white dwarf phase, in which the star remains with a degenerate helium core that does not ignite due to its low mass. At this stage, the star contract and increases its effective temperature, until the beginning of the cooling sequence. The contraction also increases the temperature in the hydrogen shell leading to unstable hydrogen-burning (CNO burning). The release of energy due to the hydrogen-burning occurs as a flash, that develops a pulse-driven convection zone due to a steep temperature gradient. This convection zone expands towards the stellar surface. Later, its lower boundary moves upwards and the convection zone vanishes. After that, the inner shells contracts while the surface layers react by expansion, which results in a redward motion in the HR diagram that almost brings the proto-white dwarf back to the RGB stage. Finally, the whole star contracts again, while increasing its effective temperature, before reaching the final cooling stage.

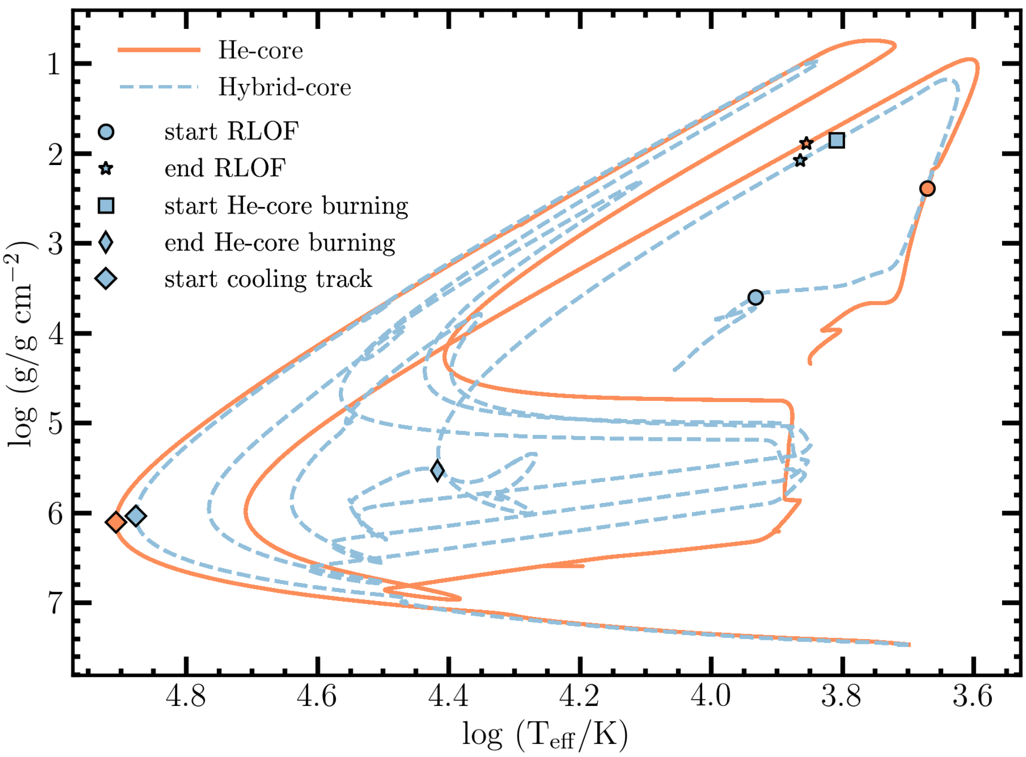

Figure 14 – The Kiel diagram showing the formation and the cooling evolution of a 0.338 $M_\odot$ He- (solid orange line) and hybrid-core (dashed blue line) white dwarf. the circle symbol depicts the beginning of the mass-transfer by stable RLOF. The end of the mass-transfer phase is marked with a star. The beginning and the end of the core-helium burning phase are showed with the square and thin diamond symbol, respectively. Finally, the beginning of the cooling track is represented by the diamond symbol.

The hybrid-core white dwarfs are formed by a 2.3 $M_\odot$ intermediate-mass donor star with a companion of 2.0 $M_\odot$ and an orbital period of ∼1.43 days and ∼1.99 days, for the progenitor of the 0.325 $M_\odot$ and 0.338 $M_\odot$, respectively. In these cases, the mass-transfer phase starts at the Hertzsprung gap, i.e. the region between MS and RGB, and ceases due to the core-helium ignition. The core-helium burning phase lasts around 670 Myrs. Once the CO-core is formed, the proto-white dwarf undergoes four hydrogen shell flashes before finally settling on the cooling track.

Because the mass of the hydrogen envelope is one of the main factors that influence the cooling evolution of a white dwarf, we computed white dwarf cooling sequences with hydrogen envelopes thinner than the ones obtained from the binary evolutionary models described in Figure 14. These sequences were computed using *relaxation* methods available in MESA. The initial conditions were taken at the beginning of the cooling track, i.e. the point of maximum effective temperature, then we removed the desired amount of hydrogen from the stellar chemical profile while keeping the total mass unchanged. The reason for these additional sequences is due to the mass of the hydrogen envelope being one of the main factors that influence the cooling evolution of a white dwarf.

Figures 15 and 16 shows the white dwarf radius as a function of the effective temperature for sequences with helium- (top panels) and hybrid-core (bottom panels). For each core composition, we consider different values of the hydrogen envelope mass, starting from the value resulting from the binary evolution down to 10^{-8} $M_\odot$. In particular, for the stellar mass of 0.325 $M_\odot$ and helium core, we also included a sequence with hydrogen mass of 10^{-10} $M_\odot$. Overplotted are the measured values of J1152+0248−V, both from the eclipse and the SED fitting.

As expected, the radius for the hybrid-core sequences is smaller than for the helium-core sequences, for the same hydrogen envelope mass. Intriguingly, the observations are not compatible with a thick hydrogen envelope, i.e. that obtained from binary evolution computations. For sequences characterized with a stellar mass of 0.338 $M_\odot$, the hydrogen envelope mass consistent with the radius and effective temperature from Parsons et al. (2020) is between 10^{-4} and 10^{-6} $M_\odot$ if we consider a hybrid core. For the sequences with a helium core, the hydrogen envelope is below 10^{-5} $M_\odot$. For sequences with a stellar mass of 0.325 $M_\odot$, the hydrogen envelope mass needs to be even smaller to fit the observations, between 10^{-5} and 10^{-8} $M_\odot$ for sequences with a hybrid core and between 10^{-6} and 10^{-10} $M_\odot$ for sequences with a helium core. Thus, J1152+0248−V has a hydrogen envelope thinner than that obtained from evolutionary sequences, independently of the central chemical composition.

4.3 Abundance and characteristic frequencies

To compare the pulsation properties of helium- and hybrid-core white dwarf models, we chose one template model for each central composition, with stellar mass of 0.338 $M_\odot$, effective temperature of 10 000 K and hydrogen envelope mass of 10^{-4} $M_\odot$. These models are presented in Figure 17, being the helium-core on the left column and the hybrid-core on the right.

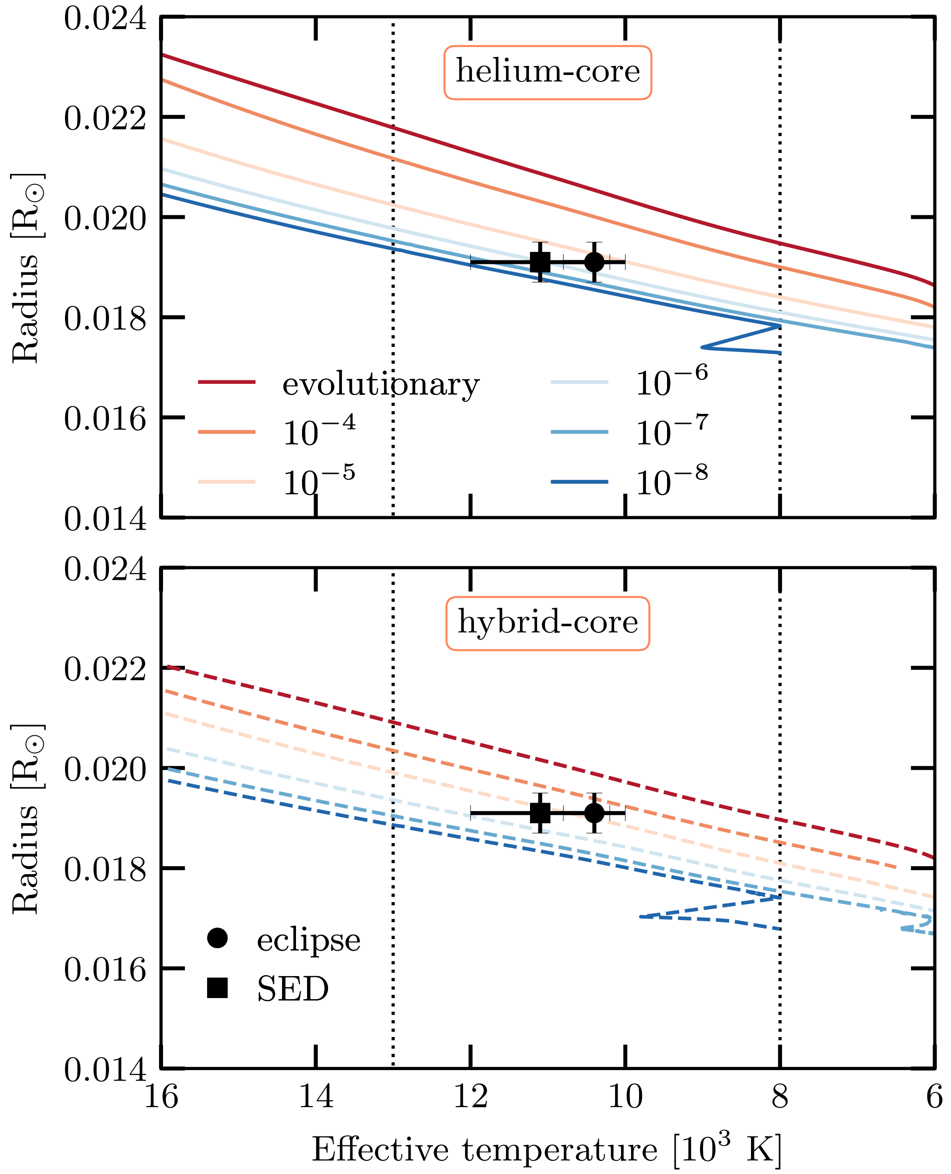

Figure 15 – Stellar radius as a function of the effective temperature for both hybrid- (dashed lines) and helium-core (solid lines) white dwarf sequences. The symbols correspond to the determinations of the effective temperature from observations (see table 6). The dotted vertical lines indicate the blue and red edges of the observed instability strip for low-mass white dwarfs. This region has an evolutionary timescale of $\sim 6 \times 10^8$ years.

In the top row of Figure 17, the chemical profiles are shown. Both template models show a pure hydrogen envelope, since gravitational settling had enough time to separate the elements in the outer layers. For the hybrid-core model, we have a second chemical transition (He/C/O transition) around $r/R \sim 0.4$, where the helium abundance decreases towards the center while the carbon and oxygen abundance increase.

The bottom row of Figure 17 shows the run of the logarithm of the Brunt-Väisälä and Lamb frequencies as a function of radius for the template models. As expected, the

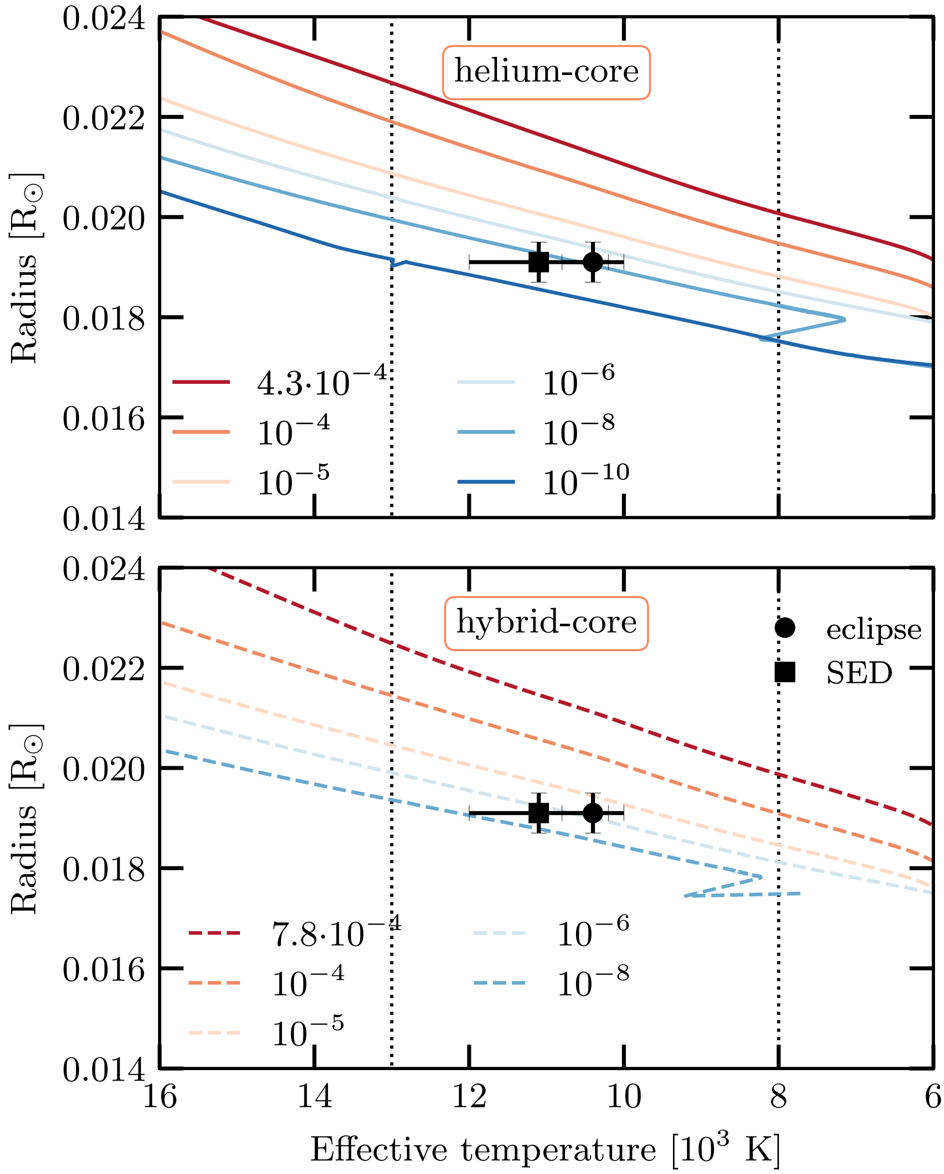

Figure 16 – Same as Figure 15 but for the white dwarf sequences with stellar mass 0.325 $M_\odot$.

bumps in $\log N^2$ correspond to the chemical transition, where the chemical gradients have non-negligible values (Tassoul; Fontaine; Winget, 1990). For both template models, the Brunt-Väisälä frequency shows a bump corresponding to the H/He transition at $r/R \sim 0.9$. However, for the hybrid-core template model, the Brunt-Väisälä frequency also shows a structure corresponding to the He/C/O transition around $r/R \sim 0.4$. This transition is wide and shows three peaks due to the structure of the chemical gradients. We expect that the different profiles for the Brunt-Väisälä frequency for helium-core and hybrid-core models will impact the period spectrum. The Lamb frequency is only sensitive to the H/He transition at the bottom of the hydrogen envelope, as is the case for ZZ Ceti stars (Romero et al., 2012). Thus we do not believe the pressure modes could give information

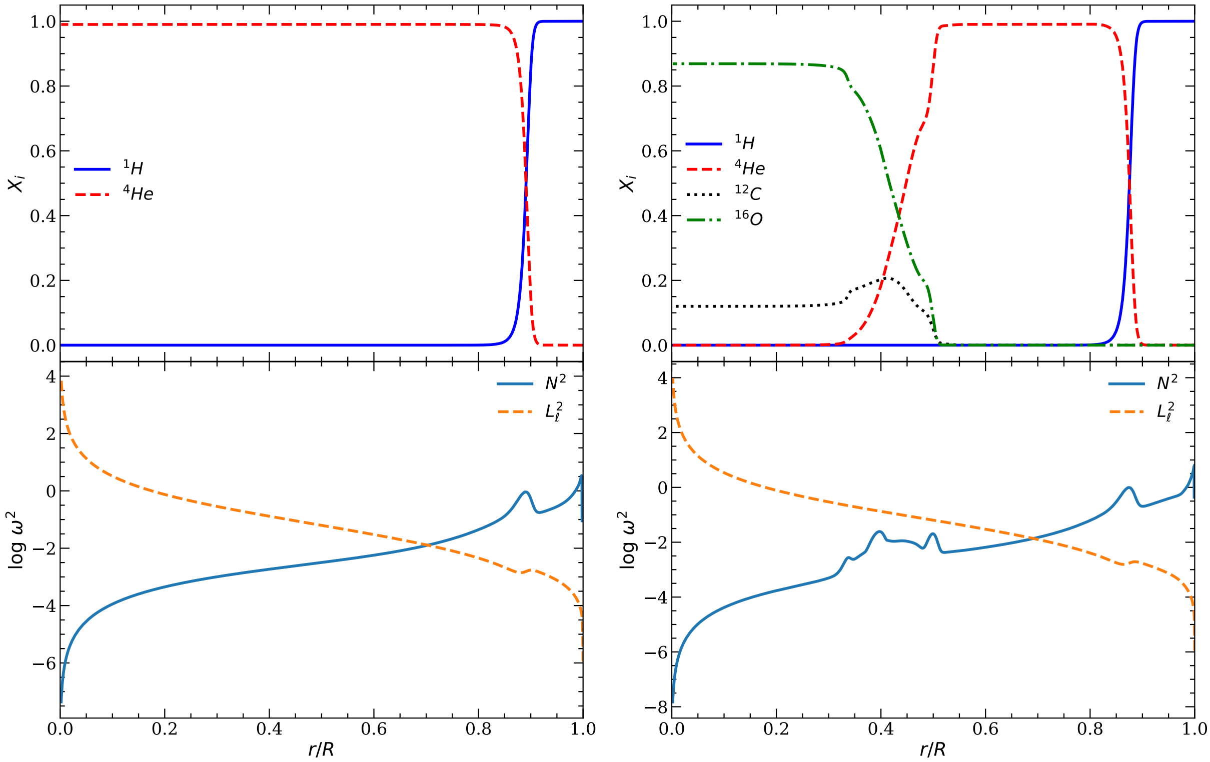

Figure 17 – Abundance profiles and characteristic frequencies for a cooling sequence white dwarf with M=0.338 $M_\odot$, T_{eff} = 10 000 K and $M_H = 10^{-4}$ $M_\odot$. Left column is a *helium-core* and right column a *hybrid-core* white dwarf. *Top* row: the mass fraction of hydrogen, helium, carbon and oxygen as a function of the relative radius. *Bottom* row: the logarithm of the Brunt-Väisälä (blue line) and the Lamb (dashed orange line) characteristic frequencies as a function of the relative radius.

on the inner regions if ever detected in low-mass white dwarf stars.

4.4 Adiabatic Pulsations and its Properties

We computed adiabatic pulsations for the helium- and hybrid-core models with varying hydrogen layer mass, in the effective temperature range of 13 000 and 8 000 K, which covers the empirical instability strip. We computed the period spectrum for $\ell = 1$ and $\ell = 2$ gravity modes with periods in a range of 80 s $\leq \Pi \leq$ 2 000 s. In this section, we will focus on models with a stellar mass of 0.338 $M_\odot$, however, similar results were found for models with a stellar mass of 0.325 $M_\odot$.

Figures 18 and 19 show the forward period spacing as a function of the period, for $\ell = 1$ and $\ell = 2$, respectively. Top panels correspond to models with helium-core while lower panels show the results for hybrid-core models. Each column corresponds to sequences with different values for the hydrogen-envelope mass and each curve shows the forward period spacing at a different effective temperature along the cooling curve, from

12 000 K to 9000 K.

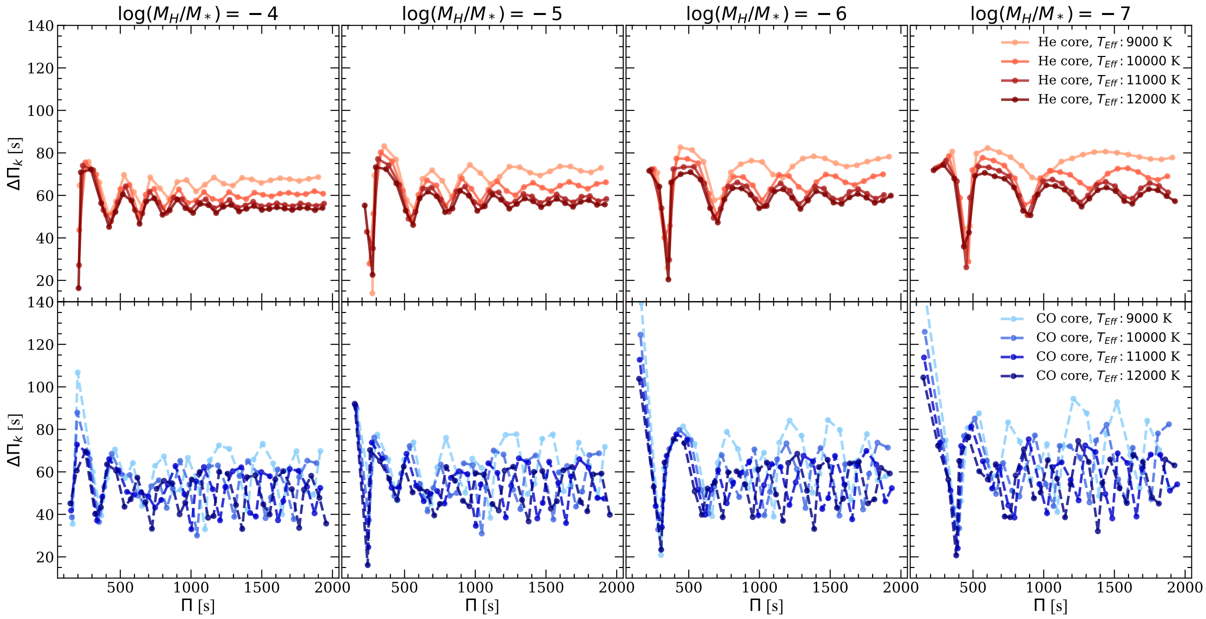

Figure 18 – The forward period spacing as a function of the period for modes with $\ell = 1$ for helium-core (*top* panels) and hybrid-core (*bottom* panels) models. Each column corresponds to a different hydrogen envelope mass. In each plot we show the period spacing for four effective temperatures along the cooling sequence, 12 000, 11 000, 10 000 and 9000 K.

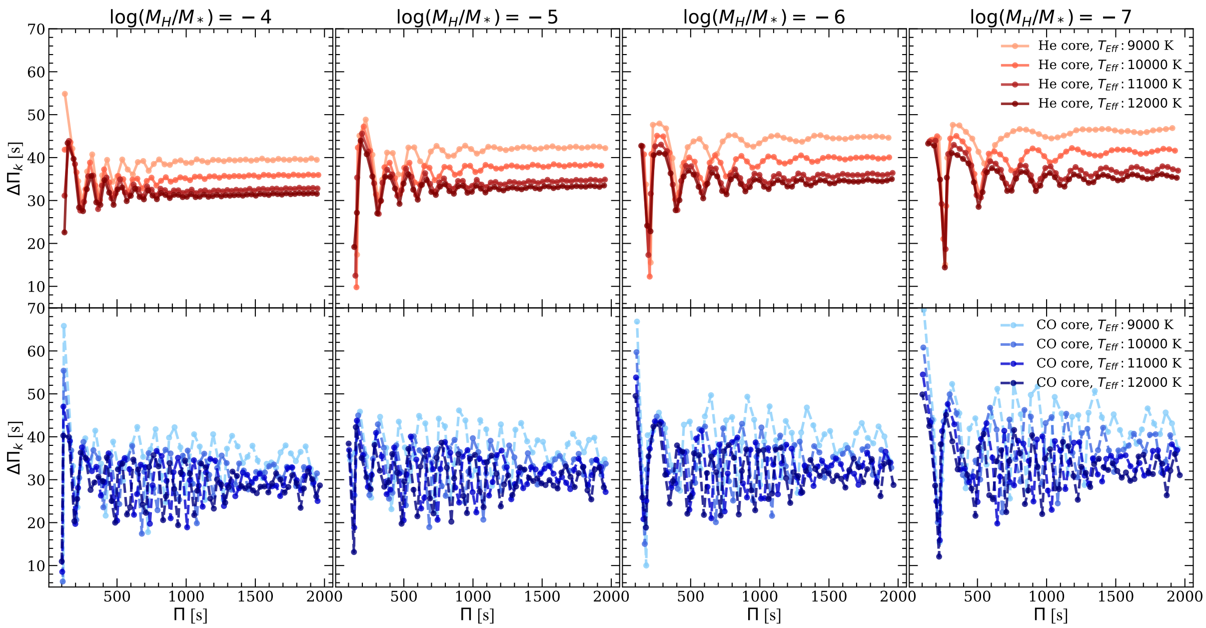

Figure 19 – Same as Figure 18 but for $\ell = 2$ modes.

For the helium-core models the distribution for the forward period spacing as a function of the period, shows a simple trapping cycle characteristic of one-transition models (Brassard et al., 1992; Córsico; Althaus, 2014), with defined local minima, as shown in the upper panels of Figures 18 for $\ell = 1$ and 19 for $\ell = 2$. For the hybrid-core models (lower panels in Figs. 18 and 19) the pattern in the forward period spacing is more complex largely due to the influence of the He/C/O transition in the Brunt-Vaisälaä frequency.

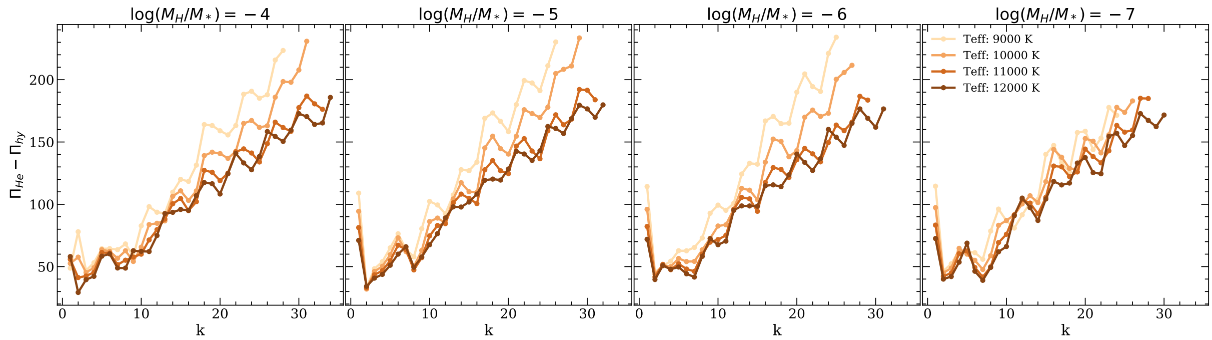

Figure 20 – The period difference as a function of the radial order for $\ell = 1$ modes. Each plot corresponds to a different hydrogen envelope mass. We consider four effective temperatures.

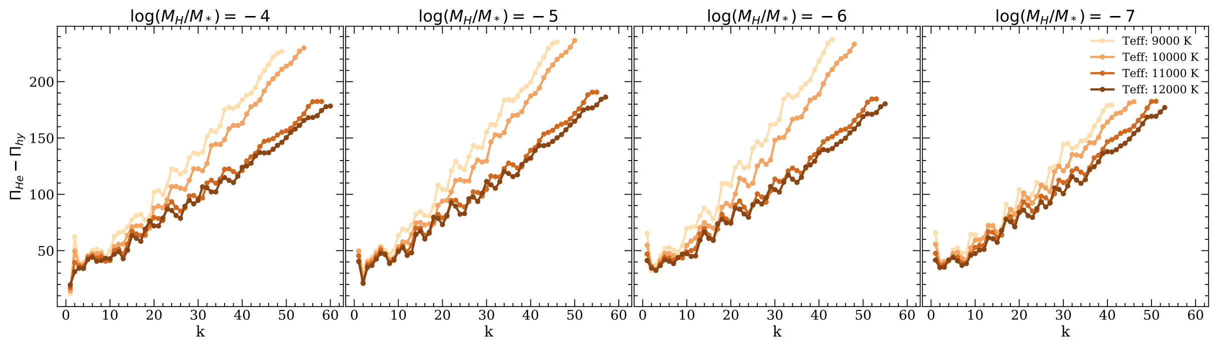

Figure 21 – Same as figure 20 but for modes with $\ell = 2$.

Figures 20 and 21 show the period difference between the helium- and the hybrid-core models, $\Pi_{\rm He} - \Pi_{\rm hy}$ as a function of the radial order k, for harmonic degree $\ell = 1$ and $\ell = 2$, respectively. Each column corresponds to a different hydrogen envelope mass, while the curves in each panel correspond to four different effective temperatures along the WD cooling track. In all cases, the difference in the periods between the helium- and hybrid-core models are between ~ 50 s, for $k \lesssim 10$ and short periods, and ~ 200 s for $k \gtrsim 30$ and longer periods. The period difference is always positive, which means that for a given radial order, the helium-core model period is larger than the period corresponding to the hybrid-core model. Also, the period difference is larger for lower effective temperatures as the periods increase with the cooling age.

4.5 Asteroseismology of J1152+0248−V

In Table 8 we list the detected pulsation periods and their corresponding amplitudes, as reported by Parsons et al. (2020), with the longest period having the highest amplitude.

Table 8 – Observed pulsation periods and the corresponding amplitudes for J1152+0248−V (Parsons et al., 2020).

Period [s]	amplitude [ppt]
1314 ± 5.9	33.0 ± 1.3
1069 ± 13	9.8 ± 1.3
582.9 ± 4.3	8.9 ± 1.3

In order to find the theoretical model that better matches the observed periods, we use a standard χ^2 approach where we search for a minima of the quality function, defined by equation 1.28.

In our fit, we consider the mode with the highest detected amplitude, as an $\ell = 1$ mode, since the amplitude is expected to decrease with increasing harmonic degree due to geometric cancellation. For the remaining two observed periods we allowed them to be fitted by $\ell = 1$ and $\ell = 2$ modes. In addition, we consider the period uncertainties reported by Parsons et al. (2020, Table 8) as an additional restriction in the fitting process. The results of our seismological fit are shown in Figure 22. The value of χ^2 (colour scale) as a function of the effective temperature and the mass of the hydrogen-envelope. The top panels correspond to models with a stellar mass of 0.338 $M_\odot$, while bottom panels show the result for models with 0.325 $M_\odot$. Models with helium-core are depicted on the left-hand panels, while hybrid-core are shown on the right-hand panels. The dashed-line rectangle indicates the region where the models are compatible with the radius and effective temperature determinations from Parsons et al. (2020, Table 6). There are several families of solutions shown in Figure 22. For a stellar mass of 0.325 $M_\odot$, the best-fitting models are mainly characterized by thick hydrogen envelopes ($\sim 10^{-4}$ $M_\odot$) and low effective temperatures ($> 10\,000$ K), for both core compositions. For a stellar mass of 0.338 $M_\odot$, thin hydrogen envelopes ($\sim 10^{-5}$ $M_\odot$) solutions are found for hybrid core and all the effective temperatures range. The number of seismological solutions is largely reduced when we combine our results with the restrictions from the radius and effective temperature presented by Parsons et al. (2020) (dashed-line rectangle in Figure 22). In particular, the models characterized by a hybrid-core structure are the ones satisfying both criteria.

In Table 9 we list the best fit models that minimize the quality function χ^2, considering the uncertainties in the observed periods and are in agreement with the determinations of radius and effective temperature presented by Parsons et al. (2020). Note that all the models are characterized by a hydrogen envelope mass of 10^{-6} $M_\odot$ and a hybrid core. Model 1 shows the lowest value of χ^2 and has a white dwarf mass of 0.338 $M_\odot$. Note that the value of χ^2 for models 2 and 3, which also have a white dwarf mass of 0.338 $M_\odot$, is 1.03 and 1.07 times higher than that for model 1, respectively. The only model with a stellar mass of 0.325 $M_\odot$ is model 4 which has a χ^2 value 1.16 times higher

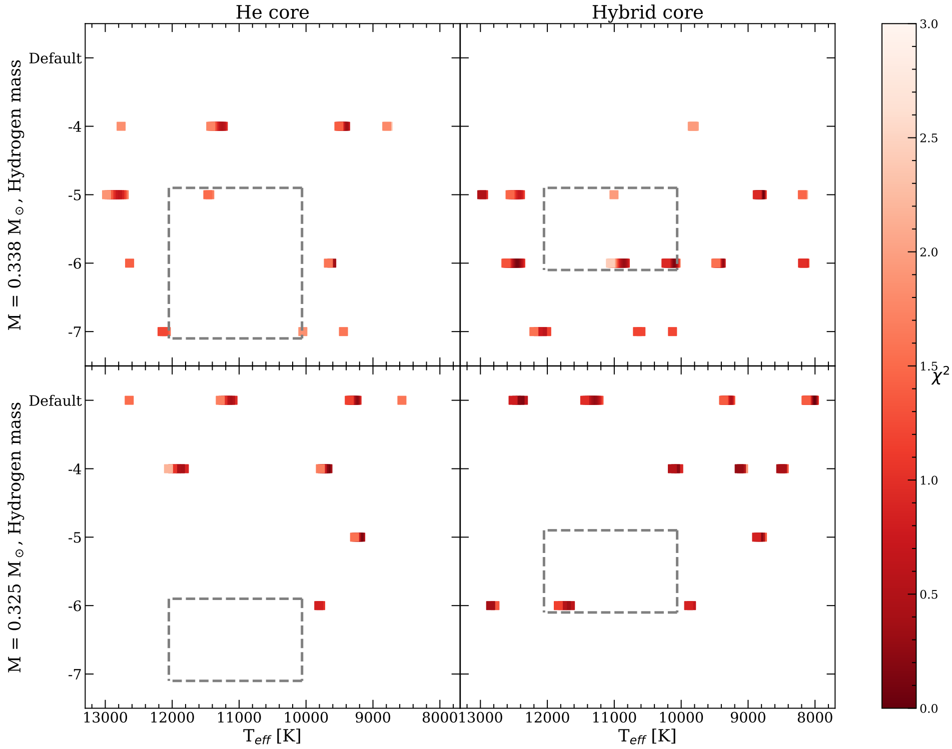

Figure 22 – The χ^2 (colour scale) as a function of the effective temperature and the mass of the hydrogen-envelope. Top (bottom) panels correspond to models with stellar mass 0.338 $M_\odot$ (0.325 $M_\odot$). Both helium-core (left panels) and hybrid-core (right panels) structure are considered. The dashed-line rectangle indicates the region of the $T_{\rm eff}$- Hydrogen envelope plane restricted by the observed determinations of radius and effective temperatures.

than that for model 1. Therefore, we can conclude that J1152+0248−V is a low-mass white dwarf star with a hybrid core, a thin hydrogen envelope, and a white dwarf mass of 0.338 $M_\odot$.

In Figure 23 we depict the radial eigenfunction y_1 as a function of the relative radius for the theoretical modes listed in Table 9. Each row corresponds to an asteroseismological model (1 and 4, from top to bottom), while each column corresponds to the theoretical period that fits each observed mode. The period, harmonic degree, and radial order of each theoretical mode are indicated on the top of the panel. Also, for reference, we show with dashed lines the mass fraction of hydrogen, helium, carbon, and oxygen. It is presented only solutions 1 and 4 given that solution 4 has a different mass than the others, which are almost identical to solution 1 in mass, effective temperature, and eigenfunction shape.

For all modes, the y_1 function shows significant amplitudes in the hydrogen envelope and is also sensitive to the position of the H/He chemical transition. For the theoretical

Table 9 – Asteroseismological models for J1152+0248−V. The effective temperature, stellar radius, stellar mass, hydrogen-envelope mass, and central composition are listed in columns 2, 3, 4, 5, and 6 respectively. We list the theoretical periods that better fit the observed periods in column 7, along with the values of ℓ and k, in columns 8 and 9. The value of the quality function χ^2 is listed in column 10.

#	$T_{\rm eff}$ [K]	$R/R_\odot$	$M_*/M_\odot$	$M_H/M_\odot$	X_C	$\Pi_{\rm th}$ [s]	ℓ	k	χ^2 [s]
1	10 917	0.0187	0.338	10^{-6}	C/O	1315.4	1	21	0.296
						1063.3	2	30	
						582.01	2	15	
2	10 904	0.0187	0.338	10^{-6}	C/O	1316.1	1	21	0.305
						1063.8	2	30	
						582.3	2	15	
3	10 929	0.0187	0.338	10^{-6}	C/O	1314.9	1	21	0.318
						1062.8	2	30	
						581.8	2	15	
4	11 717	0.0195	0.325	10^{-6}	C/O	1316.1	1	21	0.345
						1065.4	2	30	
						581.3	2	15	

modes corresponding to the fit of the mode with 1314 s, the y_1 shows significant amplitudes almost exclusively in the hydrogen envelope for all the models, making this particular mode sensitive to the hydrogen envelope mass. For the modes that fit the shortest detected period of 582.9 s, there is a marginal amplitude in the central region for all configurations. Finally, the mode with a period of 1069 s presents a higher sensitivity for 0.338 $M_\odot$ models as the amplitude is higher for solution 1 than for solution 4.

As seen in Figure 23, the observed modes seem to be very sensitive to the position of the H/He chemical transition, i.e., to the hydrogen envelope mass, which favors a thin-envelope configuration. However, note that all models fit the observed periods, given the large uncertainties. Further observations are needed to reduce the uncertainties in the observed pulsation periods.

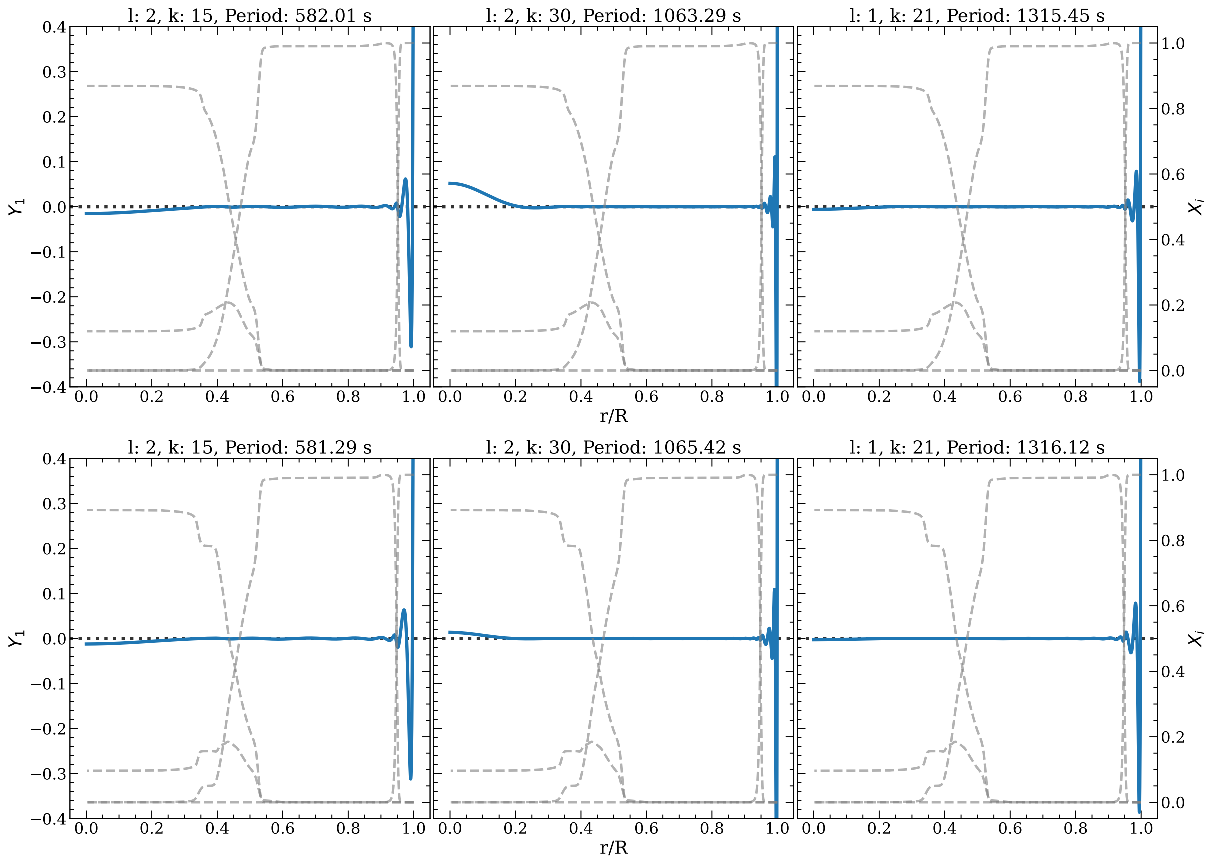

Figure 23 – The profile of the y_1 eigenfunction (blue line) as a function of the relative radius for the asteroseismological models presented in Table 9 (models 1 and 4, from top to bottom). Each row corresponds to the same model, while each column shows y_1 for each theoretical mode. The values of ℓ, k and the theoretical period are indicated on top of the panels. The chemical profile is depicted with dashed lines.

5 Conclusion

In this thesis, we performed an analysis of the pulsational properties of the variable low-mass white dwarf stars, a class of variable stars with 22 confirmed objects and stellar masses within the range of $0.30 \leq M/M_{\odot} \leq 0.45$ and photometric variability with periods between 200 and 1300 s. Throughout this work, we presented an observational, theoretical, and computational analysis of the properties of LMVs.

In chapter 3, we discussed the weighted mean period of LMVs and compared it with the same relation for ZZ Ceti stars. Although the Brunt-Väisälä frequency among the ZZ Ceti and LMV are similar, the linear relation for ZZ Ceti can not be extended for the LMVs. The formation channel of the LMVs has a direct impact on the core composition, stellar mass, and boundary of the H/He layer, which increases the dispersion in the period. More data and additional constraints are necessary in order to reduce scatter and to better calculate a relation between period, amplitude, and temperature. It also shows a list of 61 candidates that are observable from the south hemisphere and a discussion of the observation of 4 of those candidates, J2230-0023, J2058-0605, J1212-0123, and J1448+0713. The telescope properties, night of observations, light curves, and Fourier transform were presented and discussed. Unfortunately, the observed objects presented in this thesis do not show any periodicities within the detection limit and thus are classified as *Not Observed to Vary*. However, given the adverse weather conditions of the observing nights, follow-up observations with better weather conditions are necessary in order to discard additional periods.

The main results of this thesis were published in Romero et al. (2021) and also discussed in chapter 4, where fully binary evolutionary sequences for helium- and hybrid core low-mass white dwarfs with a stellar mass of 0.325 and 0.338 $M_{\odot}$ were calculated and used to perform an asteroseismological analysis and explore the inner chemical structure of the pulsating component in the J1152+0248 system.

In addition, to account for the uncertainty in the hydrogen envelope mass due to the evolution through a common envelope channel, white dwarf sequences with the same stellar mass but with a hydrogen envelope thinner than the canonical value obtained from stable mass-transfer were computed, i.e. 10^{-4} to 10^{-10}. Adiabatic pulsations were calculated for all these sequences, for effective temperatures in the range $13\,000$ K $\leq T_{\rm eff} \leq 8000$ K.

For the helium-core models, $\Delta\Pi_k$ shows a simple trapping cycle, characteristic of one-transition models. On the other hand, for hybrid-core models, the period spacing distribution is more complex due to the presence of the He/C/O transition. In both cases, the asymptotic period spacing and the mean period spacing increase with decreasing effective temperature and hydrogen envelope mass, in agreement with the results found for the ZZ Ceti stars.

For a given radial order k, the theoretical periods for the helium-core models are always larger than those for the hybrid-core models, for the same effective temperature, stellar mass, and hydrogen-envelope mass. This is a result of the dependence of the Brunt-Väisälä frequency with gravity $g \sim \mathrm{M/R}^2$, and the fact that hybrid-models are more compact at the cooling sequence, having a smaller radius for the same effective temperature than the helium-core model.

From a comparison between the observed and theoretical radius and effective temperature, the variable component of J1152+0248 must have a hydrogen envelope thinner than that predicted from stable-mass transfer binary evolution computations.

From the asteroseismological study, the best-fit model is characterized by an effective temperature of $T_{\rm eff} = 10\,917$ K, stellar mass of 0.338 $\mathrm{M}_\odot$, hydrogen mass of $\mathrm{M_H/M_\odot} = 10^{-6}$ and a hybrid-core composition. In particular, all local minima of χ^2 correspond to models with a hybrid core and a thin H envelope.

Further observations of J1152+0248−V are needed to reduce the uncertainties in the observed periods and to find additional pulsation periods, if any. This will improve the quality of the asteroseismological fit and allow the pattern of the forward period spacing to be used to determine the inner composition of low-mass white dwarf stars.

Bibliography

Aerts, C.; Christensen-Dalsgaard, J.; Kurtz, D. W. *Asteroseismology*. 1. ed. [S.l.]: Springer Netherlands, 2010. (Astronomy and Astrophysics Library). ISBN 1402051786,9781402051784. Cited 2 times on pages 40 and 46.

Ahn, C. P. et al. The Tenth Data Release of the Sloan Digital Sky Survey: First Spectroscopic Data from the SDSS-III Apache Point Observatory Galactic Evolution Experiment. *The Astrophysical Journal, Supplement*, v. 211, p. 17, abr. 2014. Cited on page 36.

Althaus, L. G. et al. New Chemical Profiles for the Asteroseismology of ZZ Ceti Stars. *The Astrophysical Journal*, v. 717, p. 897–907, jul. 2010. Cited on page 51.

Althaus, L. G. et al. Evolutionary and pulsational properties of white dwarf stars. *The Astronomy and Astrophysics Review*, v. 18, p. 471–566, out. 2010. Cited 3 times on pages 35, 36, and 46.

Althaus, L. G. et al. On the Formation of Hot DQ White Dwarfs. *The Astrophysical Journal Letter*, v. 693, p. L23–L26, mar. 2009. Cited on page 36.

Althaus, L. G.; Miller Bertolami, M. M.; Córsico, A. H. New evolutionary sequences for extremely low-mass white dwarfs. Homogeneous mass and age determinations and asteroseismic prospects. *Astronomy & Astrophysics*, v. 557, p. A19, set. 2013. Cited on page 37.

Auvergne, M. et al. The CoRoT satellite in flight: description and performance. , v. 506, n. 1, p. 411–424, out. 2009. Cited on page 46.

Battich, T. et al. Pulsational instabilities driven by the $\in$ mechanism in hot pre-horizontal branch stars. I. The hot-flasher scenario. , v. 614, p. A136, jun. 2018. Cited on page 45.

Bell, K. J. et al. Pruning The ELM Survey: Characterizing Candidate Low-mass White Dwarfs through Photometric Variability. , v. 835, n. 2, p. 180, fev. 2017. Cited on page 50.

Bell, K. J. et al. KIC 4552982: Outbursts and Asteroseismology from the Longest Pseudo-continuous Light Curve of a ZZ Ceti. , v. 809, n. 1, p. 14, ago. 2015. Cited on page 50.

Bell, K. J. et al. The McDonald Observatory search for pulsating sdA stars. Asteroseismic support for multiple populations. , v. 617, p. A6, set. 2018. Cited on page 50.

Bergeron, P. et al. On the Purity of the ZZ Ceti Instability Strip: Discovery of More Pulsating DA White Dwarfs on the Basis of Optical Spectroscopy. *The Astrophysical Journal*, v. 600, n. 1, p. 404–408, jan. 2004. Cited 2 times on pages 60 and 61.

Bischoff-Kim, A.; Montgomery, M. H.; Winget, D. E. Strong Limits on the DFSZ Axion Mass with G117-B15A. , v. 675, n. 2, p. 1512–1517, mar. 2008. Cited on page 46.

Bognar, Z.; Sodor, A. White Dwarf Period Tables I. Pulsators with hydrogen-dominated atmospheres. *Information Bulletin on Variable Stars*, v. 6184, p. 1, set. 2016. Cited 3 times on pages 48, 50, and 59.

Borucki, W. J. et al. Kepler Planet-Detection Mission: Introduction and First Results. *Science*, v. 327, n. 5968, p. 977, fev. 2010. Cited on page 46.

Brassard, P. et al. Adiabatic Properties of Pulsating DA White Dwarfs. IV. an Extensive Survey of the Period Structure of Evolutionary Models. , v. 81, p. 747, ago. 1992. Cited on page 76.

Brooks, J. et al. Carbon Shell or Core Ignitions in White Dwarfs Accreting from Helium Stars. *The Astrophysical Journal*, v. 821, p. 28, abr. 2016. Cited on page 53.

Brooks, J. et al. Accretion-induced Collapse from Helium Star + White Dwarf Binaries. *The Astrophysical Journal*, v. 843, p. 151, jul. 2017. Cited on page 53.

Brooks, J. et al. Convection Destroys the Core/Mantle Structure in Hybrid C/O/Ne White Dwarfs. *The Astrophysical Journall*, v. 834, p. L9, jan. 2017. Cited on page 53.

Brown, J. M. et al. The Binary Fraction of Low-mass White Dwarfs. , v. 730, n. 2, p. 67, abr. 2011. Cited on page 38.

Brown, W. R. et al. The ELM Survey. VII. Orbital Properties of Low-Mass White Dwarf Binaries. , v. 818, n. 2, p. 155, fev. 2016. Cited on page 38.

Brown, W. R. et al. The ELM Survey. I. A Complete Sample of Extremely Low-mass White Dwarfs. , v. 723, n. 2, p. 1072–1081, nov. 2010. Cited on page 38.

Brown, W. R. et al. The ELM Survey. VIII. Ninety-eight Double White Dwarf Binaries. , v. 889, n. 1, p. 49, jan. 2020. Cited on page 38.

Buysschaert, B. et al. Forward seismic modeling of the pulsating magnetic B-type star HD 43317. , v. 616, p. A148, ago. 2018. Cited on page 56.

Calcaferro, L. M.; Córsico, A. H.; Althaus, L. G. Asteroseismology of the GW Virginis stars SDSS J0349-0059 and VV 47. , v. 589, p. A40, maio 2016. Cited 2 times on pages 46 and 51.

Carroll, B. W.; Ostlie, D. A. *An Introduction to Modern Astrophysics*. 2. ed. [S.l.]: Pearson, 2014. ISBN 1-292-02293-0, 978-1-292-02293-2. Cited 3 times on pages 29, 32, and 33.

Cassisi, S. et al. Updated Electron-Conduction Opacities: The Impact on Low-Mass Stellar Models. , v. 661, n. 2, p. 1094–1104, jun. 2007. Cited on page 55.

Castanheira, B. G.; Kepler, S. O. Seismological studies of ZZ Ceti stars - I. The model grid and the application to individual stars. , v. 385, n. 1, p. 430–444, mar. 2008. Cited on page 51.

Castanheira, B. G.; Kepler, S. O. Seismological studies of ZZ Ceti stars - II. Application to the ZZ Ceti class. , v. 396, n. 3, p. 1709–1731, jul. 2009. Cited on page 46.

Catelan, M.; Smith, H. A. *Pulsating Stars*. [S.l.: s.n.], 2015. Cited on page 46.

Chaboyer, B.; Zahn, J. P. Effect of horizontal turbulent diffusion on transport by meridional circulation. , v. 253, p. 173–177, jan. 1992. Cited on page 56.

Chandrasekhar, S. The Maximum Mass of Ideal White Dwarfs. *The Astrophysical Journal*, v. 74, p. 81, jul. 1931. Cited on page 35.

Chen, M. C. et al. The dependence of the evolution of Type Ia SN progenitors on the C-burning rate uncertainty and parameters of convective boundary mixing. *Monthly Notices of the Royal Astronomical Society*, v. 440, p. 1274–1280, maio 2014. Cited on page 53.

Choi, J. et al. Mesa Isochrones and Stellar Tracks (MIST). I. Solar-scaled Models. *The Astrophysical Journal*, v. 823, p. 102, jun. 2016. Cited on page 53.

Clemens, J. C. The pulsation properties of the DA white dwarf variables. *Baltic Astronomy*, v. 2, p. 407–434, jan. 1993. Cited on page 59.

Compton, D. L. et al. Surface correction of main-sequence solar-like oscillators with the Kepler LEGACY sample. , v. 479, n. 4, p. 4416–4431, out. 2018. Cited on page 56.

Córsico, A. H. et al. An independent limit on the axion mass from the variable white dwarf star r548. *Journal of Cosmology and Astroparticle Physics*, IOP Publishing, v. 2012, n. 12, p. 010–010, dec 2012. Disponível em: <https://doi.org/10.1088/1475-7516/2012/12/010>. Cited 2 times on pages 46 and 50.

Córsico, A. H.; Althaus, L. G. Asteroseismic inferences on GW Virginis variable stars in the frame of new PG 1159 evolutionary models. *Astronomy and Astrophysics*, v. 454, p. 863–881, ago. 2006. Cited on page 46.

Córsico, A. H.; Althaus, L. G. Pulsating low-mass white dwarfs in the frame of new evolutionary sequences. I. Adiabatic properties. , v. 569, p. A106, Sep 2014. Cited 2 times on pages 50 and 76.

Córsico, A. H.; Althaus, L. G. Pulsating low-mass white dwarfs in the frame of new evolutionary sequences. II. Nonadiabatic analysis. , v. 585, p. A1, Jan 2016. Cited on page 50.

Córsico, A. H. et al. Pulsating white dwarfs: new insights. , v. 27, n. 1, p. 7, set. 2019. Cited 3 times on pages 46, 48, and 50.

Córsico, A. H. et al. Pulsating low-mass white dwarfs in the frame of new evolutionary sequences. III. The pre-ELM white dwarf instability strip. , v. 588, p. A74, abr. 2016. Cited on page 48.

Córsico, A. H. et al. The seismic properties of low-mass He-core white dwarf stars. , v. 547, p. A96, nov. 2012. Cited on page 50.

Cowling, T. G.; Newing, R. A. The Oscillations of a Rotating Star. , v. 109, p. 149, jan. 1949. Cited on page 43.

Cox, J. P.; Giuli, R. T. *Principles of stellar structure* . [S.l.: s.n.], 1968. Cited on page 29.

Denissenkov, P. A. et al. The C-flame Quenching by Convective Boundary Mixing in Super-AGB Stars and the Formation of Hybrid C/O/Ne White Dwarfs and SN Progenitors. *The Astrophysical Journal*, v. 772, p. 37, jul. 2013. Cited on page 53.

Dhillon, V. et al. First light with HiPERCAM on the GTC. In: Evans, C. J.; Simard, L.; Takami, H. (Ed.). *Ground-based and Airborne Instrumentation for Astronomy VII.* [S.l.: s.n.], 2018. (Society of Photo-Optical Instrumentation Engineers (SPIE) Conference Series, v. 10702), p. 107020L. Cited on page 69.

Doherty, C. L. et al. Super- and massive AGB stars - IV. Final fates - initial-to-final mass relation. *Monthly Notices of the Royal Astronomical Society*, v. 446, p. 2599–2612, jan. 2015. Cited on page 35.

Dolez, N.; Vauclair, G. Gravity modes instability in DA white dwarfs. , v. 102, p. 375–385, out. 1981. Cited on page 44.

Dotter, A. MESA Isochrones and Stellar Tracks (MIST) 0: Methods for the Construction of Stellar Isochrones. *The Astrophysical Journal, Supplement*, v. 222, p. 8, jan. 2016. Cited on page 53.

Dufour, P. et al. Hot DQ White Dwarfs: Something Different. *The Astrophysical Journal*, v. 683, p. 978–989, ago. 2008. Cited on page 36.

Dufour, P. et al. White dwarf stars with carbon atmospheres. *Nature*, v. 450, p. 522–524, nov. 2007. Cited on page 36.

Edelmann, P. V. F. et al. Three-dimensional Simulations of Massive Stars. I. Wave Generation and Propagation. , v. 876, n. 1, p. 4, maio 2019. Cited on page 56.

Eggleton, P. *Evolutionary processes in binary and multiple stars*. [S.l.]: Cambridge University Press, 2006. (Cambridge astrophysics series 40). ISBN 0521855578,9780521855570,9780511226298. Cited on page 29.

Eggleton, P. P. Aproximations to the radii of Roche lobes. , v. 268, p. 368–369, maio 1983. Cited on page 34.

Farmer, R.; Fields, C. E.; Timmes, F. X. On Carbon Burning in Super Asymptotic Giant Branch Stars. *The Astrophysical Journal*, v. 807, p. 184, jul. 2015. Cited on page 53.

Ferguson, J. W. et al. Low-Temperature Opacities. , v. 623, n. 1, p. 585–596, abr. 2005. Cited on page 55.

Fontaine, G.; Brassard, P. The Pulsating White Dwarf Stars. , v. 120, n. 872, p. 1043, out. 2008. Cited 3 times on pages 35, 46, and 48.

Fuchs, J. T. *Fundamental Properties of White Dwarfs Alone and in Binaries*. Tese (Doutorado) — The University of North Carolina at Chapel Hill, jan. 2017. Cited on page 50.

Gabriel, M.; Noels, A. Stability of a 30 M Star towards g+ Modes of High Spherical Harmonic Values. , v. 53, p. 149, nov. 1976. Cited on page 56.

Gaia Collaboration et al. Gaia Data Release 1. Open cluster astrometry: performance, limitations, and future prospects. , v. 601, p. A19, maio 2017. Cited on page 46.

García-Berro, E.; Isern, J.; Hernanz, M. The cooling of oxygen-neon white dwarfs. *Monthly Notices of the Royal Astronomical Society*, v. 289, p. 973–978, ago. 1997. Cited on page 35.

Gianninas, A.; Bergeron, P.; Fontaine, G. Toward an Empirical Determination of the ZZ Ceti Instability Strip. *The Astrophysical Journal*, v. 631, n. 2, p. 1100–1112, out. 2005. Cited 2 times on pages 60 and 61.

Goldstein, J.; Townsend, R. H. D. The Contour Method: a New Approach to Finding Modes of Nonadiabatic Stellar Pulsations. , v. 899, n. 2, p. 116, ago. 2020. Cited on page 56.

Green, R. F.; Schmidt, M.; Liebert, J. The Palomar-Green Catalog of Ultraviolet-Excess Stellar Objects. , v. 61, p. 305, jun. 1986. Cited on page 38.

Grevesse, N.; Sauval, A. J. Standard Solar Composition. , v. 85, p. 161–174, maio 1998. Cited on page 55.

Guo, J. et al. White dwarfs identified in LAMOST DR 2. , v. 454, n. 3, p. 2787–2797, dez. 2015. Cited on page 59.

Hall, W.; Castanheira, B. G.; Bischoff-Kim, A. Seismological Studies of Pulsating DA White Dwarfs Observed with the Kepler Space Telescope and K2 Campaigns 1-8. , v. 948, n. 2, p. 74, maio 2023. Cited on page 51.

Hallakoun, N. et al. SDSS J1152+0248: an eclipsing double white dwarf from the Kepler K2 campaign. , v. 458, n. 1, p. 845–854, maio 2016. Cited 2 times on pages 52 and 69.

Handler, G. et al. Amplitude and frequency variability of the pulsating DB white dwarf stars KUV 05134+2605 and PG 1654+160 observed with the Whole Earth Telescope. , v. 340, n. 3, p. 1031–1038, abr. 2003. Cited on page 51.

Heger, A.; Langer, N.; Woosley, S. E. Presupernova Evolution of Rotating Massive Stars. I. Numerical Method and Evolution of the Internal Stellar Structure. , v. 528, n. 1, p. 368–396, jan. 2000. Cited on page 56.

Henyey, L.; Vardya, M. S.; Bodenheimer, P. Studies in Stellar Evolution. III. The Calculation of Model Envelopes. , v. 142, p. 841, out. 1965. Cited on page 55.

Henyey, L. G. et al. A Method for Automatic Computation of Stellar Evolution. *The Astrophysical Journal*, v. 129, p. 628, maio 1959. Cited on page 53.

Hermes, J. J. et al. White Dwarf Rotation as a Function of Mass and a Dichotomy of Mode Line Widths: Kepler Observations of 27 Pulsating DA White Dwarfs through K2 Campaign 8. , v. 232, n. 2, p. 23, out. 2017. Cited on page 59.

Hermes, J. J. et al. Discovery of an Ultramassive Pulsating White Dwarf. *The Astrophysical Journal Letters*, v. 771, p. L2, jul. 2013. Cited on page 50.

Hermes, J. J. et al. SDSS J184037.78+642312.3: The First Pulsating Extremely Low Mass White Dwarf. , v. 750, n. 2, p. L28, maio 2012. Cited 2 times on pages 48 and 50.

Hilditch, R. W. *An Introduction to Close Binary Stars*. 1. ed. [S.l.]: Cambridge University Press, 2001. (Cambridge Astrophysics). ISBN 0521241065,9780521241069. Cited on page 29.

Iben I., J.; Tutukov, A. V. On the evolution of close binaries with components of initial mass between 3 M and 12 M. , v. 58, p. 661–710, Aug 1985. Cited on page 55.

Iben JR., I. et al. On the evolution of those nuclei of planetary nebulae that experience a final helium shell flash. *The Astrophysical Journal*, v. 264, p. 605–612, jan. 1983. Cited on page 35.

Iglesias, C. A.; Rogers, F. J. Radiative Opacities for Carbon- and Oxygen-rich Mixtures. , v. 412, p. 752, ago. 1993. Cited on page 55.

Iglesias, C. A.; Rogers, F. J. Updated Opal Opacities. *The Astrophysical Journal*, v. 464, p. 943, jun. 1996. Cited on page 55.

Isern, J. et al. Axions and White Dwarfs. *ArXiv e-prints*, out. 2010. Cited on page 46.

Isern, J.; Hernanz, M.; Garcia-Berro, E. Axion Cooling of White Dwarfs. , v. 392, p. L23, jun. 1992. Cited on page 46.

Istrate, A. G.; et. al. . In preparation. Cited 2 times on pages 54 and 70.

Istrate, A. G.; Fontaine, G.; Heuser, C. A Model of the Pulsating Extremely Low-mass White Dwarf Precursor WASP 0247-25B. *The Astrophysical Journal*, v. 847, p. 130, out. 2017. Cited on page 53.

Istrate, A. G. et al. Models of low-mass helium white dwarfs including gravitational settling, thermal and chemical diffusion, and rotational mixing. *Astronomy & Astrophysics*, v. 595, p. A35, out. 2016. Cited 4 times on pages 37, 48, 53, and 62.

Istrate, A. G. et al. The timescale of low-mass proto-helium white dwarf evolution. *Astronomy & Astrophysics*, v. 571, p. L3, nov. 2014. Cited 2 times on pages 37 and 49.

Itoh, N.; Kohyama, Y.; Takeuchi, H. Viscosity of Dense Matter. , v. 317, p. 733, jun. 1987. Cited on page 56.

Jones, P. W. et al. On the Possibility of Detecting Weak Magnetic Fields in Variable White Dwarfs. , v. 336, p. 403, jan. 1989. Cited on page 44.

Jones, S. et al. Advanced Burning Stages and Fate of 8-10 $M_\odot$ Stars. *The Astrophysical Journal*, v. 772, p. 150, ago. 2013. Cited on page 53.

Kanaan, A.; Kepler, S. O.; Winget, D. E. The ZZ Ceti red edge. *Astronomy and Astrophysics*, v. 389, p. 896–903, jul. 2002. Cited on page 59.

Kanaan, A. et al. Whole Earth Telescope observations of BPM 37093: A seismological test of crystallization theory in white dwarfs. , v. 432, n. 1, p. 219–224, mar. 2005. Cited on page 46.

Kawaler, S. D. Angular Momentum Loss in Low-Mass Stars. , v. 333, p. 236, out. 1988. Cited on page 56.

Kawaler, S. D. et al. Whole Earth Telescope Observations and Seismological Analysis of the Pre–White Dwarf PG 2131+066. , v. 450, p. 350, set. 1995. Cited on page 51.

Kepler, S. O. Whole earth telescope data analysis. *Baltic Astronomy*, v. 2, p. 515–529, jan. 1993. Cited on page 65.

Kepler, S. O. et al. White dwarf mass distribution in the SDSS. *Monthly Notices of the Royal Astronomical Society*, v. 375, p. 1315–1324, mar. 2007. Cited on page 37.

Kepler, S. O. et al. New white dwarf stars in the Sloan Digital Sky Survey Data Release 10. *Monthly Notices of the Royal Astronomical Society*, v. 446, p. 4078–4087, fev. 2015. Cited on page 37.

Kepler, S. O. et al. New white dwarf and subdwarf stars in the Sloan Digital Sky Survey Data Release 12. *Monthly Notices of the Royal Astronomical Society*, v. 455, p. 3413–3423, fev. 2016. Cited 2 times on pages 36 and 37.

Kepler, S. O. et al. White dwarf and subdwarf stars in the Sloan Digital Sky Survey Data Release 14. , v. 486, n. 2, p. 2169–2183, jun. 2019. Cited on page 61.

Kepler, S. O.; Saraiva, M. A. *ASTRONOMIA E ASTROFÍSICA*. 4. ed. [S.l.]: Livraria da Física, 2017. ISBN 9788578614850. Cited on page 29.

Kilic, M. et al. A refined search for pulsations in white dwarf companions to millisecond pulsars. , v. 479, n. 1, p. 1267–1272, set. 2018. Cited on page 50.

Kilic, M. et al. PSR J1738+0333: the first millisecond pulsar + pulsating white dwarf binary. , v. 446, p. L26–L30, jan. 2015. Cited on page 50.

Kilic, M.; Stanek, K. Z.; Pinsonneault, M. H. The Future Is Now: The Formation of Single Low-Mass White Dwarfs in the Solar Neighborhood. , v. 671, n. 1, p. 761–766, dez. 2007. Cited 2 times on pages 37 and 49.

Kleinman, S. J. et al. SDSS DR7 White Dwarf Catalog. *The Astrophysical Journal, Supplement*, v. 204, p. 5, jan. 2013. Cited 2 times on pages 35 and 37.

Kupfer, T. et al. A New Class of Large-amplitude Radial-mode Hot Subdwarf Pulsators. , v. 878, n. 2, p. L35, jun. 2019. Cited 2 times on pages 48 and 56.

Kurtz, D. W. et al. A search for a new class of pulsating DA white dwarf stars in the DB gap. , v. 389, n. 4, p. 1771–1779, out. 2008. Cited on page 47.

Landolt, A. U. A New Short-Period Blue Variable. , v. 153, p. 151, jul. 1968. Cited on page 46.

Langer, N. Presupernova Evolution of Massive Single and Binary Stars. *Annual Review of Astronomu & Astrophysics*, v. 50, p. 107–164, set. 2012. Cited on page 35.

Langer, N.; Fricke, K. J.; Sugimoto, D. Semiconvective diffusion and energy transport. *Astronomy & Astrophysics*, v. 126, p. 207, set. 1983. Cited on page 55.

Lauffer, G. R.; Romero, A. D.; Kepler, S. O. New full evolutionary sequences of H- and He-atmosphere massive white dwarf stars using MESA. , v. 480, n. 2, p. 1547–1562, out. 2018. Cited 2 times on pages 35 and 53.

Ledoux, P. The Nonradial Oscillations of Gaseous Stars and the Problem of Beta Canis Majoris. , v. 114, p. 373, nov. 1951. Cited on page 43.

Lenz, P.; Breger, M. Period04: A software package to extract multiple frequencies from real data. In: Zverko, J. et al. (Ed.). *The A-Star Puzzle*. [S.l.: s.n.], 2004. v. 224, p. 786–790. Cited on page 65.

Liebert, J.; Fontaine, G.; Wesemael, F. The luminosity function and the evolution of surface abundances of white dwarfs. *The Astrophysical Journal*, v. 58, p. 17–31, 1987. Cited on page 35.

Liebert, J. et al. Temperatures for hot and pulsating DB white dwarfs obtained with the IUE Observatory. *The Astrophysical Journal*, v. 309, p. 241–252, out. 1986. Cited on page 35.

Maciel, W. *Introduction to Stellar Structure*. 1. ed. [S.l.]: Springer International Publishing, 2016. (Springer Praxis Books). ISBN 978-3-319-16141-9,978-3-319-16142-6. Cited on page 29.

Magnus, W. On the exponential solution of differential equations for a linear operator. *Commun. Pure Appl. Math.*, v. 7, n. 4, p. 649–673, nov. 1954. Cited on page 56.

Maxted, P. F. L. et al. Multi-periodic pulsations of a stripped red-giant star in an eclipsing binary system. , v. 498, n. 7455, p. 463–465, jun. 2013. Cited on page 48.

McGraw, J. T. *The ZZ Ceti Stars - a New Class of Pulsating White Dwarfs*. Tese (Doutorado) — Texas Univ., Austin., jan. 1977. Cited on page 47.

McGraw, J. T. The period structure of the ZZ Ceti variables. In: *Current Problems in Stellar Pulsation Instabilities*. [S.l.: s.n.], 1980. p. 501–512. Cited on page 59.

McGraw, J. T. et al. PG1159-035: A new, hot, non-DA pulsating degenerate. In: van Horn, H. M.; Weidemann, V.; Savedoff, M. P. (Ed.). *IAU Colloq. 53: White Dwarfs and Variable Degenerate Stars*. [S.l.: s.n.], 1979. p. 377–381. Cited 2 times on pages 35 and 47.

Montgomery, M. H. A New Technique for Probing Convection in Pulsating White Dwarf Stars. , v. 633, n. 2, p. 1142–1149, nov. 2005. Cited on page 46.

Montgomery, M. H. et al. SDSS J142625.71+575218.3: A Prototype for a New Class of Variable White Dwarf. , v. 678, n. 1, p. L51, maio 2008. Cited on page 47.

Montgomery, M. H.; Winget, D. E. The Effect of Crystallization on the Pulsations of White Dwarf Stars. , v. 526, n. 2, p. 976–990, dez. 1999. Cited on page 46.

Moravveji, E. The impact of enhanced iron opacity on massive star pulsations: updated instability strips. , v. 455, n. 1, p. L67–L71, jan. 2016. Cited on page 56.

Mukadam, A. S. et al. Ensemble Characteristics of the ZZ Ceti Stars. *The Astrophysical Journal*, v. 640, n. 2, p. 956–965, abr. 2006. Cited 3 times on pages 59, 60, and 61.

Murphy, S. J. et al. A precise asteroseismic age and metallicity for HD 139614: a pre-main-sequence star with a protoplanetary disc in Upper Centaurus-Lupus. , v. 502, n. 2, p. 1633–1646, abr. 2021. Cited on page 56.

Nather, R. E. et al. The Whole Earth Telescope: A New Astronomical Instrument. , v. 361, p. 309, set. 1990. Cited on page 45.

Panei, J. A. et al. Full evolution of low-mass white dwarfs with helium and oxygen cores. , v. 382, n. 2, p. 779–792, dez. 2007. Cited 2 times on pages 37 and 49.

Parsons, S. G. et al. A pulsating white dwarf in an eclipsing binary. *Nature Astronomy*, v. 4, p. 690–696, mar. 2020. Cited 8 times on pages 48, 51, 62, 69, 70, 72, 77, and 78.

Paxton, B. et al. Modules for Experiments in Stellar Astrophysics (MESA). *The Astrophysical Journal, Supplement*, v. 192, p. 3, jan. 2011. Cited 2 times on pages 53 and 55.

Paxton, B. et al. Modules for Experiments in Stellar Astrophysics (MESA): Planets, Oscillations, Rotation, and Massive Stars. *The Astrophysical Journal, Supplement*, v. 208, p. 4, set. 2013. Cited on page 53.

Paxton, B. et al. Modules for Experiments in Stellar Astrophysics (MESA): Binaries, Pulsations, and Explosions. *The Astrophysical Journal, Supplement*, v. 220, p. 15, set. 2015. Cited on page 53.

Paxton, B. et al. Modules for Experiments in Stellar Astrophysics (MESA): Convective Boundaries, Element Diffusion, and Massive Star Explosions. *The Astrophysical Journal, Supplement*, v. 234, p. 34, fev. 2018. Cited on page 53.

Pelisoli, I. et al. The sdA problem - III. New extremely low-mass white dwarfs and their precursors from Gaia astrometry. , v. 482, n. 3, p. 3831–3842, jan. 2019. Cited on page 50.

Pelisoli, I.; Vos, J. Gaia Data Release 2 catalogue of extremely low-mass white dwarf candidates. , v. 488, n. 2, p. 2892–2903, set. 2019. Cited 2 times on pages 37 and 49.

Perryman, M. A. C. et al. The Hipparcos Catalogue. , v. 500, p. 501–504, jul. 1997. Cited on page 46.

Pietrukowicz, P. et al. Blue large-amplitude pulsators as a new class of variable stars. *Nature Astronomy*, v. 1, p. 0166, ago. 2017. Cited on page 48.

Pignatari, M. et al. NuGrid Stellar Data Set. I.Stellar Yields from H to Bi for Stars with Metallicities $Z = 0.02$ and $Z = 0.01$. *The Astrophysical Journal, Supplement*, v. 225, p. 24, ago. 2016. Cited on page 53.

Poelarends, A. J. T. et al. The Supernova Channel of Super-AGB Stars. *The Astrophysical Journal*, v. 675, p. 614–625, mar. 2008. Cited on page 35.

Prada Moroni, P. G.; Straniero, O. Very low-mass white dwarfs with a C-O core. , v. 507, n. 3, p. 1575–1583, dez. 2009. Cited on page 37.

Rebassa-Mansergas, A. et al. The mass function of hydrogen-rich white dwarfs: robust observational evidence for a distinctive high-mass excess near 1 $M_{\odot}$. *Monthly Notices of the Royal Astronomical Society*, v. 452, p. 1637–1642, set. 2015. Cited on page 37.

Ricker, G. R. et al. Transiting Exoplanet Survey Satellite (TESS). *Journal of Astronomical Telescopes, Instruments, and Systems*, v. 1, p. 014003, jan. 2015. Cited on page 46.

Ritter, C. et al. NuGrid Stellar Data Set. II. Stellar Yields from H to Bi for Stellar Models with Mzams = 1 to $25 M_{\odot}$ and $Z = 0.0001$ to 0.02. *ArXiv e-prints*, set. 2017. Cited on page 53.

Robinson, E. L. The Observational Properties of the ZZ Ceti Stars. In: van Horn, H. M.; Weidemann, V.; Savedoff, M. P. (Ed.). *IAU Colloq. 53: White Dwarfs and Variable Degenerate Stars*. [S.l.: s.n.], 1979. p. 343. Cited on page 59.

Robinson, E. L. The pulsating white dwarfs. In: *Current Problems in Stellar Pulsation Instabilities*. [S.l.: s.n.], 1980. p. 423–451. Cited on page 59.

Robinson, E. L.; Kepler, S. O.; Nather, R. E. Multicolor variations of the ZZ CET stars. , v. 259, p. 219–231, ago. 1982. Cited on page 47.

Rogers, F. J.; Nayfonov, A. Updated and Expanded OPAL Equation-of-State Tables: Implications for Helioseismology. *The Astrophysical Journal*, v. 576, p. 1064–1074, set. 2002. Cited on page 21.

Rohrmann, R. D. et al. Outer boundary conditions for evolving cool white dwarfs. , v. 546, p. A119, out. 2012. Cited on page 55.

Romero, A. D. et al. Ground-based observation of ZZ Ceti stars and the discovery of four new variables. , v. 490, n. 2, p. 1803–1820, dez. 2019. Cited on page 48.

Romero, A. D. et al. Pulsation in the white dwarf HE 1017-1352: confirmation of the class of hot DAV stars. , v. 497, n. 1, p. L24–L29, set. 2020. Cited on page 47.

Romero, A. D.; Campos, F.; Kepler, S. O. The age-metallicity dependence for white dwarfs stars arXiv : 1504 . 03945v1 [astro-ph . SR] 15 Apr 2015. v. 000, n. April, apr 2015. Disponível em: <http://arxiv.org/abs/1504.03945http://dx.doi.org/10.1093/mnras/stv848>. Cited 3 times on pages 48, 51, and 62.

Romero, A. D. et al. Toward ensemble asteroseismology of ZZ Ceti stars with fully evolutionary models. *Monthly Notices of the Royal Astronomical Society*, v. 420, p. 1462–1480, fev. 2012. Cited 3 times on pages 46, 61, and 74.

Romero, A. D. et al. On the evolutionary status and pulsations of the recently discovered blue large-amplitude pulsators (BLAPs). , v. 477, n. 1, p. L30–L34, jun. 2018. Cited on page 48.

Romero, A. D. et al. Probing the Structure of Kepler ZZ Ceti Stars with Full Evolutionary Models-based Asteroseismology. , v. 851, n. 1, p. 60, dez. 2017. Cited 2 times on pages 46 and 51.

Romero, A. D. et al. Asteroseismological Study of Massive ZZ Ceti Stars with Fully Evolutionary Models. *The Astrophysical Journal*, v. 779, n. 1, p. 58, oct 2013. ISSN 0004-637X. Disponível em: <http://arxiv.org/abs/1310.4137>. Cited 3 times on pages 46, 51, and 61.

Romero, A. D. et al. Discovery of 74 new bright ZZ Ceti stars in the first three years of TESS. , v. 511, n. 2, p. 1574–1590, abr. 2022. Cited on page 59.

Romero, A. D. et al. Uncovering the chemical structure of the pulsating low-mass white dwarf SDSS J115219.99+024814.4. , v. 510, n. 1, p. 858–869, dez. 2021. Disponível em: <https://doi.org/10.1093/mnras/stab3487>. Cited 3 times on pages 49, 69, and 83.

Rowan, D. M. et al. Detections and constraints on white dwarf variability from time-series GALEX observations. , v. 486, n. 4, p. 4574–4589, jul. 2019. Cited 2 times on pages 50 and 59.

Salpeter, E. E. The Luminosity Function and Stellar Evolution. *Astrophysical Journal*, v. 121, p. 161, jan. 1955. Cited 2 times on pages 31 and 35.

Schoenberner, D. Asymptotic giant branch evolution with steady mass loss. *Astronomy & Astrophysics*, v. 79, p. 108–114, out. 1979. Cited on page 35.

Schwab, J.; Bildsten, L.; Quataert, E. The importance of Urca-process cooling in accreting ONe white dwarfs. *Monthly Notices of the Royal Astronomical Society*, v. 472, p. 3390–3406, dez. 2017. Cited on page 53.

Shibahashi, H. The DB gap and pulsations of white dwarfs. In: Alecian, G.; Richard, O.; Vauclair, S. (Ed.). *EAS Publications Series*. [S.l.: s.n.], 2005. (EAS Publications Series, v. 17), p. 143–148. Cited on page 47.

Siess, L. Evolution of massive AGB stars. III. the thermally pulsing super-AGB phase. *Astronomy & Astrophysics*, v. 512, p. A10, mar. 2010. Cited on page 35.

Steinfadt, J. D. R.; Bildsten, L.; Arras, P. Pulsations in Hydrogen Burning Low-mass Helium White Dwarfs. , v. 718, n. 1, p. 441–445, jul. 2010. Cited on page 50.

Stetson, P. B. DAOPHOT: A Computer Program for Crowded-Field Stellar Photometry. , v. 99, p. 191, mar. 1987. Cited on page 64.

Su, J. et al. New ZZ Ceti Stars from the LAMOST Survey. , v. 847, n. 1, p. 34, set. 2017. Cited 2 times on pages 50 and 59.

Sun, M.; Arras, P. Formation of Extremely Low-mass White Dwarfs Binaries. *ArXiv e-prints*, mar. 2017. Cited on page 53.

Sun, M.; Townsend, R. H.; Guo, Z. GYRE-tides: a new open-source code to model stellar tides. In: *American Astronomical Society Meeting Abstracts*. [S.l.: s.n.], 2021. (American Astronomical Society Meeting Abstracts, v. 53), p. 438.04. Cited on page 56.

Tassoul, M. Asymptotic approximations for stellar nonradial pulsations. , v. 43, p. 469–490, ago. 1980. Cited on page 42.

Tassoul, M.; Fontaine, G.; Winget, D. E. Evolutionary Models for Pulsation Studies of White Dwarfs. , v. 72, p. 335, fev. 1990. Cited 2 times on pages 51 and 74.

Tassoul, M.; Tassoul, J. L. Asymptotic Approximations for Stellar Pulsations. , v. 153, p. 127, jul. 1968. Cited on page 42.

Thoul, A. A.; Bahcall, J. N.; Loeb, A. Element diffusion in the solar interior. *The Astrophysical Journal*, v. 421, p. 828–842, fev. 1994. Cited on page 55.

Timmes, F. X.; Swesty, F. D. The Accuracy, Consistency, and Speed of an Electron-Positron Equation of State Based on Table Interpolation of the Helmholtz Free Energy. *The Astrophysical Journal, Supplement*, v. 126, p. 501–516, fev. 2000. Cited on page 21.

Tody, D. The IRAF Data Reduction and Analysis System. In: Crawford, D. L. (Ed.). *Instrumentation in astronomy VI*. [S.l.: s.n.], 1986. (Society of Photo-Optical Instrumentation Engineers (SPIE) Conference Series, v. 627), p. 733. Cited on page 64.

Tody, D. IRAF in the Nineties. In: Hanisch, R. J.; Brissenden, R. J. V.; Barnes, J. (Ed.). *Astronomical Data Analysis Software and Systems II*. [S.l.: s.n.], 1993. (Astronomical Society of the Pacific Conference Series, v. 52), p. 173. Cited on page 64.

Townsend, R. H. D.; Goldstein, J.; Zweibel, E. G. Angular momentum transport by heat-driven g-modes in slowly pulsating B stars. , v. 475, n. 1, p. 879–893, mar. 2018. Cited on page 56.

Townsend, R. H. D.; Goldstein, J.; Zweibel, E. G. Angular momentum transport by heat-driven g-modes in slowly pulsating B stars. , v. 475, n. 1, p. 879–893, mar. 2018. Cited on page 56.

Townsend, R. H. D.; Teitler, S. A. GYRE: an open-source stellar oscillation code based on a new Magnus Multiple Shooting scheme. , v. 435, n. 4, p. 3406–3418, nov. 2013. Cited on page 56.

Tremblay, P. E. et al. 3D Model Atmospheres for Extremely Low-mass White Dwarfs. , v. 809, n. 2, p. 148, ago. 2015. Cited 2 times on pages 61 and 62.

Udalski, A. et al. The Optical Gravitational Lensing Experiment. , v. 42, p. 253–284, out. 1992. Cited on page 45.

Unno, W. et al. *Nonradial oscillations of stars*. [S.l.: s.n.], 1989. Cited on page 39.

Van Grootel, V. et al. The Newly Discovered Pulsating Low-mass White Dwarfs: An Extension of the ZZ Ceti Instability Strip. , v. 762, n. 1, p. 57, jan. 2013. Cited on page 50.

Van Reeth, T. et al. Sensitivity of gravito-inertial modes to differential rotation in intermediate-mass main-sequence stars. , v. 618, p. A24, out. 2018. Cited on page 56.

Vernet, J. et al. X-shooter, the new wide band intermediate resolution spectrograph at the ESO Very Large Telescope. , v. 536, p. A105, dez. 2011. Cited on page 69.

Wang, B.; Podsiadlowski, P.; Han, Z. He-accreting carbon-oxygen white dwarfs and Type Ia supernovae. *Monthly Notices of the Royal Astronomical Society*, v. 472, p. 1593–1599, dez. 2017. Cited on page 53.

Warner, B.; van Zyl, L. Discovery of non-radial pulsations in the white dwarf primary of a cataclysmic variable star. In: Deubner, F.-L.; Christensen-Dalsgaard, J.; Kurtz, D. (Ed.). *New Eyes to See Inside the Sun and Stars*. [S.l.: s.n.], 1998. v. 185, p. 321. Cited on page 47.

Werner, K.; Herwig, F. The elemental abundances in bare planetary nebula central stars and the shell burning in agb stars. *Publications of the Astronomical Society of the Pacific*, [The University of Chicago Press, Astronomical Society of the Pacific], v. 118, n. 840, p. 183–204, 2006. ISSN 00046280, 15383873. Disponível em: <http://www.jstor.org/stable/10.1086/500443>. Cited on page 47.

Winget, D. E.; Kepler, S. O. Pulsating white dwarf stars and precision asteroseismology. , v. 46, p. 157–199, set. 2008. Cited on page 46.

Winget, D. E. et al. Asteroseismology of the DOV Star PG 1159-035 with the Whole Earth Telescope. , v. 378, p. 326, set. 1991. Cited on page 51.

Winget, D. E. et al. Photometric observations of GD 358 : DB white dwarfs do pulsate. , v. 262, p. L11–L15, nov. 1982. Cited on page 47.

Winget, D. E. et al. A Strong Test of Electroweak Theory Using Pulsating DB White Dwarf Stars as Plasmon Neutrino Detectors. , v. 602, n. 2, p. L109–L112, fev. 2004. Cited on page 46.

Winget, D. E. et al. Hydrogen-driving and the blue edge of compositionally stratified ZZ Ceti star models. , v. 252, p. L65–L68, jan. 1982. Cited on page 47.

Woosley, S. E.; Heger, A. The Remarkable Deaths of 9-11 Solar Mass Stars. *The Astrophysical Journal*, v. 810, p. 34, set. 2015. Cited on page 35.

York, D. G. et al. The Sloan Digital Sky Survey: Technical Summary. , v. 120, n. 3, p. 1579–1587, set. 2000. Cited on page 45.

Zenati, Y.; Toonen, S.; Perets, H. B. Formation and evolution of hybrid He-CO white dwarfs and their properties. , v. 482, n. 1, p. 1135–1142, jan. 2019. Cited 2 times on pages 37 and 49.

Zwintz, K. et al. A comprehensive study of young B stars in NGC 2264 . I. Space photometry and asteroseismology. , v. 601, p. A101, maio 2017. Cited on page 56.

Appendix

APPENDIX A – Equations of pulsation

In this section will be presented a description of the equations and considerations that control the non-radial oscillations. Let us consider a self-gravitating gaseous spherically symmetric star in the absence of external forces (i.e no magnetic field) and without rotation. The basic hydrostatic equations that control the non-radial pulsations are: Equation of mass (A.1), momentum (A.2), and energy conservation (A.3):

$$\frac{\partial \rho}{\partial t} + \nabla \cdot (\rho \vec{u}) = 0 \tag{A.1}$$

$$\rho \left(\frac{\partial}{\partial t} + \vec{u} \cdot \nabla \right) \vec{u} = \rho \vec{f} - \nabla P - \rho \nabla \Phi + \nabla \Theta \tag{A.2}$$

$$\rho T \left(\frac{\partial}{\partial t} + \vec{u} \cdot \nabla \right) S = \rho \left(\epsilon_N + \epsilon_V \right) - \nabla \cdot \vec{F}_R \quad . \tag{A.3}$$

Where ρ denotes the density, P the pressure, T the temperature, $\vec{u}$ the fluid velocity, S the specific entropy, Φ the gravitational potential, $\vec{f}$ the electro-magnetic and external forces, Θ the viscous stress tensor,ϵ_N the nuclear energy generation rate, ϵ_V the viscous heat generation, $\vec{F}_R$ the radiative energy flux, ∇ the gradient operator.

In order to describe a complete system, supplementary equations are needed. The first one of them is the Poisson equation, which relates the distribution of matter to the gravitational potential,

$$\nabla^2 \Phi = 4\pi G \rho \quad , \tag{A.4}$$

and the second is the radiative flux given by the radiative diffusion equation,

$$\vec{F}_R = -K \nabla T \quad , \tag{A.5}$$

where G is the gravitational constant, ∇^2 is the Laplacian operator, and K is the radiative conductivity that is written in terms of the opacity κ as:

$$K = \frac{4ac}{3\kappa\rho} T^3 \quad , \tag{A.6}$$

where a is the radiation density constant and c is the velocity of light. The remaining supplementary equations are equations of state giving $P(\rho, T)$, $S(\rho, T)$, $\epsilon_N(\rho, T)$, $\kappa(\rho, T)$ for a given chemical composition.

For simplicity, the convection will be neglected as it adds complexity to the velocity term. Also, in the absence of convection, the viscosity term in our equations becomes rather small, hence it will be neglected together with the viscous heat generation rate ($\nabla \Theta = 0$ and $\epsilon_V = 0$). We are also considering a non-rotating, non-magnetic star. Hence the term of external forces is set to zero. Under these conditions, equations (A.1) to (A.3) become:

$$\frac{\partial \rho}{\partial t} + \nabla \cdot (\rho \vec{v}) = 0 \tag{A.7}$$

$$\rho \left(\frac{\partial}{\partial t} + \vec{v} \cdot \nabla \right) \vec{v} = -\nabla P - \rho \nabla \Phi \tag{A.8}$$

$$\rho T \left(\frac{\partial}{\partial t} + \vec{v} \cdot \nabla \right) S = \rho \epsilon_N - \nabla \cdot \vec{F}_R \quad , \tag{A.9}$$

while equations (A.4) and (A.5) keep unchanged.

Note that the fluid velocity term $\vec{u}$ was changed to $\vec{v}$ to distinguish the fluid velocity without convection. The last addition is the equilibrium state, upon which small perturbations of oscillations are superimposed. By adding the subscript 0 to denote the unperturbed equilibrium state and setting the time derivative and equilibrium velocity to zero ($\partial/\partial t = 0$ and $\vec{v}_0 = 0$) in equations (A.4) to (A.9), we obtain:

$$-\nabla P_0 - \rho_0 \nabla \Phi_0 = 0 \tag{A.10}$$

$$\rho_0 \epsilon_{N,0} - \nabla \cdot \vec{F}_{R,0} = 0 \tag{A.11}$$

$$\nabla^2 \Phi_0 = 4\pi G \rho_0 \tag{A.12}$$

$$\vec{F}_{R,0} = -K_0 \nabla T \quad . \tag{A.13}$$

To further derive the equations of oscillations, we have to consider the unperturbed equilibrium state of a star and superimpose on it small perturbations. We assume that those perturbations are sufficiently small, thus using the linear theory and neglecting the terms of a higher order than one in the perturbations.

The perturbations of a physical quantity f can be described in two different ways: The Eulerian form (f') and the Lagrangian form (δf). The difference among them is that the Eulerian form is defined as a perturbation at a given position while the Lagrangian is a perturbation for a given fluid element. A physical quantity f is therefore expressed by either:

$$f(\vec{r}, t) = f_0(\vec{r}) + f'(\vec{r}, t) \tag{A.14}$$

$$f(\vec{r}, t) = f_0(\vec{r}_0) + \delta f(\vec{r}_0, t) \quad . \tag{A.15}$$

The Lagrangian and Eulerian perturbations are related to each other by

$$\delta f(\vec{r}, t) = f'(\vec{r}, t) + \vec{\xi} \cdot \nabla f_0(\vec{r}) \quad , \tag{A.16}$$

where $\vec{\xi} = \vec{r} - \vec{r}_0$ is the displacement of the Lagrangian position variable of a given fluid element which is at $\vec{r} = \vec{r}_0$ in the equilibrium state. For the equilibrium state ($\vec{v}_0 = 0$), the velocity perturbation is given by:

$$\vec{v} = \vec{v}' = \delta \vec{v} = \frac{\mathrm{d}\vec{\xi}}{\mathrm{d}t} \quad . \tag{A.17}$$

With the above preparations, the physical quantities in equations (A.10) to (A.13) can be expressed as its equilibrium value plus a small Eulerian perturbation:

$$\rho = \rho_0 + \rho' \tag{A.18}$$

$$\Phi = \Phi_0 + \Phi' \tag{A.19}$$

$$P = P_0 + P' \tag{A.20}$$

$$\vec{v} = \vec{v}_0 + \vec{v}' \tag{A.21}$$

$$T = T' + T_0 \quad . \tag{A.22}$$

Replacing the above quantities into equations (A.10) to (A.13), we obtain:

$$\frac{\partial \rho'}{\partial t} + \nabla \cdot (\rho_o \vec{v}) = 0 \tag{A.23}$$

$$\rho_0 \frac{\partial \vec{v}}{\partial t} + \nabla P' + \rho \nabla \Phi' + \rho' \nabla \Phi_0 = 0 \tag{A.24}$$

$$\nabla^2 \Phi' = 4\pi G \rho' \tag{A.25}$$

$$\vec{F}_R' = -K_0 \nabla T' - K' \nabla T_0 \quad . \tag{A.26}$$

Equations (A.23) to (A.26) are linear, homogeneous, partial differential equations for perturbed variables (e.g ρ', T', Φ', etc.) with respect to time t, spacial coordinates r, velocity vector $\vec{v}$ and Lagrangian displacement $\vec{\xi}$. The coefficients of these partial differential equations include solely quantities at equilibrium such as ρ_0, T_0, etc., which are functions of radial coordinate only as we are assuming a perturbed model with spherical symmetry:

$$\rho_0 = \rho_0(\vec{r}), \quad T_0 = T(_0\vec{r}), \quad \Phi_0 = \Phi_0(\vec{r}), \quad \ldots \quad . \tag{A.27}$$

Henceforth, we omit the subscript 0 for equilibrium quantities unless there is confusion.

Since we are assuming spherical symmetry, we can rewrite our equations as functions in spherical polar coordinates plus time:

$$f' = f'(r, \theta, \phi, t) \quad , \tag{A.28}$$

where r is the radius, θ the colatitude, and ϕ the azimuth angle. We may separate the time t by assuming the temporal perturbations to be proportional to $e^{i\sigma t}$, where σ is the angular frequency, which is related to the cyclic frequency ν and the period Π by:

$$\nu = \frac{\sigma}{2\pi} = \frac{1}{\Pi} \quad . \tag{A.29}$$

Therefore, any physical quantity can be rewritten in the following form:

$$f'(r, \theta, \phi, t) = f'(r, \theta, \phi)\, e^{i\sigma t} \quad . \tag{A.30}$$

Let us now express the density perturbation from the following thermodynamic relation:

$$\frac{\rho'}{\rho} = \frac{1}{\Gamma_1}\frac{P'}{P} - A\xi_r - \nabla_{ad}\frac{\rho T}{P}\delta S \quad , \tag{A.31}$$

where Γ_1, ∇_{ad} and A are given by:

$$\Gamma_1 = \left(\frac{\partial \ln P}{\partial \ln \rho}\right)_S \tag{A.32}$$

$$\nabla_{ad} = \left(\frac{\partial \ln T}{\partial \ln P}\right)_S \tag{A.33}$$

$$A = \frac{\mathrm{d}\ln\rho}{\mathrm{d}r} - \frac{1}{\Gamma_1}\frac{\mathrm{d}\ln P}{\mathrm{d}r} \quad . \tag{A.34}$$

The ξ_r is the radial component of $\vec{\xi}$ and A is the Schwarzschild discriminant which denotes the degree of convective instability ($A > 0$) or stability ($A < 0$)

Applying the dependence of equation (A.30) and the equation (A.31) into equations (A.23) to (A.25), we have:

$$\frac{1}{\rho}\left(\frac{\partial}{\partial r} + \frac{\rho g}{\Gamma_1 P}\right)P' - \left(\sigma^2 + gA\right)\xi_r + \frac{\partial \Phi'}{\partial r} = g\nabla_{ad}\frac{\rho T}{P}\delta S \tag{A.35}$$

$$\frac{1}{r}\frac{\partial(r^2\xi_r)}{\partial r} + \frac{1}{\Gamma_1}\frac{\mathrm{d}\ln P}{\mathrm{d}r}\xi_r + \left(\frac{\rho}{\Gamma_1 P} + \frac{\nabla_\perp^2}{\sigma^2}\right)\frac{P'}{\rho} + \frac{1}{\sigma^2}\nabla_\perp^2\Phi' = \nabla_{ad}\frac{\rho T}{P}\delta S \tag{A.36}$$

$$\left(\frac{1}{r^2}\frac{\partial}{\partial r}r^2\frac{\partial}{\partial r} + \nabla_\perp^2\right)\Phi' - 4\pi G\rho\left(\frac{P'}{\Gamma_1 P} - A\xi_r\right) = -4\pi G\nabla_{ad}\frac{\rho^2 T}{P}\delta S \tag{A.37}$$

$$i\sigma\rho T\delta S = (\rho\epsilon_N)' - \frac{1}{r^2}\frac{\partial(r^2 F_r')}{\partial r} + \nabla_\perp^2(KT') \tag{A.38}$$

$$F_r' = -K\frac{\partial T'}{\partial r} - K'\frac{\mathrm{d}T}{\mathrm{d}r} \quad , \tag{A.39}$$

where $\nabla_\perp^2$ is the differential operator in the spherical polar coordinates:

$$\nabla_\perp^2 = \frac{1}{r^2}\frac{1}{\sin^2\theta}\left[\sin\theta\frac{\partial}{\partial\theta}\left(\sin\theta\frac{\partial}{\partial\theta}\right) + \frac{\partial^2}{\partial\phi^2}\right] \quad , \tag{A.40}$$

and F_r' is the radial component of the perturbed $\vec{F}_R'$

The coefficients in equations (A.35) to (A.39) are time independent. Their only dependency is with the radial component r and the one and only differential operator with respect to the angular variables θ and ϕ is $\nabla_\perp^2$. In this case, the separations of variables into radial and angular parts is possible by spherical harmonics $Y_\ell^m(\theta,\phi)$, which are eigenfunctions of the $L^2 = r^2\nabla_\perp^2$ operator with eigenvalues $l(l+1)$:

$$L^2 Y_\ell^m(\theta,\phi) = l(l+1)Y_\ell^m(\theta,\phi) \quad . \tag{A.41}$$

The explicit form of the spherical harmonics is given by:

$$Y_\ell^m(\theta,\phi) = (-1)^{(m+|m|)/2}\left[\frac{2l+1}{2\pi}\frac{(l-|m|)}{(l+|m|)!}\right]^{1/2} P_\ell^{|m|}(\cos\theta)e^{im\phi} \quad , \tag{A.42}$$

where $m = -\ell, -\ell+1, \dots, \ell-1, \ell$ and $P_\ell^{|m|}(\cos\theta)$ is the Legendre Polynomials. Therefore, we can rewrite the perturbations for any physical quantity as:

$$f'(r,\theta,\phi) = f(r)Y_\ell^m(\theta,\phi) \quad . \tag{A.43}$$

Hence, the expression for the displacement vector $\vec{\xi}$ is given by:

$$\vec{\xi} = \left[\xi_r(r), \xi_h(r)\frac{\partial}{\partial\theta}, \xi_h(r)\frac{\partial}{\sin\theta\partial\phi}\right] Y_\ell^m(\theta,\phi)e^{i\theta t} \quad , \tag{A.44}$$

where ξ_h is:

$$\xi_h = \frac{1}{\partial^2 r}\left(\frac{P'}{\rho} + \Phi'\right). \tag{A.45}$$

Assuming that the perturbed physical quantities are given by (A.43), we obtain a set of ordinary differential equations from equations (A.35) to (A.39) as follows:

$$\frac{1}{\rho}\frac{\mathrm{d}P'}{\mathrm{d}r} + \frac{g}{\rho c_S^2}P' + \left(N^2 - \sigma^2\right)\xi_r + \frac{\mathrm{d}\Phi'}{\mathrm{d}r} = g\nabla_{ad}\frac{\rho T}{P}\delta S \tag{A.46}$$

$$\frac{1}{r^2}\frac{\mathrm{d}}{\mathrm{d}r}\left(r^2\xi_r\right) + \frac{1}{\Gamma_1}\frac{\mathrm{d}\ln P}{\mathrm{d}r}\xi_r + \left(1 - \frac{L_\ell^2}{\sigma^2}\right)\frac{P'}{\rho c_S^2} - \frac{\ell(\ell+1)}{\sigma^2 r^2}\Phi' = \nabla_a d\frac{\rho T}{P}\delta S \tag{A.47}$$

$$\frac{1}{r^2}\frac{\mathrm{d}}{\mathrm{d}r}\left(r^2\frac{\mathrm{d}\Phi^2}{\mathrm{d}r}\right) - \frac{\ell(\ell+1)}{r^2}\Phi' - 4\pi G\rho\left(\frac{P'}{\rho c_S^2} + \frac{N^2}{g}\xi_r\right) = -4\pi G\nabla_{ad}\frac{\rho^2 T}{P}\delta S \tag{A.48}$$

$$K\frac{\mathrm{d}T'}{\mathrm{d}r} = -F_r' - K'\frac{\mathrm{d}T}{\mathrm{d}r} \tag{A.49}$$

$$i\sigma\rho T\delta S = (\rho\epsilon_N)' - \frac{1}{r^2}\frac{\mathrm{d}(r^2F_r')}{\mathrm{d}r} - \frac{\ell(\ell+1)}{r^2}KT' \quad , \tag{A.50}$$

where $c_s^2 = (\Gamma_1 P/\rho)^{1/2}$ is the local sound speed, N and L_ℓ are the Brunt-Väisälä and Lamb frequencies, respectively, given by:

$$N^2 = g\left(\frac{1}{\Gamma_1}\frac{\mathrm{d}\ln P}{\mathrm{d}\ln r} - \frac{\mathrm{d}\ln\rho}{\mathrm{d}\ln r}\right) \tag{A.51}$$

$$L_\ell^2 = \frac{\ell(\ell+1)}{r^2}c_S^2 \quad . \tag{A.52}$$

The properties of stellar oscillations can be studied assuming the adiabatic approximations, where the specific entropy is conserved during the oscillations:

$$\delta S = 0 \quad . \tag{A.53}$$

In this approximation, there is no heat exchange between fluids in the internal regions of the star. Applying the condition (A.53) into the density perturbation given by equation (A.31), we have:

$$\rho' = \frac{P'}{c_S^2} + \frac{\xi_r \rho N^2}{g} \quad , \tag{A.54}$$

which express the relation between the density perturbation and the pressure perturbation. Therefore, we can rewrite the equations (A.46) to (A.48):

$$\frac{1}{r^2}\frac{\mathrm{d}(r^2\xi_r)}{\mathrm{d}r} - \frac{g}{c_S^2}\xi_r + \left(1 - \frac{L_\ell^2}{\sigma^2}\right)\frac{P'}{\rho c_S^2} = \frac{\ell(\ell+1)}{\sigma^2 r^2}\Phi' \tag{A.55}$$

$$\frac{1}{\rho}\frac{\mathrm{d}P'}{\mathrm{d}r} + \frac{g}{\rho c_S^2}P' + (N^2 - \sigma^2)\xi_r = -\frac{\mathrm{d}\Phi}{\mathrm{d}r} \tag{A.56}$$

$$\frac{1}{r^2}\frac{\mathrm{d}}{\mathrm{d}r}\left(r^2\frac{\mathrm{d}\Phi^2}{\mathrm{d}r}\right) - \frac{\ell(\ell+1)}{r^2}\Phi' = 4\pi G\rho\left(\frac{P'}{\rho c_S^2} + \frac{N^2}{g}\xi_r\right) \quad . \tag{A.57}$$

These equations with proper boundary conditions, give an eigenvalue problem with an eigenvalue σ^2, where the solutions are given by normal oscillations modes. It will be considered the boundary conditions at the center ($r = 0$) and at the surface ($r = R_* \rightarrow P = 0$) where the above equations are singular. Also, the above equations are independent of the azimuth number m and show degeneration of order $2\ell + 1$ on the eigenvalues.

In order to solve numerically the equation (A.55) to (A.57), it is necessary to rewrite them in four first-order differential equations with four dimensionless variables. The new dimensionless variables are defined as:

$$\begin{aligned} y_1 &= \frac{\xi_r}{r}, \quad y_2 = \frac{1}{gr}\left(\frac{P'}{\rho} + \Phi'\right) \\ y_3 &= \frac{\Phi'}{gr}, \quad y4 = \frac{1}{g}\frac{\mathrm{d}\Phi'}{\mathrm{d}r} \quad . \end{aligned} \tag{A.58}$$

The variables ξ_r, P', Φ' and $\mathrm{d}\Phi'/\mathrm{d}r$ are them represented by

$$\begin{aligned} \xi_r &= r y_1, \quad P' = \rho g r(y_2 - y_1) \\ \Phi' &= g r y_3, \quad \frac{\mathrm{d}\Phi'}{\mathrm{d}r} = g y_4 \quad . \end{aligned} \tag{A.59}$$

The substitution of equations (A.59) into the equations (A.55) to (A.57) gives

$$x\frac{\mathrm{d}y_1}{\mathrm{d}r} = (V_g - 3)y_1 + \left[\frac{\ell(\ell+1)}{c_1\omega^2} - V_g\right]y_2 + V_g y_3 \tag{A.60}$$

$$x\frac{\mathrm{d}y_2}{\mathrm{d}r} = (c_1\omega^2 - A^*)y_1 + (A^* - U + 1)y_2 - A^* y_3 \tag{A.61}$$

$$x\frac{\mathrm{d}y_3}{\mathrm{d}r} = (1 - U)y_3 + y_4 \tag{A.62}$$

$$x\frac{\mathrm{d}y_4}{\mathrm{d}r} = UA^* y_1 + UV_g y_2 + [\ell(\ell+1) - UV_g]\, y_3 - U y_4 \quad , \tag{A.63}$$

where

$$V_g = -\frac{1}{\Gamma_1}\frac{\mathrm{d}\ln P}{\mathrm{d}\ln r} = \frac{gr}{c_S^2} \tag{A.64}$$

$$U = \frac{\mathrm{d}\ln M_r}{\mathrm{d}\ln r} = \frac{4\pi\rho r^3}{M_r} \tag{A.65}$$

$$c_1 = \left(\frac{r}{R_*}\right)^3 \frac{M_*}{M_r} \tag{A.66}$$

$$A^* = \frac{r}{g}N^2 = g\left(\frac{1}{\Gamma_1}\frac{\mathrm{d}\ln P}{\mathrm{d}\ln r} - \frac{\mathrm{d}\ln \rho}{\mathrm{d}\ln r}\right) \tag{A.67}$$

$$\omega^2 = \sigma^2 \frac{R^3}{GM} \tag{A.68}$$

$$x = \frac{r}{R_*} \quad , \tag{A.69}$$

and M_r is the enclosed mass in a sphere of radius r and M_* and R_* are the total mass and radius of the star.

The boundary conditions in the dimensionless form and the normalization that completes the system of equations are:

i at the center ($x = 0$)

$$y_1 c_1 \omega^2 - \ell y_2 = 0 \tag{A.70}$$

$$\ell y_3 - y_4 = 0 \tag{A.71}$$

ii at the surface ($x = 1$)

$$y_1 - y_2 + y_3 = 0 \tag{A.72}$$

$$(\ell + 1)y_3 + y_4 = 0 \tag{A.73}$$

iii Normalization condition

$$y_1 = 1 \quad \text{at} \quad x = 1 \quad . \tag{A.74}$$

These equations form a set of first-order differential equations of linear adiabatic non-radial oscillation, in which the coefficients are expressed in terms of dimensionless stellar equilibrium quantities with a proper boundary condition.

APPENDIX B – Published Paper

Monthly Notices of the ROYAL ASTRONOMICAL SOCIETY

MNRAS **510,** 858–869 (2022) https://doi.org/10.1093/mnras/stab3487
Advance Access publication 2021 December 2

Uncovering the chemical structure of the pulsating low-mass white dwarf SDSS J115219.99+024814.4

A. D. Romero ,[1★] G. R. Lauffer ,[1] A. G. Istrate [2] and S. G. Parsons [3]

[1]Physics Institute, Universidade Federal do Rio Grande do Sul, Avenida Bento Goncalves 9500, Porto Alegre 91501-970, RS, Brazil
[2]Department of Astrophysics, Radboud University Nijmegen, P.O. Box 9010, Nijmegen NL-6500 GL, the Netherlands
[3]Department of Physics and Astronomy, University of Sheffield, Sheffield, S3 7RH, UK

Accepted 2021 November 26. Received 2021 October 22; in original form 2021 March 14

ABSTRACT

Pulsating low-mass white dwarf (WD) stars are WDs with stellar masses between 0.30 and 0.45 $M_\odot$ that show photometric variability due to gravity-mode pulsations. Within this mass range, they can harbour both a helium core and hybrid core, depending if the progenitor experienced helium-core burning during the pre-WD evolution. SDSS J115219.99+024814.4 is an eclipsing binary system where both components are low-mass WDs, with stellar masses of 0.362 ± 0.014 $M_\odot$ and 0.325 ± 0.013 $M_\odot$. In particular, the less-massive component is a pulsating star, showing at least three pulsation periods of ∼1314, ∼1069, and ∼582.9 s. This opens the way to use asteroseismology as a tool to uncover its inner chemical structure, in combination with the information obtained using the light-curve modelling of the eclipses. To this end, using binary evolutionary models leading to helium- and hybrid-core WDs, we compute adiabatic pulsations for $\ell = 1$ and $\ell = 2$ gravity modes with `Gyre`. We found that the pulsating component of the SDSS J115219.99+024814.4 system must have a hydrogen envelope thinner than the value obtained from binary evolution computations, independently of the inner composition. Finally, from our asteroseismological study, we find a best-fitting model characterized by $T_{\rm eff} = 10\,917$ K, $M = 0.338$ $M_\odot$, and $M_{\rm H} = 10^{-6}$ $M_\odot$ with the inner composition of a hybrid WD.

Key words: asteroseismology – binaries: eclipsing – white dwarfs.

1 INTRODUCTION

White dwarfs (WDs) are the most common endpoint of stellar evolution. All stars with initial masses below 7−12 $M_\odot$ (e.g. Garcia-Berro, Isern & Hernanz 1997; Woosley & Heger 2015; Lauffer, Romero & Kepler 2018), representing more than 95 per cent of the stars in the Milky Way, will end their lives as WDs. The WD population can be divided into hydrogen (H)-rich atmosphere objects (DA), that correspond to more than 85 per cent of all WDs, and H-deficient objects (non-DA), which show no H in their atmospheres (see Fontaine & Brassard 2008; Althaus et al. 2010a).

For H-atmosphere WDs the mass distribution peaks at ∼0.6 $M_\odot$, which represents ∼84 per cent of the total sample (Kepler et al. 2007; Kepler et al. 2015), exhibiting also a high- and a low-mass components. The low- and high-mass WDs are most likely the result of close binary evolution, where mass transfer and mergers commonly occur.

The low-mass tail in the DA mass distribution peaks at ∼0.39 $M_\odot$ and extends to stellar masses <0.45 $M_\odot$. WDs with masses <∼0.30 $M_\odot$ can only be formed through mass transfer in close binary systems, since single star evolution is not able to form such remnants in the Hubble time (Kilic, Stanek & Pinsonneault 2007; Istrate et al. 2016; Pelisoli & Vos 2019). These objects are known as extremely low-mass white dwarfs (ELMs). Low-mass WDs are stars with stellar masses in the range of $0.30 \le M/M_\odot \le 0.45$. In addition to the binary formation channel, these objects could also form as a result of strong mass-loss episodes during giant stages for high-metallicity progenitors. Noteworthy, low-mass WDs can harbour either a pure helium (He) core (e.g. Panei et al. 2007; Althaus, Miller Bertolami & Córsico 2013; Istrate, Tauris & Langer 2014; Istrate et al. 2016) or a hybrid core, composed of He, carbon (C), and oxygen (O; e.g. Iben & Tutukov 1985; Han, Tout & Eggleton 2000; Prada Moroni & Straniero 2009; Zenati, Toonen & Perets 2019).

Probably the only way to probe the inner chemical composition in detail is through the pulsation-period spectrum observed in variable stars. Each pulsation mode propagates in a specific region providing information on that particular zone, where its amplitude is maximum (Tassoul, Fontaine & Winget 1990). Thus, we can perform an asteroseismic study, where we compare the observed periods with the theoretical period spectrum, computed using representative models, to uncover the inner stellar structure (see e. g. Romero et al. 2012, 2019).

There are currently several families of pulsating WDs that can be found in specific ranges of effective temperature and surface gravity. They show g-mode non-radial pulsations with periods range from minutes to a few hours and variation amplitudes of millimag. The excitation mechanism acting on pulsating WDs is a combination of the κ-mechanism, driven by an opacity bump due to partial ionization of the main element in the outer layers (Dolez & Vauclair 1981; Winget et al. 1982), and the γ-mechanism, related to the effect of a small value of the adiabatic exponent in the ionization zone (Brickhill 1991; Goldreich & Wu 1999).

The location of the different classes in the Kiel diagram is depicted in Fig. 1. At high effective temperatures we find the GW

★ E-mail: alejandra.romero@ufrgs.br

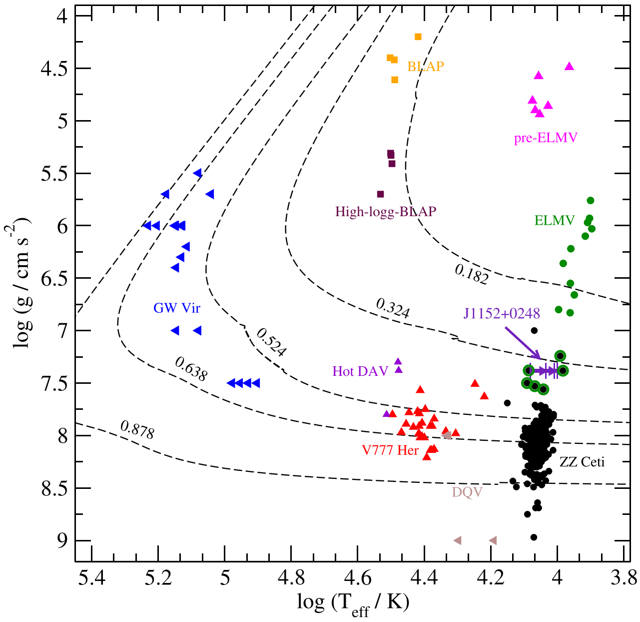

Figure 1. The classes of pulsating WDs. The data were extracted from Fontaine & Brassard (2008), Bognar & Sodor (2016), Pietrukowicz et al. (2017), Córsico et al. (2019), Romero et al. (2019), and Kupfer et al. (2019). For reference, we include theoretical WD sequences with C/O core and masses of 0.878, 0.638, and 0.524 $M_\odot$ (Romero, Campos & Kepler 2015) and He-core with stellar mass of 0.324 and 0.182 $M_\odot$ (Istrate et al. 2016). The different symbols indicate the element related to the excitation mechanism: H (circles), He (triangle-up), C and/or O (triangle-left), and iron peak elements (squares). The known variable low-mass WDs are indicated with a surrounding green circle. The position of J115219.99+024814.4 is depicted with a triangle-right, with the atmospheric parameters taken from Parsons et al. (2020; see Table 1 for details).

Vir stars, with C/O atmospheres, followed by He-rich atmosphere V777 Her and the C-rich atmosphere DQV. Finally, the H-envelope pulsating WDs, known as ZZ Ceti stars, are located at lower effective temperatures. For lower log (g), we find the pulsating low-mass WDs, and the ELMs along with their progenitors, the pre-ELMs. Even though the group of pulsating ELMs is considered a class on its own, their instability strip is an extension of the ZZ Ceti instability strip to lower surface gravities, as can be seen from Fig. 1.

There are 11 pulsating ELMs known to date (green dots in Fig. 1, Hermes et al. 2013a, b; Bell et al. 2015, 2017; Kilic et al. 2015; Pelisoli et al. 2018). The pulsating ELMs are characterized by periods in the range of 100−6 300 s, effective temperatures of 7 800−10 000 K, and an H-dominated surface composition (Córsico et al. 2019). In addition, there are 10 objects in the literature with stellar masses within the range $0.30 \leq M/M_\odot \leq 0.45$ (black-green dots in Fig. 1) that show photometric variability with periods between 200 and 1300 s (Bognar & Sodor 2016; Fuchs 2017; Su et al. 2017; Rowan et al. 2019). For four of them, the uncertainties in the atmospheric parameters are quite large, leading to an uncertainty in stellar mass of 0.1–0.4 $M_\odot$ (Su et al. 2017; Rowan et al. 2019). The low number of pulsating low-mass WDs as compared to canonical mass ZZ Ceti stars could be due to some kind of fine tuning during the evolution of the progenitor, but it is most likely due to the lack of studies focused on the search for pulsations for objects in this stellar mass range.

Recently, Parsons et al. (2020) reported the discovery of the first pulsating low-mass WDs in a compact eclipsing binary system (orbital period of 2.4 h), which happens to have another low-mass WD as a companion. The binary nature of the SDSS J115219.99+024814.4 system (hereafter J1152+0248) was first reported by Hallakoun et al. (2016), based on K2 data from the *Kepler* mission. Parsons et al. (2020) performed high-speed photometry observations with HiPERCAM on the 10.4 m *Gran Telescopio Canárias* in five different bands, with a total of 108 min of data, covering both primary and secondary eclipses. From the high time-resolution light curves they found pulsation-related variations from the cooler component with at least three significant periods. To determine the mass and radius of each component in J1152+0248, they combine radial velocity determinations from X-shooter spectroscopy with the information extracted from the primary and secondary eclipses in the light curves (see their table 1). The effective temperature was determined using two techniques, i.e. by fitting the spectral energy distribution [$T_{\rm eff}$ (SED)] and by modelling the light curves including the effects of the eclipses [$T_{\rm eff}$ (eclipse)]. The stellar parameters obtained by Parsons et al. (2020) for the pulsating component in J1152+0248 (hereafter J1152+0248 −V) are listed in Table 1.

Table 1. Stellar parameters presented in Parsons et al. (2020) for the pulsating component of the J1152+0248 eclipsing binary.

Parameter	Value
$M_*/M_\odot$	0.325 ± 0.013
$R_*/R_\odot$	0.0191 ± 0.0004
log [g/(g cm^{-2})]	7.386 ± 0.012
$T_{\rm eff}$/K (SED)	$11\,100^{+950}_{-770}$
$T_{\rm eff}$/K (eclipse)	$10\,400^{+400}_{-340}$

Based on the determination of the radius, Parsons et al. (2020) proposed that J1152+0248 −V is either a hybrid- or an He-core low-mass WD with an extremely thin surface H layer ($M_{\rm H}/M_\odot < 10^{-8}$). Different inner chemical structures will influence the characteristic period spectrum of a pulsating star. Therefore, an asteroseismological study of this object can shed some light on both the chemical composition and the mass of the H envelope.

In this work, we explore the pulsational properties of both hybrid- and He-core low-mass WD models representative for the case of J1152+0248 −V. Furthermore, we consider sequences with H envelopes thinner than the value predicted by stable mass-transfer binary evolutionary models. For the evolutionary computations we use the stellar evolution code MESA (Paxton et al. 2011, 2013, 2015, 2018, 2019), while the adiabatic pulsations are computed using GYRE stellar oscillation code (Townsend & Teitler 2013; Townsend, Goldstein & Zweibel 2018). Using the theoretical period spectra, we perform an asteroseismological study of J1152+0248 −V to uncover its inner structure.

This paper is organized as follows. In Section 2, we provide a description of the evolutionary computations and the input physics adopted in our calculations. In Section 3, we present the pulsation computations. Section 4 is devoted to study the pulsational properties of our low-mass WD models, including a comparison between the hybrid- and He-core configurations. The results of the asteroseismological study of J1152+0248 −V are presented in this section as well. Our final remarks are presented in Section 5.

2 EVOLUTIONARY SEQUENCES

The evolutionary models presented in this work are computed using the open-source binary stellar evolution code MESA (Paxton et al. 2011, 2013, 2015, 2018, 2019) version 12115 and are part of a grid of models covering the mass interval where He- and hybrid-core WDs overlap, i.e. ∼0.32–0.45 $M_{\odot}$ (Istrate et al., in preparation). Since the aim of this work is analyse the core composition of J1152+0248 −V using asteroseismology, we only consider sequences compatible with its observed effective temperature and radius. We present evolutionary sequences for a WD mass of 0.325 $M_{\odot}$, corresponding to the value obtained by Parsons et al. (2020), and 0.338 $M_{\odot}$, i.e. the maximum WD mass compatible within 1σ.

2.1 Input physics

We compute binary evolutionary sequences using similar assumptions as in Istrate et al. (2016). All models include rotation, with the initial rotational velocity initialized such that the donor is synchronized with the orbital period. We include magnetic braking for the loss of angular momentum just for the donors leading to the formation of the He-core WDs. For more massive donors (>2.0 $M_{\odot}$), which are considered for the progenitors of the hybrid-core WDs, we assume that the magnetic braking stops operating. This assumption follows from the conventional thinking that braking via a magnetized stellar wind is inoperative in stars with radiative envelopes (Kawaler 1988). For all the models, we assume a mass-transfer efficiency of 50 per cent, i.e. 50 per cent of the transferred mass is accreted by the companion, while the rest leaves the system with the specific angular momentum of the accretor.

Below, we briefly describe the main input physics considered in the evolutionary computations and refer to Istrate et al. (in preparation) for more details. We consider an initial metallicity of $Z = 0.01$, with an He abundance given by $Y = 0.24+2.0 \cdot Z$ and the metal abundances scaled according to Grevesse & Sauval (1998). Convection is modelled using the standard mixing-length theory (Henyey, Vardya & Bodenheimer 1965) with a mixing-length parameter $\alpha = 2.0$, adopting the Ledoux criterion. A step function overshooting extends the mixing region for 0.25 pressure scale heights beyond the convective boundary during core H burning. In order to smooth the boundaries we also include exponential overshooting with $f = 0.0005$. Semiconvection follows the work of Langer, Fricke & Sugimoto (1983), with an efficiency parameter $\alpha_{sc} = 0.001$. Thermohaline mixing is included with an efficiency parameter of 1.0. Radiative opacities are taken from Ferguson et al. (2005) for $2.7 \leq \log T \leq 3.8$ and OPAL (Iglesias & Rogers 1993, 1996) for $3.75 \leq \log T \leq 8.7$, and conductive opacities are adopted from Cassisi et al. (2007).

The nuclear network used is *cno_extras.net* which accounts for additional nuclear reactions for the CNO burning compared to the default *basic.net* network. We consider the effects of element diffusion (e.g. Iben & Tutukov 1985; Thoul, Bahcall & Loeb 1994) on all isotopes and during all the stages of evolution.

We adopt a grey atmosphere using the Eddington approximation on the evolution prior to the cooling track, and the WD atmosphere tables from Rohrmann et al. (2012) during the WD cooling stage.

Rotational mixing and angular momentum transport are treated as diffusive processes as described in Heger, Langer & Woosley (2000), with an efficiency parameter $f_c = 1/30$ (Chaboyer & Zahn 1992) and a sensitivity to composition gradients parametrized by $f_{\mu} = 0.05$. We also include transport of angular momentum due to electron viscosity (Itoh, Kohyama & Takeuchi 1987).

2.2 WD formation history

Fig. 2 shows the evolution of the donor star in the Kiel diagram leading to a remnant mass of 0.338 $M_{\odot}$ with an He core (solid orange line) and hybrid core (blue dashed line). The evolution is computed from the zero-age main sequence (ZAMS) until the remnant WD cools down to an effective temperature of 5 000 K. In both cases, the companion star is treated as a point mass. We also mark on the evolutionary sequences several important points. The moment when the donor star overflow its Roche lobe (RLOF), marking the beginning of the mass-transfer phase, is depicted with a circle symbol, the end of the mass-transfer phase is marked with a star, the beginning and the end of the core-He burning phase are showed with the square and thin diamond symbol, respectively. Finally, the beginning of the cooling track is represented by the diamond symbol.

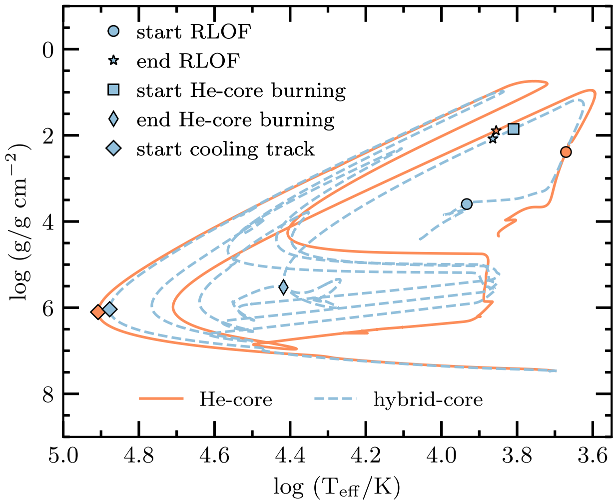

Figure 2. The Kiel diagram showing the formation and the cooling evolution of a 0.338 $M_{\odot}$ He- (solid orange line) and hybrid-core (dashed blue line) WD. The initial binary parameters are $M_{\rm donor} = 1.3\,M_{\odot}$, $M_{\rm accretor} = 1.2\,M_{\odot}$, $P_{\rm initial} = \sim 16.982$ d for the He-core model, and $M_{\rm donor} = 2.3\,M_{\odot}$, $M_{\rm accretor} = 2.0\,M_{\odot}$, $P_{\rm initial} = \sim 1.990$ d for the hybrid-core model, at an initial metallicity of $Z = 0.01$. In both cases, the accretor is treated as a point mass. The evolutionary tracks are computed from ZAMS until the effective temperature of the WD reaches 5 000 K. The symbols mark various stages of evolution. The beginning and the end of the mass-transfer phase are represented by the circle and star symbol, respectively, the beginning and the end of the core-He burning phase (in the case of the hybrid-core sequence) are depicted by the square and thin diamond symbol, respectively, and finally the diamond symbol represents the beginning of the cooling track, i.e. the point when the evolutionary track reaches its maximum effective temperature.

The He-core WDs are formed by stripping mass when the donor star is on its red giant branch. The binary system consists of a low-mass donor star with an initial mass of 1.3 $M_{\odot}$, a main-sequence companion of 1.2 $M_{\odot}$, and an initial orbital period of ∼11.75 and ∼16.98 d, for the progenitor of the 0.325 $M_{\odot}$ and 0.338 $M_{\odot}$, respectively. After the end of the mass-transfer phase, the remnant evolves through the so-called proto-WD phase, in which unstable H burning leads to the occurrence of at least one H flash.

The initial binary configuration leading to the formation of the hybrid-core WDs is a 2.3 $M_{\odot}$ intermediate-mass donor star with a companion of 2.0 $M_{\odot}$, and an orbital period of 1.43 and ∼1.99 d, or the progenitor of the 0.325 $M_{\odot}$ and 0.338 $M_{\odot}$, respectively. The mass-transfer phase initiates during the Hertzsprung gap. Unlike the case of the He-core WD sequence, here the mass transfer ceases due to the core-He ignition. Shortly after the mass transfer ended, the remnant starts the core-He burning phase, which lasts around 670 Myr. Once the CO core is formed, the proto-WD undergoes four H shell flashes before finally settling on the cooling track.

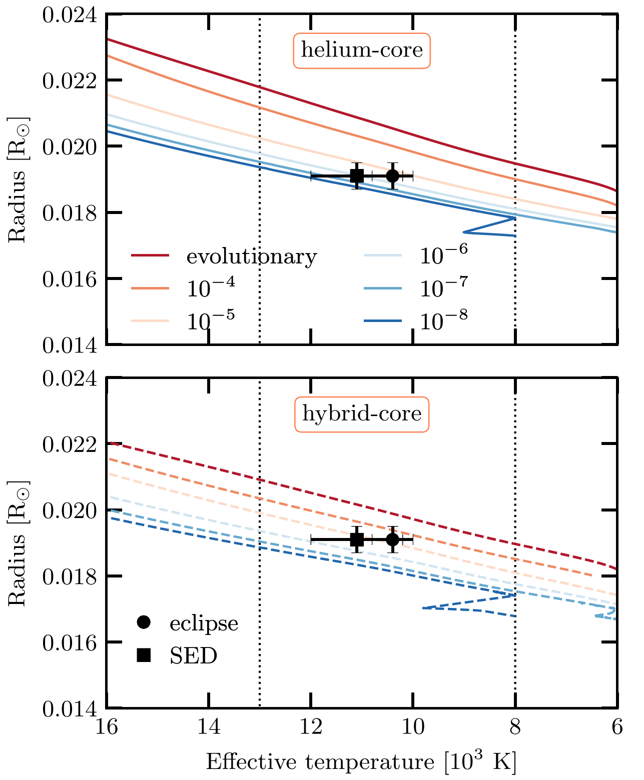

Figure 3. Stellar radius as a function of the effective temperature for both hybrid- (dashed lines) and He-core (solid lines) WD sequences with stellar mass 0.338 M$_\odot$. The symbols correspond to the determinations of the effective temperature from observations (see Table 1). The dotted vertical lines indicate the blue and red edges of the observed instability strip for low-mass WDs (see Fig. 1).

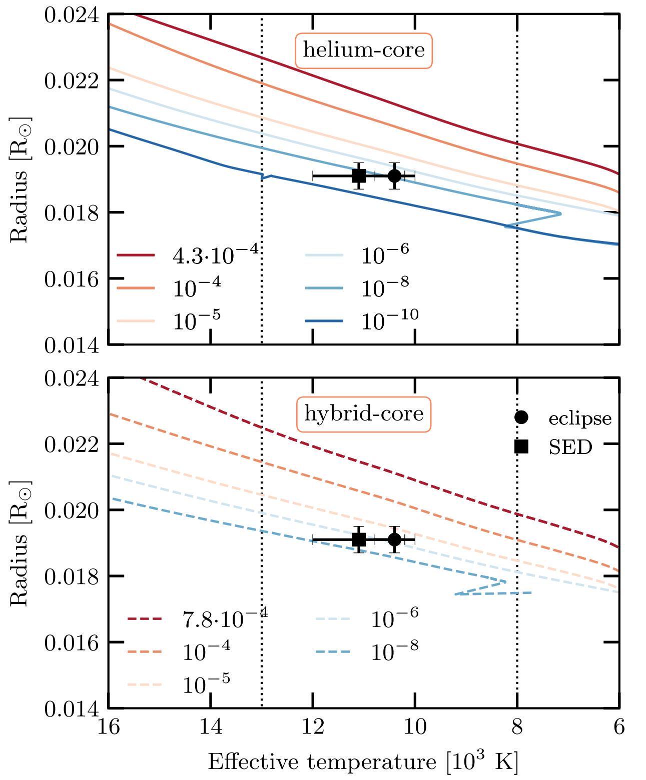

Figure 4. Same as Fig. 3 but for the WD sequences with stellar mass 0.325 M$_\odot$.

2.3 WD cooling track

The WD sequences discussed in the previous section are formed through a stable mass-transfer channel. While it is possible that the first mass-transfer phase which leads to the formation of J1152+0248 −V is stable, we cannot rule out completely a common-envelope evolution. Additionally, the short orbital period of J1152+0248 (2.4 h) suggests that the second mass-transfer phase leading to the formation of the most massive component is unstable and proceeds through a common-envelope evolution. This evolutionary phase could possibly also affect the lower-mass component. Either way, there is an uncertainty in the mass of the H envelope available at the beginning of the cooling track resulting from the evolutionary history prior to the observed stage of the system.

The mass of the H envelope is one of the main factors that influence the cooling evolution of a WD. In order to take this uncertainty into account, we also computed WD cooling sequences with H envelopes thinner than the ones obtained from the binary evolutionary models described above. These sequences were computed using *relaxation* methods available in MESA. The initial conditions are taken at the point when the remnant reaches the beginning of the cooling track. Using the stellar profile at this point, we remove the desired amount of H, keeping the total mass unchanged (see Istrate et al., in preparation, for details).

Figs 3 and 4 show the WD radius as a function of the effective temperature for sequences with He- (top panels) and hybrid-core (bottom panels) and stellar mass of 0.338 M$_\odot$ and 0.325 M$_\odot$, respectively.

For each core composition we consider different values of the H-envelope mass, starting from the value resulting from the binary evolution down to 10^{-8} M$_\odot$. In particular, for the stellar mass of 0.325 M$_\odot$ and He core, we also include a sequence with H-envelope mass of 10^{-10} M$_\odot$. Overplotted are the measured values of J1152+0248 −V, both from the eclipse and the SED fitting.

As expected, the radius for the hybrid-core sequences is smaller than for the He-core sequences, for the same H-envelope mass. Intriguingly, the observations are not compatible with a thick H envelope, i.e. which obtained from binary evolution computations. For sequences characterized with a stellar mass of 0.338 M$_\odot$ (see Fig. 3) the H-envelope mass consistent with the radius and effective temperature from Parsons et al. (2020) is between 10^{-4} and 10^{-6} M$_\odot$ if we consider a hybrid core. For the sequences with an He core, the H-envelope mass is below 10^{-5} M$_\odot$. For sequences with stellar mass of 0.325 M$_\odot$ (see Fig. 4), the H-envelope mass needs to be even smaller to fit the observations, between 10^{-5} and 10^{-8} M$_\odot$ for sequences with a hybrid core and between 10^{-5} and 10^{-10} M$_\odot$ for sequences with an He core. Thus, J1152+0248 −V has an H envelope thinner than that obtained from evolutionary sequences, independently of the central chemical composition.

3 ADIABATIC PULSATIONS

The pulsational properties in stars are dominated by the characteristic frequencies, i.e. the Brunt-Väisälä (N^2) and the Lamb (L_ℓ^2) frequencies (Cowling 1941; Unno et al. 1989). The Brunt-Väisälä frequency represents the oscillation frequency of a convective bubble around the stable equilibrium position. It is closely related with gravity modes since the restoring force is gravity. In the case of low-mass WDs, the gravity modes correspond to the long-period (low-frequency) modes, with periods $\gtrsim$200 s for $\ell = 1$. The N^2 frequency is given by (Brassard et al. 1991)

$$N^2 = \frac{g^2\rho}{P}\frac{\chi_T}{\chi_\rho}\left(\nabla_{\rm ad} - \nabla + B\right), \tag{1}$$

where g, ρ, and P are the gravitational acceleration, the density, and the pressure, respectively. $\nabla_{\rm ad}$ and ∇ are the adiabatic and the temperature gradient, respectively, and χ_T and χ_ρ are defined as,

$$\chi_T = \left(\frac{\partial \ln P}{\partial \ln T}\right)_\rho \tag{2}$$

$$\chi_\rho = \left(\frac{\partial \ln P}{\partial \ln \rho}\right)_T. \tag{3}$$

The term B is called the Ledoux term and it is defined as

$$B = -\frac{1}{\chi_T}\left(\frac{\partial \ln P}{\partial ln X_i}\right)_{\rho,T}\frac{{\rm d}\ln X_i}{{\rm d}\ln P}, \tag{4}$$

where X_i is the chemical abundance of the element i. The Ledoux term B gives the explicit contribution of the change of chemical composition, thus it contributes in the region where chemical transitions are found (Brassard et al. 1992a).

The Lamb frequency is given by

$$L_\ell^2 = \frac{(\ell+1)\ell}{r^2}c_{\rm S}^2, \tag{5}$$

where $c_{\rm S}$ is the adiabatic sound speed. The Lamb frequency is inversely proportional to the time that a sound wave takes to travel a distance $2\pi r/\ell$. It is closely related to pressure modes since the restoring force is the pressure gradient. Pressure modes correspond to short-period (high-frequency) modes with periods of $\lesssim$10 s for low-mass WDs.

For a chemically homogeneous and radiative star, the period spectrum is characterized by a constant period separation, known as the asymptotic period spacing (Tassoul, Fontaine & Winget 1990),

$$\Delta\Pi_a = \frac{\Pi_0}{[\ell(\ell+1)]^{1/2}}, \tag{6}$$

where

$$\Pi_0 = 2\pi^2\left(\int_{r_1}^{r_2}\frac{N(r)}{r}{\rm d}r\right)^{-1}. \tag{7}$$

In the case of WDs, the inner chemical structure is far from homogeneous, showing composition gradients (Althaus et al. 2010b). In this case, the asymptotic period spacing corresponds to the period spacing at the limit of very large values of k (Tassoul et al. 1990).

3.1 Numerical computations

For our pulsational computations we employed GYRE (Townsend & Teitler 2013; Townsend, Goldstein & Zweibel 2018), an open-source stellar oscillation code in its adiabatic form, version 5.0. Although GYRE is integrated within MESA, it was used as a stand-alone package. We performed a scan using a linear grid over a period range of 80−2000 s with `alpha_osc` = 100 and `alpha_exp` and `alpha_ctr` set to 50. The boundary conditions and variables were set to UNNO and DZIEM, respectively.[1]

[1]The inlist and all its configuration settings can be found in here (link to be updated).

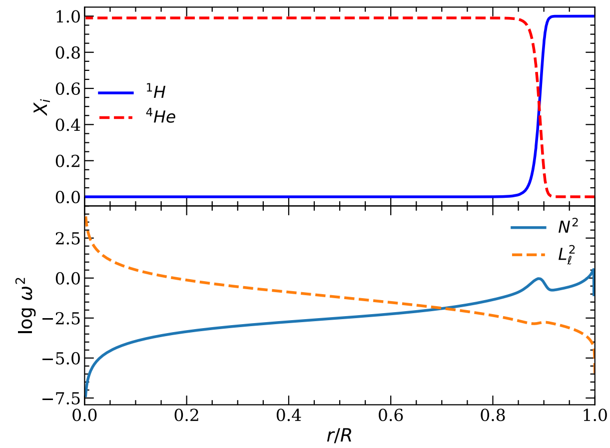

Figure 5. Internal profiles and characteristic frequencies for an *He-core* cooling sequence with M=0.338 M$_\odot$, T$_{\rm eff}$ = 10 000 K, and $M_{\rm H} = 10^{-4}$ M$_\odot$. Top panel: The mass fraction of H and He as a function of the relative radius. Bottom panel: The logarithm of the Brunt-Väisälä (full blue line) and the Lamb (dashed orange line) characteristic frequencies as a function of the relative radius.

We compute pulsations for He- and hybrid-core models in the effective temperature range of 13 000 and 8 000 K, which covers the empirical instability strip. We compute the period spectrum for ℓ = 1 and ℓ = 2 gravity modes with periods in a range of 80 s $\leq \Pi \leq$ 2 000 s.

3.2 Internal composition and the characteristic frequencies

To compare the pulsation properties of He- and hybrid-core WD models, we chose one template model for each central composition, with stellar mass of 0.338 M$_\odot$, effective temperature of 10 000 K, and H-envelope mass of 10^{-4} M$_\odot$. In the top panel of Figs 5 and 6, we depict the chemical profiles for an He- and a hybrid-core template models, respectively. Both template models show a pure H envelope, since gravitational settling had enough time to separate the elements in the outer layers. For the hybrid-core model we have a second chemical transition (He/C/O transition) around $r/R \sim 0.4$, where the He abundance decreases towards the centre while the C and O abundance increase.

The presence of chemical transitions, where the abundances of nuclear species vary considerably in radius, modifies the conditions of the resonant cavity in which modes should propagate as standing waves. Specifically, the chemical transitions act as reflecting walls, trapping certain modes in a particular region of the star, where they show larger oscillation amplitudes. Trapped modes are those for which the wavelength of their radial eigenfunction matches the spatial separation between two chemical transitions or between a transition and the stellar centre or surface (Brassard et al. 1992b; Bradley, Winget & Wood 1993; Córsico et al. 2002).

The bottom panels of Figs 5 and 6 show the run of the logarithm of the Brunt-Väisälä and Lamb frequencies as a function of radius for the template models. The overall behaviour of log N^2 is a general decrease with increasing stellar depth, eventually reaching small values in the deep core, as a consequence of degeneracy. As expected, the bumps in log N^2 correspond to the chemical transition, where the chemical gradients have non-negligible values (Tassoul et al. 1990). For the He-core template model, the Brunt-Väisälä frequency shows only one bump corresponding to the H/He transition at $r/R \sim 0.9$. For the hybrid-core template model, in addition to the bump

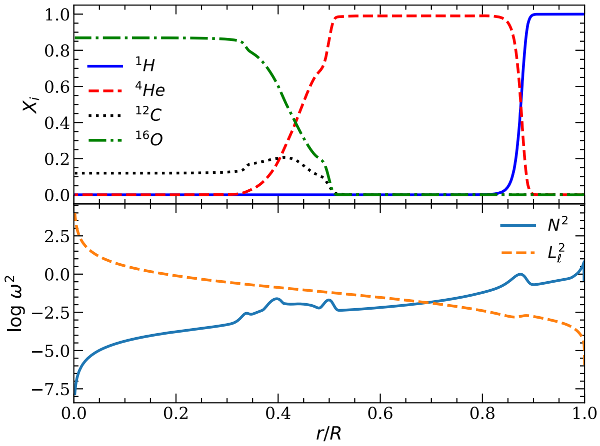

Figure 6. Internal chemical composition and characteristic frequencies for a *hybrid-core* sequence with M=0.338 $M_\odot$, $T_{\rm eff}$ = 10 000 K, and $M_H = 10^{-4}$ $M_\odot$. Top panel: Mass fraction of H, He, C, and O as a function of the relative radius. *Bottom* panel: The logarithm of the Brunt-Väisälä (full blue line) and Lamb (dashed orange line) characteristic frequencies as a function of the relative radius.

at the base of the H envelope, the Brunt-Väisälä frequency shows a structure corresponding to the He/C/O transition around $r/R \sim 0.4$. This transition is wide and shows three peaks due to the structure of the chemical gradients. We expect that the different profiles for the Brunt-Väisälä frequency for He-core and hybrid-core models will impact the pulsation properties, for example the period spectrum and the period spacing.

The Lamb frequency is only sensitive to the H/He transition at the bottom of the H envelope, as it is the case for ZZ Ceti stars (Romero et al. 2012). Thus, we do not believe the pressure modes could give information on the inner regions, if ever detected in low-mass WD stars.

4 RESULTS

4.1 Pulsational properties

As previously mentioned, for a chemically homogeneous and radiative star, the forward period spacing ($\Delta\Pi_k = \Pi_{k+1} - \Pi_k$) would be constant and given by the asymptotic period spacing, defined in equation (6). However, in the stratified inner structures, as the ones found in low-mass WDs, the forward period spacing deviates from a constant value, particularly for low-radial order modes. In this section, we will focus on models with stellar mass 0.338 $M_\odot$. Similar results are found for models with stellar mass of 0.325 $M_\odot$.

Fig. 7 shows the forward period spacing as a function of the period for $\ell = 1$ modes. Top panels correspond to models with He core while bottom panels show the results for hybrid-core models. Finally, each column corresponds to sequences with different values for the H-envelope mass and each curve shows the forward period spacing at a different effective temperature along the cooling curve, from 12 000 K to 9000 K.

For the He-core models the distribution for the forward period spacing as a function of the period, shows a simple trapping cycle characteristic of one-transition models (Brassard et al. 1992b; Córsico & Althaus 2014), with defined local minima, as shown in the top panels of Fig. 7. For the hybrid-core models (bottom panels in Fig. 7) the pattern in the forward period spacing is more complex largely due to the influence of the He/C/O transition in the Brunt-Vaisälä frequency. Even though we expect the H/He transition to be dominant in the mode selection process, the presence of the second, broader, transition is not negligible. The differences in the pattern of the forward period spacing can be used to determine the inner composition of low-mass WDs, if enough consecutive periods are detected.

The trapping period, i.e. the period difference between two consecutive minima in $\Delta\Pi_k$, is longer for lower effective temperatures and thinner H envelopes. This effect is much more evident for the He-core models than for the hybrid-core models.

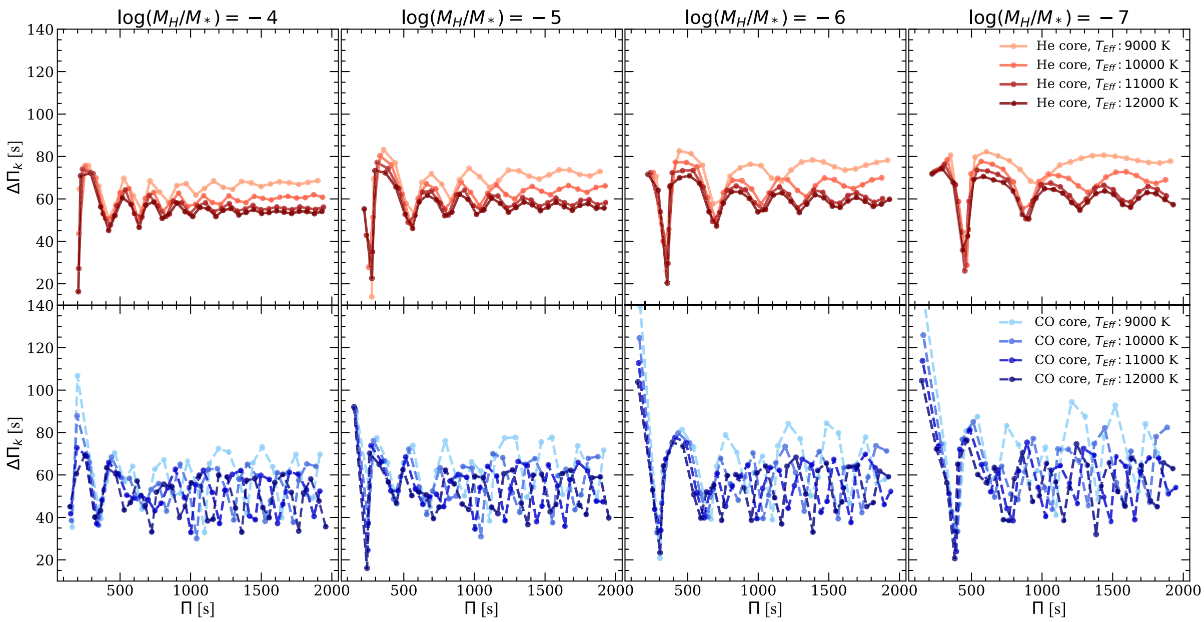

Figure 7. The forward period spacing ($\Delta\Pi_k = \Pi_{k+1} - \Pi_k$) as a function of the period for modes with $\ell = 1$ for He- (top panels) and hybrid-core (bottom panels) models, with stellar mass 0.338 $M_\odot$. Each column corresponds to a different H-envelope mass. In each plot, we show the period spacing for four effective temperatures along the cooling sequence, 12 000, 11 000, 10 000, and 9000 K.

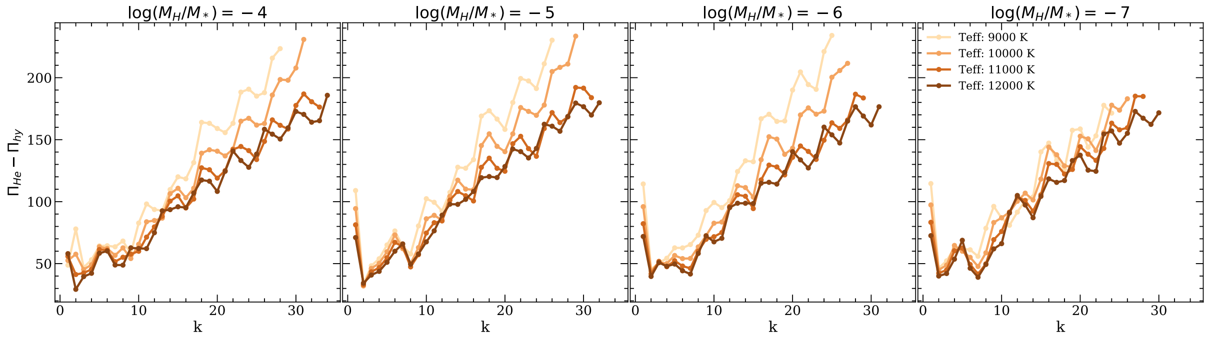

Figure 8. Period difference ($\Pi_{\rm he} - \Pi_{\rm hy}$) as a function of the radial order for $\ell = 1$ modes. The stellar mass is fixed to 0.338 $M_\odot$. Each plot corresponds to a different H-envelope mass. We consider four effective temperatures.

In general, we expect the forward period spacing to increase with decreasing effective temperature and thinner envelopes (Brassard et al. 1992b). This can be better explained in terms of the asymptotic period spacing, given by equation (6). The higher values for $\Delta\Pi_a$, and $\overline{\Delta\Pi}$, for lower effective temperatures result from the dependence of the Brunt-Väisälä frequency as $N \propto \sqrt{\chi_T}$, with $\chi_T \rightarrow 0$ for increasing degeneracy ($T \rightarrow 0$) (see for instance Romero et al. 2012). In addition, the asymptotic period spacing, and the mean period spacing, are longer for thinner H envelopes (Tassoul et al. 1990).

If the stellar mass is fixed, the asymptotic period spacing for the He-core model is longer than that for the hybrid-core model, for the same effective temperature and H-envelope mass. This is related to the dependence of the Brunt-Väisälä frequency on the surface gravity $N \propto g$, where $g \propto M/R^2$. In this case, the radius is smaller for the hybrid-core models which leads to a larger value of the surface gravity (see Figs 3 and 4).

Finally, given the different chemical structure of He- and hybrid-core WD models, we expect different values for the period spectra as well. Fig. 8 shows the period difference between He- and the hybrid-core models, $\Pi_{\rm he} - \Pi_{\rm hy}$ as a function of the radial order k, for harmonic degree $\ell = 1$. Each column corresponds to a different H-envelope mass, while the curves in each panel correspond to four different effective temperatures along the 0.338 $M_\odot$ WD cooling track. In all cases, the difference in the periods between the He- and hybrid-core models are between ∼50 s, for $k \lesssim 10$ and short periods, and ∼200 s for $k \gtrsim 30$ and longer periods. Note that the period difference is always positive, meaning that, for a given radial order, the period for the He-core model is larger than the one corresponding to the hybrid-core model. This is expected, since the periods, and the period spacing, vary as the inverse of the Brunt-Väisälä frequency, and thus the surface gravity (equation 7). As the period also increases with the cooling age, the period difference is larger for lower effective temperatures, particularly for modes with radial order $k > 20$. For future reference, we list the periods for $\ell = 1$ and $\ell = 2$, corresponding to the models considered in Fig. 8 and in Tables A1–A4.

4.2 Asteroseismology of J1152+0248 −V

For J1152+0248 −V Parsons et al. (2020) detected three pulsation periods, with the period of ∼1314 s being the one showing the highest amplitude. The list of observed periods and their corresponding amplitudes are listed in Table 2.

In order to find the theoretical model that better matches the observed periods, we use a standard χ^2 approach where we search for a minima of the quality function, defined as

Table 2. Observed pulsation periods and the corresponding amplitudes for J1152+0248 −V (Parsons et al. 2020).

Period (s)	Amplitude (ppt)
1314 ± 5.9	33.0 ± 1.3
1069 ± 13	9.8 ± 1.3
582.9 ± 4.3	8.9 ± 1.3

$$\chi^2 = \sum_{i=1}^{3} \left(\frac{\Pi_{\rm obs}^{(i)} - \Pi_{\rm th}^{(i)}}{\sigma_{\rm obs}^{(i)}} \right)^2, \qquad (8)$$

where $\Pi_{\rm obs}^{(i)}$ and $\sigma_{\rm obs}^{(i)}$ are the observed periods and their associated uncertainties in g_s-band, and $\Pi_{\rm th}^{(i)}$ are the theoretical periods. In our fit, we consider the mode with the highest detected amplitude, as an $\ell = 1$ mode, since the amplitude is expected to decrease with increasing harmonic degree due to geometric cancellation (Robinson, Kepler & Nather 1982). For the remaining two observed periods, we allowed them to be fitted by $\ell = 1$ and $\ell = 2$ modes. Finally, we restrict the possible seismological solutions to those models that fit the observed periods within the uncertainties reported by Parsons et al. (2020; see Table 2). The results of our seismological fit are depicted in Fig. 9. The value of χ^2 (colour scale) is shown as a function of the effective temperature and the mass of the H envelope. Top (bottom) panels correspond to models with stellar mass 0.338 $M_\odot$ (0.325 $M_\odot$). Models with He core are depicted on the left-hand panels, while the ones with hybrid core are shown in the right-hand panels. The dashed-line rectangle indicates the region where the models are compatible with the radius and effective temperature determinations from Parsons et al. (2020). As can be seen from this figure, there are several families of solutions. For a stellar mass 0.325 $M_\odot$, the best-fitting models are mainly characterized by thick H envelopes, $\sim 10^{-4}$ $M_\odot$ and low effective temperatures, > 9 000 K, for both core compositions. Thin H-envelope solutions, with H mass below $\sim 10^{-5}$ $M_\odot$, are found for models with stellar mass 0.338 $M_\odot$ and hybrid core, for all the effective temperature range.

If we combine our seismological results with the restrictions from the radius and the effective temperature presented in Parsons et al. (2020) (dashed-line rectangle in Fig. 9), the number of possible seismological solutions is largely reduced. In particular, the models characterized by a hybrid-core structure are the ones satisfying both criteria.

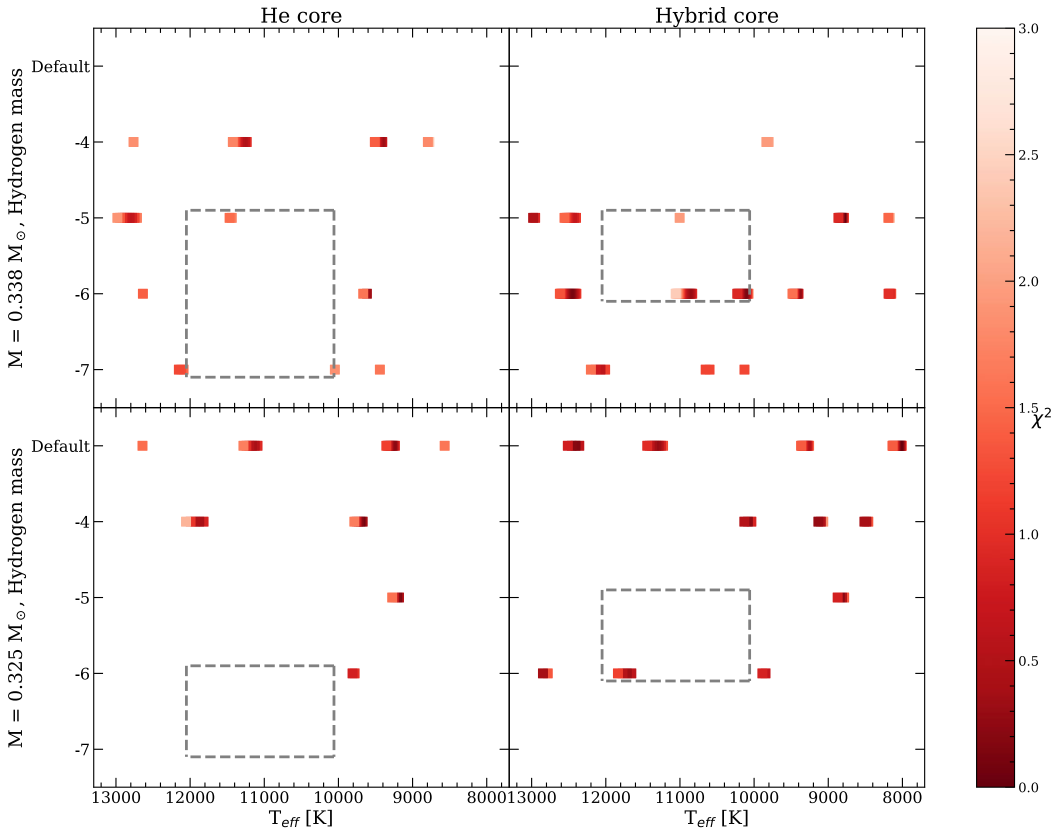

Figure 9. The value of χ^2 (colour scale) as a function of the effective temperature and the mass of the H envelope. Top panels correspond to models with stellar mass 0.338 M$_\odot$, while bottom panels show the results for 0.325 M$_\odot$ models. Both He- (left-hand panels) and hybrid-core (right-hand panels) structures are considered. The dashed-line rectangle indicates the region of the $T_{\rm eff}$–H envelope plane restricted by the determinations of radius and effective temperature from Parsons et al. (2020).

Table 3. Asteroseismological models for the low-mass WD J1152+0248 −V. The effective temperature, H-envelope mass, and central composition are listed in columns 2, 3, and 4, respectively. We list the theoretical periods that better fit the observed periods in column 4, along with the values of ℓ and k, in columns 6 and 7. The value of the quality function χ^2 is listed in column 8.

#	$T_{\rm eff}$ (K)	R/R$_\odot$	M_*/M$_\odot$	$M_{\rm H}$/M$_\odot$	$X_{\rm C}$	$\Pi_{\rm th}$ (s)	ℓ	k	χ^2 (s)
1	10 917	0.0187	0.338	10^{-6}	C/O	1315.4	1	21	0.296
						1063.3	2	30	–
						582.01	2	15	–
2	10 904	0.0187	0.338	10^{-6}	C/O	1316.1	1	21	0.305
						1063.8	2	30	–
						582.3	2	15	–
3	10 929	0.0187	0.338	10^{-6}	C/O	1314.9	1	21	0.318
						1062.8	2	30	–
						581.8	2	15	–
4	11 717	0.0195	0.325	10^{-6}	C/O	1316.1	1	21	0.345
						1066.4	2	30	–
						581.3	2	15	–

The best-fitting models for J1152+0248 −V are listed in Table 3. These models fit the observed periods within the uncertainties and are in agreement with the determinations of radius and effective temperature presented by Parsons et al. (2020). Note that all the models are characterized by an H-envelope mass of 10^{-6} M$_\odot$ and a hybrid core. Thus, we can conclude that J1152+0248 −V is a low-mass WD star with a hybrid core and a thin H envelope.

5 CONCLUSIONS

In this work, we explore the inner chemical structure of the pulsating low-mass WD in the J1152+0248 system using asteroseismology as a tool. This is the first pulsating low-mass WD in an eclipsing binary system with another low-mass WD which allows constraining the mass and radius of each component independently of evolutionary models.

We use low-mass WDs models with a stellar mass of 0.325 and 0.338 $M_\odot$ and an He core and hybrid core, respectively, resulting from fully binary evolutionary computations. In addition, to account for the uncertainty in the H-envelope mass due to the evolution through a common-envelope channel, we use WD sequences with the same stellar mass but with an H envelope thinner than the canonical value obtained from stable mass transfer, i.e. from 10^{-4} to 10^{-10} $M_\odot$. For all these sequences, we calculate adiabatic pulsations for effective temperatures in the range 13 000 K $\leq T_{\rm eff} \leq$ 8000 K.

We perform a study on the pulsating low-mass WD in the binary system J1152+0248 to uncover its inner chemical composition. By comparing the determinations of the radius and effective temperature presented by Parsons et al. (2020) with theoretical models (Istrate et al., in preparation), we find that the variable component of J1152+0248 must have an H envelope thinner than that predicted from stable mass-transfer binary evolution computations.

From the asteroseismological study we find a best-fitting model characterized by $M_* = 0.338$ $M_\odot$, $T_{\rm eff} = 10\,917$ K, $M_{\rm H}/M_\odot = 10^{-6}$, and a hybrid-core composition. In particular, all local minima of χ^2 correspond to models with hybrid core and a thin H envelope.

A systematic study of the pulsational properties and the observed period spectrum of low-mas WDs can give valuable information on the inner structure of these objects. This will help in disentangling the two WD populations coexisting in the mass interval ~0.32–0.45 $M_\odot$ which in turn leads to clues of the underlying progenitor population.

ACKNOWLEDGEMENTS

ADR and GRL acknowledge the support of the Coordenação de Aperfeiçoamento de Pessoal de Nível Superior – Brazil (CAPES) – Finance Code 001, and by Conselho Nacional de Desenvolvimento Científico e Tecnológico - Brazil (CNPq). AGI acknowledges support from the Netherlands Organisation for Scientific Research (NWO). SGP acknowledges the support of a Science and Technology Facilities Council (STFC) Ernest Rutherford Fellowship. Special thanks to Pablo Marchant, Josiah Schwab, and Jocelyn Goldstein for their help with numerical debugging and to the developers of MESA and GYRE for their continuous efforts to improve and extend these codes. This research has made use of NASA's Astrophysics Data System and open source software such as the Python 3 language (Python Core Team 2015), the IPYTHON KERNEL (Pérez & Granger 2007), the Jupyter Project (Kluyver et al. 2016), and the packages MATPLOTLIB (Hunter 2007), PANDAS (McKinney 2010), and the SCIPY ecosystem (Virtanen et al. 2019).

DATA AVAILABILITY

As an effort to promote open science, the results and codes to reproduce our results are available at https://zenodo.org/communities/mesa/.

REFERENCES

Althaus L. G., Córsico A. H., Isern J., García-Berro E., 2010a, A&AR, 18, 471
Althaus L. G., Córsico A. H., Bischoff-Kim A., Romero A. D., Renedo I., García-Berro E., Miller Bertolami M. M., 2010b, ApJ, 717, 897
Althaus L. G., Miller Bertolami M. M., Córsico A. H., 2013, A&A, 557, A19
Bell K. J., Kepler S. O., Montgomery M. H., Hermes J. J., Harrold S. T., Winget D. E., 2015, in Dufour P., Bergeron P., Fontaine G., eds, ASP Conf. Ser. Vol. 493, SDSS J1618+3854: The Sixth Extremely Low-Mass White Dwarf Pulsator. Astron. Soc. Pac., San Francisco, p. 217
Bell K. J. et al., 2017, ApJ, 835, 180
Bognar Z., Sodor A., 2016, Inf. Bull. Var. Stars, 6184, 1
Bradley P. A., Winget D. E., Wood M. A., 1993, ApJ, 406, 661
Brassard P., Fontaine G., Wesemael F., Kawaler S. D., Tassoul M., 1991, ApJ, 367, 601
Brassard P., Fontaine G., Wesemael F., Hansen C. J., 1992a, ApJS, 80, 369
Brassard P., Fontaine G., Wesemael F., Tassoul M., 1992b, ApJS, 81, 747
Brickhill A. J., 1991, MNRAS, 251, 673
Cassisi S., Potekhin A. Y., Pietrinferni A., Catelan M., Salaris M., 2007, ApJ, 661, 1094
Chaboyer B., Zahn J. P., 1992, A&A, 253, 173
Córsico A. H., Althaus L. G., 2014, A&A, 569, A106
Córsico A. H., Althaus L. G., Benvenuto O. G., Serenelli A. M., 2002, A&A, 387, 531
Córsico A. H., Althaus L. G., Miller Bertolami M. M., Kepler S. O., 2019, A&AR, 27, 7
Cowling T. G., 1941, MNRAS, 101, 367
Dolez N., Vauclair G., 1981, A&A, 102, 375
Ferguson J. W., Alexander D. R., Allard F., Barman T., Bodnarik J. G., Hauschildt P. H., Heffner-Wong A., Tamanai A., 2005, ApJ, 623, 585
Fontaine G., Brassard P., 2008, PASP, 120, 1043
Fuchs J. T., 2017, PhD thesis, Univ. North Carolina at Chapel Hill
Garcia-Berro E., Isern J., Hernanz M., 1997, MNRAS, 289, 973
Goldreich P., Wu Y., 1999, ApJ, 511, 904
Grevesse N., Sauval A. J., 1998, Space Sci. Rev., 85, 161
Hallakoun N. et al., 2016, MNRAS, 458, 845
Han Z., Tout C. A., Eggleton P. P., 2000, MNRAS, 319, 215
Heger A., Langer N., Woosley S. E., 2000, ApJ, 528, 368
Henyey L., Vardya M. S., Bodenheimer P., 1965, ApJ, 142, 841
Hermes J. J. et al., 2013a, MNRAS, 436, 3573
Hermes J. J. et al., 2013b, ApJ, 765, 102
Hunter J. D., 2007, Comput. Sci. Eng., 9, 90
Iben I. J., Tutukov A. V., 1985, ApJS, 58, 661
Iglesias C. A., Rogers F. J., 1993, ApJ, 412, 752
Iglesias C. A., Rogers F. J., 1996, ApJ, 464, 943
Istrate A. G., Tauris T. M., Langer N., 2014, A&A, 571, A45
Istrate A. G., Marchant P., Tauris T. M., Langer N., Stancliffe R. J., Grassitelli L., 2016, A&A, 595, A35
Itoh N., Kohyama Y., Takeuchi H., 1987, ApJ, 317, 733
Kawaler S. D., 1988, ApJ, 333, 236
Kepler S. O., Kleinman S. J., Nitta A., Koester D., Castanheira B. G., Giovannini O., Costa A. F. M., Althaus L., 2007, MNRAS, 375, 1315
Kepler S. O. et al., 2015, MNRAS, 446, 4078
Kilic M., Stanek K. Z., Pinsonneault M. H., 2007, ApJ, 671, 761
Kilic M., Hermes J. J., Gianninas A., Brown W. R., 2015, MNRAS, 446, L26
Kluyver T. et al., 2016, in Loizides F., Schmidt B., eds, Positioning and Power in Academic Publishing: Players, Agents and Agendas. p. 87
Kupfer T. et al., 2019, ApJ, 878, L35
Langer N., Fricke K. J., Sugimoto D., 1983, A&A, 126, 207
Lauffer G. R., Romero A. D., Kepler S. O., 2018, MNRAS, 480, 1547
McKinney W., 2010, in van der Walt S., Millman J., eds, Proc. 9th Python Sci. Conf., Vol. 445, Data Structures for Statistical Computing in Python. p. 56
Panei J. A., Althaus L. G., Chen X., Han Z., 2007, MNRAS, 382, 779
Parsons S. G. et al., 2020, Nature Astron., 4, 690
Paxton B., Bildsten L., Dotter A., Herwig F., Lesaffre P., Timmes F., 2011, ApJS, 192, 3
Paxton B. et al., 2013, ApJS, 208, 4
Paxton B. et al., 2015, ApJS, 220, 15
Paxton B. et al., 2018, ApJS, 234, 34
Paxton B. et al., 2019, ApJS, 243, 10
Pelisoli I., Vos J., 2019, MNRAS, 488, 2892
Pelisoli I., Kepler S. O., Koester D., Castanheira B. G., Romero A. D., Fraga L., 2018, MNRAS, 478, 867
Pérez F., Granger B. E., 2007, Comput. Sci. Eng., 9, 21

Pietrukowicz P. et al., 2017, Nature Astron., 1, 0166

Prada Moroni P. G., Straniero O., 2009, A&A, 507, 1575

Python Core Team, 2015, Python: A Dynamic, Open Source Programming Language. Python Software Foundation, Available at: https://www.python.org/

Robinson E. L., Kepler S. O., Nather R. E., 1982, ApJ, 259, 219

Rohrmann R. D., Althaus L. G., García-Berro E., Córsico A. H., Miller Bertolami M. M., 2012, A&A, 546, A119

Romero A. D., Córsico A. H., Althaus L. G., Kepler S. O., Castanheira B. G., Miller Bertolami M. M., 2012, MNRAS, 420, 1462

Romero A. D., Campos F., Kepler S. O., 2015, MNRAS, 450, 3708

Romero A. D. et al., 2019, MNRAS, 490, 1803

Rowan D. M., Tucker M. A., Shappee B. J., Hermes J. J., 2019, MNRAS, 486, 4574

Su J., Fu J., Lin G., Chen F., Khokhuntod P., Li C., 2017, ApJ, 847, 34

Tassoul M., Fontaine G., Winget D. E., 1990, ApJS, 72, 335

Thoul A. A., Bahcall J. N., Loeb A., 1994, ApJ, 421, 828

Townsend R. H. D., Teitler S. A., 2013, MNRAS, 435, 3406

Townsend R. H. D., Goldstein J., Zweibel E. G., 2018, MNRAS, 475, 879

Unno W., Osaki Y., Ando H., Saio H., Shibahashi H., 1989, Nonradial Oscillations of Stars, 2nd edn. University of Tokyo Press, Tokyo

Virtanen P. et al., 2019, Nature Methods, 17, 261

Winget D. E., van Horn H. M., Tassoul M., Fontaine G., Hansen C. J., Carroll B. W., 1982, ApJ, 252, L65

Woosley S. E., Heger A., 2015, ApJ, 810, 34

Zenati Y., Toonen S., Perets H. B., 2019, MNRAS, 482, 1135

APPENDIX A: THEORETICAL PERIODS

Table A1. Period values for $\ell = 1$ and $\ell = 2$ modes corresponding to models with $M_* = 0.338$ $M_\odot$, effective temperature of 12 000 K, and H-envelope mass of 10^{-4}, 10^{-5}, and 10^{-6} $M_\odot$.

$M_H/M_\odot$		10^{-4}		10^{-5}		10^{-6}	
ℓ	k	He	C/O	He	C/O	He	C/O
1	1	204.948	146.886	218.643	147.610	220.319	148.418
1	2	221.260	192.002	273.896	239.660	291.871	252.223
1	3	292.114	252.597	296.524	255.774	356.006	305.175
1	4	364.331	322.131	369.816	326.066	376.420	328.547
1	5	420.666	362.298	442.175	391.085	442.595	392.939
1	6	465.821	405.630	507.842	447.835	512.597	468.370
1	7	518.050	469.162	560.626	494.718	583.536	541.930
1	8	578.586	529.785	606.713	557.217	650.957	592.739
1	9	636.102	573.359	665.303	607.547	704.944	632.512
1	10	682.723	620.481	727.082	659.543	752.211	684.640
1	11	739.842	677.741	786.677	710.230	810.293	739.861
1	12	798.462	723.525	838.796	749.740	873.722	778.522
1	13	849.341	756.759	892.586	794.649	937.811	838.306
1	14	902.294	808.744	954.758	856.940	997.247	898.565
1	15	960.397	864.535	1014.63	912.796	1051.18	952.676
1	16	1014.40	919.221	1067.36	959.175	1106.24	991.396
1	17	1066.15	959.235	1122.26	1002.96	1168.11	1052.52
1	18	1122.16	1004.73	1182.63	1062.39	1231.03	1116.87
1	19	1177.61	1061.12	1240.57	1121.12	1289.88	1166.22
1	20	1229.32	1121.06	1294.31	1165.97	1343.50	1203.20
2	1	120.014	100.316	141.344	100.940	142.736	101.493
2	2	142.587	111.277	160.508	139.347	185.489	150.999
2	3	185.975	151.547	187.659	152.494	209.625	176.847
2	4	225.657	191.494	231.584	194.754	232.453	195.717
2	5	254.034	211.840	272.358	229.803	273.019	231.131
2	6	281.506	237.353	307.956	260.380	314.097	273.528
2	7	314.200	273.648	334.955	288.159	354.935	316.423
2	8	349.925	308.696	364.899	326.241	319.257	347.570
2	9	379.496	336.314	400.421	358.342	418.988	372.001
2	10	408.479	365.660	435.919	386.702	449.058	401.706
2	11	443.206	396.338	468.693	416.106	484.623	439.694
2	12	475.033	425.943	497.913	452.092	521.580	476.215
2	13	504.023	461.149	531.857	483.738	557.625	498.294
2	14	536.607	486.195	567.956	503.483	590.826	524.268
2	15	569.643	506.188	600.466	533.089	621.325	560.439
2	16	599.506	538.593	630.662	570.281	655.268	596.169
2	17	630.599	572.313	664.302	597.936	691.754	617.974
2	18	663.345	594.209	699.097	619.426	727.368	649.520
2	19	694.175	617.784	731.092	652.467	759.583	684.916
2	20	724.441	652.464	762.392	689.291	791.026	716.668
2	21	756.787	684.847	795.637	714.925	825.950	738.317
2	22	787.930	709.047	829.417	737.077	861.764	774.935
2	23	818.226	731.327	861.601	772.178	895.634	813.010
2	24	849.940	764.288	893.184	810.806	927.753	848.125
2	25	881.227	800.000	926.496	843.600	960.895	870.022
2	26	911.804	833.115	959.922	863.817	995.764	902.046
2	27	943.122	853.700	991.721	894.125	1030.54	939.114
2	28	974.435	879.080	1023.75	930.100	1063.74	966.625
2	29	1005.23	913.682	1057.21	956.318	1096.41	989.506
2	30	1036.10	941.506	1089.98	978.538	1130.42	1026.26

Table A2. Period values for $\ell = 1$ and $\ell = 2$ modes corresponding to models with $M_* = 0.338$ $M_\odot$, effective temperature of 11 000 K, and H-envelope mass of 10^{-4}, 10^{-5}, and 10^{-6} $M_\odot$.

$M_H/M_\odot$		10^{-4}		10^{-5}		10^{-6}	
ℓ	k	He	C/O	He	C/O	He	C/O
1	1	207.777	151.919	233.957	152.645	235.524	153.322
1	2	234.935	193.714	276.833	243.947	307.762	266.071
1	3	308.929	266.516	311.893	268.497	361.733	309.919
1	4	380.793	335.386	389.048	342.310	391.382	343.863
1	5	433.845	372.487	463.274	408.527	463.749	411.409
1	6	481.618	420.763	528.221	461.074	537.098	489.063
1	7	538.336	486.755	577.219	513.621	610.573	564.377
1	8	602.632	547.503	629.465	582.118	676.213	616.106
1	9	655.766	598.093	692.730	635.549	725.608	655.982
1	10	707.296	647.314	756.426	681.750	779.270	707.562
1	11	769.074	697.705	814.497	731.479	843.416	768.330
1	12	825.765	746.133	866.850	782.429	909.524	813.564
1	13	877.491	789.346	928.721	827.532	973.853	868.318
1	14	936.544	836.128	992.887	884.697	1032.09	927.724
1	15	994.745	890.138	1049.75	944.978	1087.01	992.624
1	16	1047.83	952.948	1104.48	1003.92	1149.66	1032.11
1	17	1104.56	1002.48	1166.22	1038.52	1215.34	1085.88
1	18	1162.76	1035.48	1227.62	1092.55	1277.54	1149.55
1	19	1216.77	1091.03	1283.50	1156.59	1333.40	1211.86
1	20	1272.22	1153.26	1340.63	1216.10	1392.04	1256.28
2	1	120.711	103.726	149.787	104.375	151.814	104.829
2	2	151.834	112.262	162.269	141.279	194.448	158.655
2	3	195.703	159.298	197.606	160.112	211.759	179.466
2	4	234.191	198.316	243.168	203.875	243.337	204.548
2	5	261.843	218.039	284.536	239.630	285.963	241.754
2	6	291.547	246.112	318.537	267.939	328.974	285.360
2	7	327.190	283.652	345.423	299.045	370.474	328.794
2	8	362.990	318.254	379.569	339.961	404.184	360.358
2	9	390.988	350.257	416.755	375.420	431.958	388.493
2	10	424.473	383.250	452.823	402.049	466.541	417.648
2	11	459.804	409.554	483.925	429.733	504.598	454.562
2	12	490.304	438.938	516.320	467.240	542.571	490.865
2	13	521.968	475.075	553.706	498.686	578.574	513.862
2	14	556.885	500.928	589.250	519.210	610.434	540.633
2	15	588.750	521.371	620.508	550.428	644.063	580.230
2	16	620.001	555.159	654.070	590.481	681.677	621.644
2	17	653.702	590.195	690.425	625.170	719.126	649.981
2	18	686.347	622.643	724.303	648.467	753.175	671.000
2	19	717.267	644.476	756.359	674.238	785.390	707.347
2	20	750.538	671.115	790.585	711.447	821.198	745.512
2	21	783.051	704.597	825.706	743.906	858.469	768.119
2	22	814.218	737.499	859.058	764.570	893.692	799.575
2	23	846.959	757.240	891.796	797.047	926.893	838.324
2	24	879.365	785.944	926.331	835.814	961.390	878.146
2	25	911.008	822.649	960.885	872.099	997.639	907.292
2	26	943.351	858.165	993.755	900.244	1033.59	933.155
2	27	975.716	887.886	1027.15	924.922	1067.91	970.154
2	28	1007.49	908.910	1061.95	960.303	1101.84	1008.85
2	29	1072.09	940.675	1095.65	997.176	1137.52	1034.44
2	30	1103.79	975.775	1128.77	1024.26	1173.68	1060.13

Table A3. Period values for $\ell = 1$ and $\ell = 2$ modes corresponding to models with $M_* = 0.338$ $M_\odot$, effective temperature of 10 000 K, and H-envelope mass of 10^{-4}, 10^{-5}, and 10^{-6} $M_\odot$.

$M_H/M_\odot$		10^{-4}		10^{-5}		10^{-6}	
ℓ	k	He	C/O	He	C/O	He	C/O
1	1	209.850	157.321	252.328	157.951	254.801	158.549
1	2	253.518	195.924	280.175	248.189	326.917	283.059
1	3	329.045	283.798	331.577	285.471	366.984	315.927
1	4	398.872	349.747	411.843	361.596	412.719	362.727
1	5	449.743	386.155	487.861	248.295	490.081	433.524
1	6	501.311	439.089	550.052	476.945	567.284	513.238
1	7	564.292	507.595	598.176	536.112	642.441	588.261
1	8	629.238	566.539	658.379	608.287	703.193	639.718
1	9	679.188	625.059	725.480	662.554	752.760	680.114
1	10	739.471	673.875	790.184	704.021	815.755	733.170
1	11	802.594	718.873	845.394	756.443	884.549	800.999
1	12	856.823	772.083	904.980	819.879	953.196	856.930
1	13	914.781	828.101	972.970	868.674	1017.90	905.083
1	14	977.584	871.154	1036.10	918.761	1075.56	964.206
1	15	1034.07	923.283	1092.89	982.771	1138.42	1034.76
1	16	1091.60	988.449	1155.57	1045.98	1208.10	1074.30
1	17	1153.16	1042.38	1222.19	1076.96	1277.21	1124.88
1	18	1211.49	1072.43	1284.28	1129.61	1341.23	1190.77
1	19	1268.95	1127.11	1344.28	1199.66	1402.32	1264.19
1	20	1330.48	1189.77	1408.16	1267.85	1468.56	1325.45
2	1	121.586	107.287	157.518	107.919	163.156	108.312
2	2	163.416	113.564	167.306	143.524	203.910	168.026
2	3	206.981	168.965	209.618	169.896	216.181	183.062
2	4	243.544	205.790	256.828	214.873	257.004	215.468
2	5	271.659	226.439	298.421	250.869	302.091	254.650
2	6	304.270	256.870	329.841	277.285	347.023	299.360
2	7	343.101	295.672	359.639	312.151	388.134	342.354
2	8	376.609	329.099	397.374	355.056	418.378	374.155
2	9	406.703	365.975	436.177	392.490	450.250	406.368
2	10	443.943	400.944	471.367	418.069	489.031	434.251
2	11	478.181	424.514	502.886	445.030	529.062	470.434
2	12	509.339	453.685	540.512	483.040	568.103	506.993
2	13	545.056	489.279	579.302	514.825	603.410	532.999
2	14	580.024	516.482	613.501	538.859	637.183	562.265
2	15	612.022	540.797	647.314	572.300	675.967	604.029
2	16	646.904	574.901	685.322	612.391	716.491	646.414
2	17	981.976	609.741	722.939	649.241	755.304	682.219
2	18	714.771	647.571	757.683	684.100	790.917	702.311
2	19	749.324	679.309	793.296	703.049	827.350	735.388
2	20	784.642	696.728	831.114	737.108	866.985	777.381
2	21	818.136	728.585	868.816	774.163	907.360	807.014
2	22	852.723	764.778	904.819	802.704	946.459	832.156
2	23	888.137	792.796	941.137	828.950	984.102	871.453
2	24	922.537	815.698	979.211	866.280	1021.99	914.490
2	25	957.299	850.262	1017.29	905.561	1061.17	951.177
2	26	992.689	887.230	1053.93	942.024	1101.43	976.345
2	27	1027.87	923.354	1090.87	966.846	1141.57	1011.69
2	28	1062.61	950.145	1129.15	998.759	1180.46	1053.86
2	29	1098.14	975.476	1167.12	1038.43	1219.08	1088.51
2	30	1133.72	1011.07	1204.56	1074.88	1258.10	1110.10

Table A4. Period values for $\ell = 1$ and $\ell = 2$ modes corresponding to models with $M_* = 0.338\ \mathrm{M}_\odot$, effective temperature of **9 000** K, and H-envelope mass of 10^{-4}, 10^{-5}, and $10^{-6}\ \mathrm{M}_\odot$.

$M_\mathrm{H}/\mathrm{M}_\odot$		10^{-4}		10^{-5}		10^{-6}	
ℓ	k	He	C/O	He	C/O	He	C/O
1	1	211.971	163.184	272.688	163.728	278.506	164.253
1	2	276.632	198.670	286.577	253.161	349.212	303.724
1	3	352.387	305.461	355.981	307.717	375.098	324.564
1	4	418.508	365.398	439.196	385.267	440.661	386.324
1	5	469.126	404.819	516.118	451.060	523.307	460.588
1	6	526.313	461.883	573.907	497.554	604.686	542.008
1	7	595.997	532.423	627.193	563.328	680.545	615.165
1	8	657.552	589.357	695.003	637.210	738.264	665.314
1	9	711.747	653.526	766.831	686.424	797.295	704.490
1	10	780.216	697.500	833.735	731.373	868.130	768.783
1	11	843.534	745.433	893.015	793.537	942.846	847.662
1	12	901.897	808.247	961.966	869.583	1019.19	918.324
1	13	968.255	875.514	1036.37	928.897	1094.93	970.636
1	14	1035.46	925.732	1106.85	979.084	1164.70	1031.76
1	15	1097.32	977.308	1172.29	1045.33	1233.01	1100.78
1	16	1162.30	1043.90	1241.03	1107.19	1306.57	1139.70
1	17	1230.74	1099.27	1314.57	1145.56	1383.92	1213.45
1	18	1296.20	1132.24	1387.83	1214.51	1462.30	1297.58
1	19	1360.81	1197.61	1458.53	1291.93	1539.71	1374.64
1	20	1429.04	1270.06	1527.91	1369.63	1614.85	1424.85
2	1	122.673	111.022	161.731	111.709	177.473	112.048
2	2	177.534	115.239	179.106	146.305	211.221	178.889
2	3	219.601	181.074	224.211	182.664	226.761	188.896
2	4	254.109	214.244	273.063	228.523	274.394	229.265
2	5	283.806	237.817	313.728	263.906	322.327	270.651
2	6	320.563	270.466	343.764	289.721	369.126	316.276
2	7	361.292	310.114	378.605	328.255	408.989	358.240
2	8	392.415	342.644	419.762	372.913	440.332	391.682
2	9	428.280	384.076	460.811	410.346	478.305	423.698
2	10	467.738	417.823	496.879	433.479	507.736	451.141
2	11	502.082	439.454	532.901	463.571	564.517	493.970
2	12	537.746	471.766	575.233	507.100	608.865	537.519
2	13	577.290	510.640	617.606	544.610	651.321	570.193
2	14	614.507	543.309	656.751	574.361	690.583	602.753
2	15	650.556	573.042	694.888	610.217	731.419	647.504
2	16	689.501	608.268	736.295	655.098	775.176	697.196
2	17	728.692	646.436	779.002	698.230	820.347	733.340
2	18	765.618	688.715	820.721	730.570	865.547	756.089
2	19	804.125	724.033	861.022	752.829	909.721	799.923
2	20	843.683	741.825	901.474	797.069	952.601	844.521
2	21	882.106	778.876	943.447	839.523	995.140	871.128
2	22	920.408	820.648	986.213	865.190	1038.45	909.888
2	23	959.520	851.564	1028.20	898.880	1082.74	959.228
2	24	998.867	876.304	1069.13	645.024	1127.70	1003.20
2	25	1037.62	916.100	1110.60	988.842	1172.86	1032.01
2	26	1076.42	958.321	1153.10	1019.67	1217.46	1070.84
2	27	1116.01	995.860	1195.53	1052.01	1261.71	1117.93
2	28	1155.22	1022.68	1237.56	1095.90	1305.52	1157.13
2	29	1194.12	1057.21	1279.30	1137.63	1349.21	1187.67
2	30	1233.58	1097.80	1321.30	1166.17	1393.53	1231.34

This paper has been typeset from a TEX/LATEX file prepared by the author.

APPENDIX C – GYRE Configuration File

```
&constants
/

&model
model_type = 'EVOL'  ! Obtain stellar structure from an evolutionary model
file = 'profileYYYY.data.GYRE'
file_format = 'MESA' ! File format of the evolutionary model
/

&mode
l = 1
/

&mode
l = 2
/

&osc
outer_bound = 'UNNO'
inner_bound = 'REGULAR'
variables_set = 'DZIEM'
zeta_scheme = 'KAWALER'
inertia_norm = 'RADIAL'
/

&rot
/

&num
diff_scheme = 'COLLOC_GL4'
/

&scan
grid_type = 'LINEAR'
freq_min = 5.0d-4  ! Minimum frequency to scan from 1/2000
freq_max = 5.0d-3  ! Maximum frequency to scan to ~1/200
n_freq = 2000      ! Number of frequency points in scan
freq_min_units = 'HZ'
```

```
freq_max_units = 'HZ'
/

&grid
alpha_osc = 100  ! Ensure at least 100 points per wavelength in propagation regions
alpha_exp = 50   ! Ensure at least 50 points per scale length in evanescent regions
alpha_ctr = 50     ! Ensure at least 50 points between center and inner turning points
/

&ad_output
summary_file = 'summary.txt'
summary_file_format = 'TXT'
detail_template = 'mode.%J.txt'
detail_file_format = 'TXT'
freq_units = 'HZ'
/

&nad_output
/
```